Doctoral theses at NTNU, 2017:256

Atsede Gualu Endegnanew

Stability Analysis of High Voltage Hybrid AC/DC Power Systems

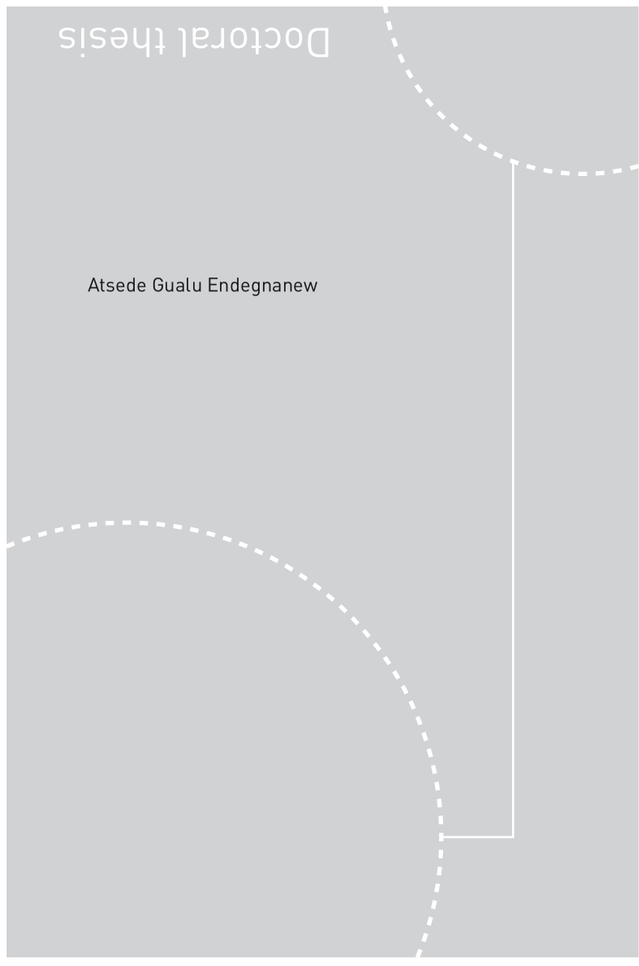

ISBN 978-82-326-2583-3 (printed ver.)
ISBN 978-82-326-2584-0 (electronic ver.)
ISSN 1503-8181

NTNU
Norwegian University of
Science and Technology

NTNU
Norwegian University of Science and Technology
Thesis for the Degree of
Philosophiae Doctor
Faculty of Information Technology and Electrical
Engineering
Department of Electric Power Engineering

Doctoral theses at NTNU, 2017:256

NTNU
Norwegian University of
Science and Technology

Atsede Gualu Endegnanew

Stability Analysis of High Voltage Hybrid AC/DC Power Systems

Thesis for the Degree of Philosophiae Doctor

Trondheim, September 2017

Norwegian University of Science and Technology
Faculty of Information Technology and Electrical Engineering
Department of Electric Power Engineering

NTNU
Norwegian University of
Science and Technology

NTNU
Norwegian University of Science and Technology

Thesis for the Degree of Philosophiae Doctor

Faculty of Information Technology and Electrical Engineering
Department of Electric Power Engineering

ISBN 978-82-326-2583-3 (printed ver.)
ISBN 978-82-326-2584-0 (electronic ver.)
ISSN 1503-8181

IMT-report 2017:256

Doctoral theses at NTNU, 2017:256

Printed by NTNU Grafisk senter

Abstract

Interest in large-scale integration of power from renewable energy sources (RES) has grown in the last decade as a result of energy policies adopted by governments in an effort to reduce CO_2 and greenhouse gas emissions. Both large scale, and distributed solar and wind energy have proliferated the power system and will continue to do so in the future. Thus, large and complex transmission systems are needed for robust, flexible and secure operation of the future power system. Multi-terminal HVDC (MTDC) grids are expected to play an important role in an efficient socio-economic operation of the electric power system by acting as a means for integration of RES, exchange of balancing power, cross-border power market trading, grid reinforcement, etc.

As the introduction of MTDC grids will eventually result in a hybrid ac/dc power system, it is necessary to carry out a global analysis that considers the entire hybrid ac/dc power system, which includes both dc and all synchronous areas of the power systems. The main objective of this PhD is to study the stability of hybrid ac/dc power systems, with a particular focus on the ac grids. The work investigates how the dynamic characteristics of ac grids will be affected by the introduction of the MTDC grids and/or by control methods implemented in MTDC converter controllers.

Modal analysis, in particular eigenvalues, mode shapes, and participation factors, was used to identify and analyze interactions (dynamic coupling) between different subsystems in a hybrid ac/dc power system. Mode shapes were used to identify electromechanical interactions between generators located in different synchronous areas (asynchronous grids). The inter-grid electromechanical interactions are generally weak but are influenced by dc grid control strategy, controller tuning and damped frequency of electromechanical modes. The source of the interactions is dynamic coupling between ac and dc grids. When several terminals share the duty of dc voltage regulation, as in the case of dc voltage droop control operation mode, the dynamics of the ac grids behind those terminals are coupled to a common dc grid dynamics. This leads to indirect coupling of dynamics of different ac grids through dc grid dynamics. A qualitative analysis of state matrix of a single 2-level converter with and without connection to a detailed ac grid model was used to supplement the findings of the quantitative modal analysis. It was shown that

there is a *two-way* dynamic coupling between ac and dc grids when a converter is operated in constant dc voltage or dc voltage droop control modes, i.e. ac grid dynamics is coupled with dc grid dynamics and dc grid dynamics is coupled with ac grid dynamics. However, there is only a *one-way* coupling between an ac grid and a dc grid if the converter is operated in constant power control mode. In such cases, the ac grid dynamics is coupled with the dc grid dynamics, but the dc grid dynamics is not coupled with the ac grid dynamics.

Decentralized control techniques were used to study interactions between power oscillation damping (POD) controllers on multiple terminals of an MTDC that interconnects several asynchronous ac grids. Interaction between the selected control loops was assessed using dynamic relative gain array and performance relative gain array techniques in the frequency domain. In addition, modal and time domain analyses carried out for the study case supported the findings from the frequency domain analysis. For the study case analyzed, it was found that due to control loop interactions the performance of one of the controllers was augmented, while the performance of the other controller deteriorated. The analyses clearly showed that control loop interaction should be considered while tuning PODs on converters even if they are connected to different grids.

Finally, a coordinated control strategy for terminal converters of a dc grid was proposed to address the issue of frequency disturbance in other ac grids when one grid receives frequency support from an offshore wind farm. It was shown that by coordinating converter controllers at the terminals of an offshore wind farm and one ac grid, it is possible to maximize frequency support contribution of the offshore wind farm and avoid disturbance in other ac grids connected to the MTDC. However, the proposed method works when only one ac grid is receiving frequency support and the remaining ac grids are connected MTDC terminals, which are operating in dc droop or constant power control mode. If more than one ac grids are to receive frequency support through MTDC grid, then negative interactions occur when the proposed controller is used. Therefore, in such cases, distributed dc voltage and frequency droop control is the best control option. However, it should be noted that with distributed dc voltage and frequency droop control method, the frequency support comes not only from the wind farm but also from other ac grids behind an MTDC terminal operating in dc voltage droop control mode.

Acknowledgement

This thesis summarizes the research conducted during my PhD study, which was carried out at the Department of Electric Power Engineering at the Norwegian University of Science and Technology. The PhD was partly financed by the "DC grids for integration of large scale wind power-OffshoreDC" project that was funded by Nordic Energy Research and several industry partners.

First and foremost, I would like to thank my supervisor Professor Kjetil Uhlen for giving me the opportunity to work on this topic, for his positive encouragement, unwavering support and open door policy throughout the PhD period. I would also like to thank my co-supervisor Salvatore D'Arco for finding time in his busy schedule to discuss and comment on the progress of the work. In addition, I am grateful to Jef Beerten who has guided and advised me at an earlier stage of the research. The work has greatly benefited from the collaboration works with Jef Beerten, Lester Kalemba and Gilbert Bergna-Diaz. Thank you all.

I would like to extend my gratitude to Ula, Trond, Sverre and Abel who have kindly read the draft of the thesis and provided valuable comments. Many thanks goes to my colleagues at the Electric Power Engineering department and at SINTEF Energy Research for creating an easy, fun and comfortable working environment. Special thanks is due to Abel for being a commendable office-mate, Andrzej and Ula for all their support, for being good friends and neighbors, Trond for being my mentor, friend, colleague and family, Sverre for his patience and understanding, and my Ethiopian friends in Trondheim for all the good times and for always being there for me.

Finally, I would like to express my heartfelt thanks to my parents and siblings for their endless love and invaluable support and the Almighty God for everything I am and have.

Table of Contents

List of Tables

List of Figures

List of symbols

Symbol	Unit	Description
c_{dc}	s	DC link capacitor
E'	$p.u.$	Transient voltage
E''	$p.u.$	Sub-transient voltage
E_{fd}	$p.u.$	Field excitation voltages
H	s	Inertia constant
I_t	$p.u.$	Generator terminal current
i_{cz}	$p.u.$	Circulating current
i_{g_dq}	$p.u.$	Current flowing from converter into grid in dq- reference frame
L_a	$p.u.$	Arm inductor
M_d		State variable associated with the PI in the d-axis outer controller
M_q		State variable associated with the PI in the q-axis outer controller
N_d		State variable associated with the PI in the d-axis inner current controller
N_q		State variable associated with the PI in the q-axis inner current controller
P_m	$p.u.$	Mechanical power
T_{rconv}	s	Switching time delay
v_{dc}	$p.u.$	DC voltage
v_{g_dq}	$p.u.$	PCC voltage in dq reference frame
v_{g_ReIm}	$p.u.$	PCC voltage in global reference frame
v_{s_dq}	$p.u.$	Internal VSC voltage in dq reference frame
V_t	$p.u.$	Generator terminal voltage
$w_{\Sigma,z}$	$p.u.$	Zero-sequence energy-sum
x_{AVR}		State variable associated with AVR
x_{GOV}		State variables associated with turbine/governor
x_{pll}		State variable associated with PI controller of the PLL
x_{PSS}		States associated with PSS
δ	rad	Rotor angle
$\Delta\omega$	$p.u.$	Rotor speed deviation from synchronous speed
κ		State variable associated with PI in zero-sequence energy controller
θ_{pll}	rad	PLL estimated PCC voltage angle
ρ_{dc}		DC voltage droop constant
ω_o	rad/s	Base grid frequency ($2\pi f$)
ω_{pll}	$p.u.$	Grid frequency measured by a PLL
ξ		State variable associated with PI in zero-sequence circulating current controller

Abbreviation

AVR	Automatic Voltage Regulator
DAE	Differential And Algebraic Equations
DRGA	Dynamic Relative Gain Array
EMT	Electro-Magnetic Transients
FACTS	Flexible AC Transmission System
FCR	Frequency Containment Reserve
HVAC	High Voltage Alternating Current
HVDC	High Voltage Direct Current
IGBT	Insulated-Gate Bipolar Transistor
LCC	Line Commutated Converter
MMC	Modular Multi-level Converter
MIMO	Multi-Input-Multi-Output
MTDC	Multi-Terminal HVDC
PRGA	Performance Relative Gain Array
PLL	Phase Locked Loop
PCC	Point of Common Coupling
POD	Power Oscillation Damping
PSS	Power System Stabilizer
RGA	Relative Gain Array
RES	Renewable Energy Sources
SEXS	Simplified Excitation System
SVC	Static Var Compensator
SM	Submodules
TCSC	Thyristor Controlled Series Capacitor
VSC	Voltage Source Converter

1. Introduction

1.1. Background and Motivation

Interest in large-scale integration of power from renewable energy sources (RES) has grown in the last decade as a result of energy policies adopted by governments in an effort to reduce CO_2 and greenhouse gas emissions [1, 2]. The Paris Agreement [3] signed in December 2015 by all member states of the United Nations will shape energy policies around the globe and further strengthen commitment to the development of RES. Hence, wind, solar, wave, and tidal power will take a significant share of the electric power generation in the future alongside the conventional hydro and thermal based power generations. The offshore wind farm developments in the North Sea region are also part of this larger picture. The total installed offshore wind power in Europe, mostly located in the North Sea, was 12.6 GW by the end of 2016 [4], and according to European Wind Energy Association (EWEA) central scenario, this number is expected to increase to 23.5 GW by 2020 [5]. Large and complex transmission systems will be needed to transfer power from offshore wind farms to onshore connection points. Moreover, additional transmission systems are also needed for the exchange of balancing power between the different systems located around the North Sea, which will become even more important once the intermittent wind power plants are installed. Due to the long distances and the large amount of power that needs to be transferred, the transmission system will consist of High Voltage Direct Current (HVDC) systems, possibly with multiple connection points.

High Voltage Direct Current (HVDC) transmission links are preferred over high voltage ac transmissions (HVAC) for large amount of power transfer over long distances. This is because of the high cost and limited power transfer capacity HVACs have beyond a certain distance. HVAC transmission is economical up to approximately 600 – 800 km for overhead lines and feasible up to around 100 km for high voltage cables. The limitation in power transfer capacity in cables comes from the high reactive power generated by the cable capacitances along the transmission. Thus, for connection of offshore wind farms located far out in the sea, HVDC transmission using submarine cables is the only viable option. BorWin1 was the first offshore wind farm to be connected to shore using an HVDC link [6]. Since then, several offshore wind farms in the North Sea have used or plan to use HVDC links for main grid connection [7-11].

Multi-terminal HVDC (MTDC) grids are high voltage dc transmission systems with more than two converter terminals. Although almost all of the dc transmissions in the world today are two terminal point-to-point HVDC links, MTDC grids are foreseen as the next step in dc transmission. This is because MTDC grids are expected to play an important role in an efficient socio-economic operation of the electric power system by acting as a means for integration of RES, exchange of balancing power, cross-border power market trading, grid reinforcement, etc. In general, they will contribute to the robust, flexible and secure operation of the power system. For an MTDC grid to emerge as a viable option for large-scale offshore wind power integration and interconnection of ac systems, solutions need to be developed for stable and secure operation of the dc grid. To this end, considerable research has been conducted on modeling [12-15], and control [16-21] of MTDC grids.

Although the introduction of MTDC grids will eventually result in a hybrid ac/dc power system, most of the research has focused on the control and operation of the MTDC grid itself. In many of these research works, not much attention has been paid to the ac grids and are usually modeled as stiff buses. On the other hand, in studies concerning the provision of ancillary services through the MTDC grid, the ac grids are modeled in detail. However, the focus of these investigations has mostly been on determining the capability of MTDC grids to provide ancillary services to a single ac grid. For instance, the technical feasibility of frequency reserve sharing strategies is demonstrated through isolated analysis limited to a single synchronous grid with a focus on the frequency of the grid under study. However, in a global system where several synchronous grids are connected through an HVDC links, frequency reserve sharing will also affect the frequency of other synchronous zones, which may or may not experience a lack of frequency reserve and/or inertia. Therefore, it is important to carry out a global analysis that considers the entire hybrid ac/dc power system, which includes both dc and all asynchronous grids.

This PhD research work aims at addressing this lacuna by focusing on both ac and dc grids in hybrid ac/dc grids, and by investigating how the ac grid will be affected by the introduction of the MTDC grids and/or by control methods implemented in the converter controllers.

1.2. Objectives and Main Contributions

The main objective of this PhD work is to study the stability of high voltage hybrid ac/dc power systems, with a particular focus on the ac grids. It analyzes the dynamic

characteristics of the systems and interaction of control loops. The objective of this work is to:

- study how the dynamics of different ac grids are affected when the grids are interconnected through an MTDC grids, and the control methods implemented for the dc grid;
- investigate interactions between the electro-mechanical modes of synchronous generators across the dc system;
- understand and model the nature of dynamic interactions between ac grids connected through an MTDC system;
- develop a linear model of a generalized system that includes both detailed MTDC grid and multi-machine ac grids in order to get a full picture of the ac-to-dc and ac-to-ac dynamic interaction;
- explore possible adverse interactions between controllers in a hybrid ac/dc grid;
- study global frequency stability in a hybrid ac/dc grid.

The main contributions of this thesis are:

i. *Identification of small-signal interactions between asynchronous grids connected through a multi-terminal dc grid*

Modal analysis methods, more specifically mode shapes of eigenvalues, were used to identify the interaction between generators located in different synchronous grids, which are interconnected with a dc grid. The interaction arises from the shared control of dc voltage when operating under dc voltage droop control, which is the most appropriate control strategy for an MTDC. Poorly damped electromechanical modes are observable not only in the synchronous area where they originated from but also in other synchronous areas that linked through an MTDC. It was found that, though low in magnitude, generators located in asynchronous grids interconnected through an MTDC oscillated against each other. Furthermore, the effect of converter type, dc grid control and operation strategy on the level of the identified interactions was analyzed.

ii. Analysis of decentralized MTDC controllers interaction

One of the ancillary services that can be provided by dc grids to connected ac grids is power oscillation damping. Decentralized control techniques used in the analysis of multi-input-multiple-output systems were applied to assess the performance of and interaction between power oscillation damping controllers at different terminals of a dc grid. It was found that the performance of the controllers could be augmented or deteriorated due to the interaction between the decentralized controllers.

iii. Coordinated control of MTDC converters to increase global frequency stability

Coordinated control strategy for MTDC converters connected to several ac grids and an offshore wind farm was proposed. The proposed controller maximizes frequency support contribution of the wind farm to one ac grid and, at the same time, minimizes frequency disturbance in other ac grids connected to the MTDC.

1.3. Scope

The PhD work focuses on stability and control of a power system where more than one synchronous ac grids are connected to the same dc transmission system, which is referred to in the thesis as a hybrid ac/dc power system. Figure 1-1 illustrates the scope of the power system. Each ac grid can be connected to one or more terminals of the dc grid. A dc grid that has all its terminals connected to a single synchronous system, also known as embedded MTDC, is not within the scope of this work. The ac grids represent large power systems with multiple machines. Generator excitation and turbine/governor systems are included in order to capture important dynamics in each ac grid. Both point-to-point HVDC and multi-terminal types of dc transmission systems are included in this work. Different types of MTDC grid control strategies are considered. Furthermore, ancillary services provided to connected ac grids by the dc grid are covered in the PhD study.

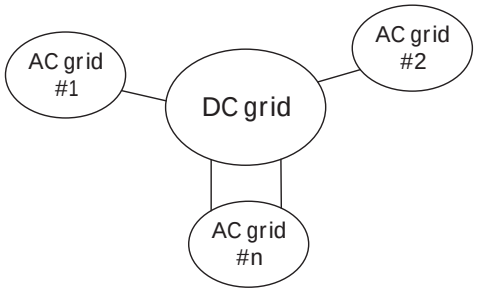

Figure 1-1 : The scope of the hybrid ac/dc power system in the thesis

The work is mainly concerned with stability analysis of a hybrid ac/dc power system, with a special focus on ac power systems' dynamics. The dashed circle in Figure 1-2 indicates the types of power system stabilities considered in the thesis. The period of interest for the stability studies ranges from seconds to minutes. Therefore, the hybrid grid is modelled accordingly with generator rotor and generator/converter controller behaviors dominating the dynamics in the system. Hence, fast electro-magnetic transients associated with voltages and currents in ac grids and switching of power electronics devices in converters are ignored. Small-signal/Modal analysis is used to study interaction between asynchronous ac grids connected through the dc grid and ac/dc interactions. Frequency stability analysis of the global hybrid grid is carried out using time domain analysis. Furthermore, interaction between decentralized controllers in the dc grid is studied using decentralized control techniques. DIgSILENT *PowerFactory* and MATLAB/Simulink are used to simulate and analyze the hybrid power system. Symmetrical and balanced conditions are assumed in the ac grids and only RMS simulations are conducted. The PhD research work does not cover ac or dc protection and harmonics studies.

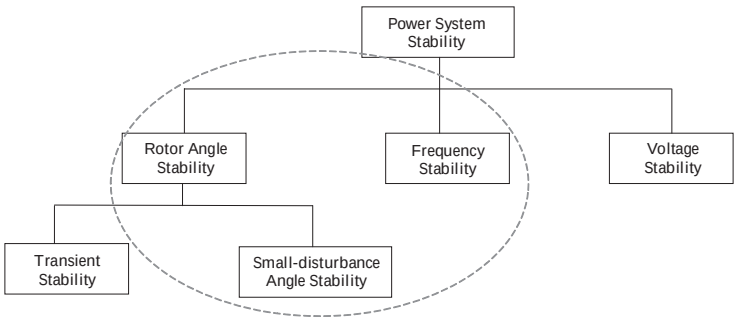

Figure 1-2 : Classification of power system stability [22]

1.4. List of publications

Some of the results in this PhD work are published in:

1. A. G. Endegnanew, J. Beerten, and K. Uhlen, "Dynamic interactions between ac synchronous grids interconnected through an MTDC grid," in *CIGRE Symposium*, Lund, 2015.

2. A. G. Endegnanew and K. Uhlen, "Investigation of dynamic behavior of hybrid ac/dc power system," *14th Wind Integration Workshop 14th Workshop on Large-Scale Integration of Wind Power into Power Systems as well as on Transmission Networks for Offshore Wind Power Plants Proceedings*, Brussels, 2015

3. A. G. Endegnanew and K. Uhlen, "Coordinated Converter Control Strategy in Hybrid AC/DC Power Systems for System Frequency Support," *Energy Procedia,* vol. 94, pp. 173-181, 2016.

4. A. G. Endegnanew, K. Uhlen, G. Bergna-Diaz, and J. Beerten, "Small-Signal Modelling of an MMC-Based HVDC Link Interfacing Large AC Systems," in *2016 IEEE 17th Workshop on Control and Modeling for Power Electronics (COMPEL)*, Trondheim, 2016, pp. 1-9.

5. A. G. Endegnanew and K. Uhlen, "Global Analysis of Frequency Stability and Inertia in AC Systems Interconnected through an HVDC," in *2016 IEEE International Energy Conference (ENERGYCON)*, Leuven, 2016, pp. 1-6.

6. A. G. Endegnanew, L. Kalemba, K. Uhlen, "Using Decentralized Control Techniques for Interaction Analysis in Hybrid AC/DC Grids", submitted to *IET Generation, Transmission & Distribution*

Publication within the topic of PhD research but not part of the thesis:

7. A. G. Endegnanew, G. Bergna-Diaz, K. Uhlen, "Avoiding AC/DC Grid Interactions in MMC Based MTDC Systems", *2017 Twelfth International Conference on Ecological Vehicles and Renewable Energies (EVER)*, 2017, pp. 1-8

8. A. G. Endegnanew, K. Uhlen, T. M. Haileselassie, and O. Anaya-Lara, "Transient Stability Analysis in Multi-Terminal VSC-HVDC Grids," in *2016 Power Systems Computation Conference (PSCC)*, 2016, pp. 1-7.

9. T. M. Haileselassie, A. G. Endegnanew, and K. Uhlen, "Secondary Control in Multi-Terminal VSC-HVDC Transmission System," in *2015 IEEE Power & Energy Society General Meeting*, 2015, pp. 1-5.

10. R. E. Torres-Olguin, A. R. Årdal, H. Støylen, A. G. Endegnanew, K. Ljøkelsøy, and J. O. Tande, "Experimental Verification of a Voltage Droop Control for Grid Integration of Offshore Wind Farms Using Multi-terminal HVDC," *Energy Procedia,* vol. 53, pp. 104-113, 2014.

Other publications during the PhD period:

11. A. G. Endegnanew, K. Satertro, S. Gjerde, H. Svendsen, O. Anaya-Lara, J. O. Tande*, et al.*, "Integrated modelling platform for floating wind turbine dynamic performance assessment," *Energy Procedia,* vol. 80, pp. 376-391, 2015.

12. M. Santos-Mugica, E. Robles, A. G. Endegnanew, E. Tedeschi, and J. Giebhardt, "Grid integration and power quality testing of Marine Energy Converters: Research activities in the MaRINET Project," in *2014 Ninth International Conference on Ecological Vehicles and Renewable Energies (EVER)*, 2014, pp. 1-9.

13. T. Toftevaag, A. G. Endegnanew, H. Seljeseth, R. Paulsen, "Resonansproblem i fordelingsnett knyttet til kondensatorer for fasekompensering - målinger, simuleringer, analyser", *NEF Teknisk møte 2014 Strømmen skal fram*, Trondheim, 2014.

14. T. K. Vrana, H. G. Svendsen, A. G. Endegnanew, “Wind Power Grid Codes: Historic Development, Present State and Future Outlook” *14th Wind Integration Workshop 14th Workshop on Large-Scale Integration of Wind Power into Power Systems as well as on Transmission Networks for Offshore Wind Power Plants Proceedings*, Brussels, 2015.

1.5. Outline of the thesis

The remaining of the chapters in this thesis are organized in the following way. Chapter 2 gives an overview of HVDC transmission systems: development, technology, and control. Chapter 3 describes the modelling of components and controllers, which are building blocks of a hybrid ac/dc grid. Chapter 4 describes methodologies used in the thesis to analyze dynamic interactions between ac grids, dc grid, and controllers. Chapters 5 uses modal analysis methods to assess interaction between asynchronous ac grids connected through an MTDC. In Chapter 6, control loop interaction between power oscillation damping controllers inserted into MTDC converters is assessed using decentralized control techniques. Chapter 7 presents a global analysis of frequency stability when MTDCs are involved in ac grid frequency and inertia support. The last chapter, Chapter 8, concludes the findings of the thesis and gives suggestions for future works.

2. High Voltage Direct Current Transmission Systems

High Voltage Direct Current (HVDC) transmission systems comprise of at least two converter stations that are connected to each other with dc transmission lines or cables. They are used for high voltage and high power transfer in a form of direct current between connected ac buses located in one or more synchronous systems. HVDC transmission systems with only two converter stations are referred to as point-to-point HVDC links or simply HVDC links, while HVDC transmission systems with more than two converter stations are referred to as multi-terminal high voltage dc (MTDC) grids or simply dc grids.

The first point-to-point HVDC link in the world was a 98 km long submarine cable connection built in 1954. It had 20 MW rating at 100 kV and connected Gotland Island with mainland Sweden. Since then, there has been a rapid development in cable and converter technologies. Today, HVDC links with ratings reaching 8000 MW at ±800 kV are in service, while an HVDC link with a rating of 12000 MW at ±1100 kV is currently under development in China [23]. The three terminal Hydro-Quebec/New England and Italy/Corsica/Sardinia MTDCs, which were built almost three decades ago, are the only dc grids that are operational today. Recently, MTDC grids that use a different type of converter technology have been commissioned [24, 25] in China in a pilot phase for interconnection of islands, offshore wind farms, and the main grid, while several other MTDC projects are at various stages of development [23, 26-29].

HVDC transmission systems will play an important role in bulk power transfer, interconnection of different power systems, integration of renewables, connection of offshore oil and gas platforms and refurbishment of aging/stressed ac grids. In addition, they will contribute to the robust, flexible and secure operation of ac grids through power flow control, voltage regulation, reactive power support, power oscillation damping etc.

This chapter gives a general overview of HVDC transmission systems, particularly MTDC grids. Section 2.1 discusses reasons for choosing HVDC over the traditional, widely used and well-understood high voltage ac transmission system. The main drivers and current challenges for HVDC transmission systems are addressed in Section 2.2. Converter technology, topology, and control of the systems are presented in Sections 2.3, 2.4 and 2.5, respectively. Section 2.6 summarizes the chapter.

2.1. Why HVDC?

Generally, high voltage dc transmission is considered over high voltage ac (HVAC) transmission for technical or economic reasons. The technical reasons are associated with reactive power transfer in ac transmissions. In ac transmission, overhead lines absorb reactive power causing the voltage to drop along the line when loaded close to their ratings. AC cables, on the other hand, are highly capacitive and generate reactive power. The excess reactive power limits the active power transmission capacity of cables. In both overhead ac lines and underground ac cables, different reactive power compensation techniques can be used to regulate voltage and maximize power transfer capacity. However, as the distance gets longer, active power transmission capability is reduced, requiring compensation at short intervals along the transmission, especially for cables. The fact that there is no reactive power in HVDC systems makes them suitable for long distance bulk power transmission. Another technical reason for using dc transmission is a non-synchronous interconnection of power systems. For example, the HVDC links are used to connect 50 Hz and 60 Hz grids in Japan and Paraguay/Brazil.

The economic reasons for choosing HVDC over HVAC are associated with investment and operational costs. Beyond a certain distance, the investment cost of ac transmission systems and the compensation devices needed become comparable with the investment cost of the converters, filters, and cables in dc transmission systems. The break-even distance is approximately 600-800 km for overhead lines and around 100 km for high voltage cables. DC transmission requires a lower number of conductors and lower level of insulation than ac transmission. Furthermore, for similar voltage and power ratings, the transmission losses are lower in dc transmission than ac transmission due to the absence of reactive current and skin effect. However, it should be noted that converter losses are introduced in dc transmission systems.

Aside from the technical and economic reasons, limited right of way, especially in congested areas, environmental impact, public resistance, long and difficult permitting process for building new ac transmission lines are also factors for preferring HVDC over HVAC.

It is worth mentioning that research efforts are being made to extend the transmission distance of ac cables, especially for offshore applications. Some of the ideas include using (mid-way) compensations, variable transmission frequency for offshore wind farm connection [30, 31] and using lower operating voltage than the rating of the cables [32]. A

163km long 100 kV/55MW ac submarine cable connecting Martin Linge offshore oil and gas field in the North Sea to the Norwegian power grid is the longest subsea ac cable in the world. A static var compensator is used onshore for voltage control [33, 34].

The merits of HVDC systems include asynchronous connection, bulk power transfer over long distance (especially for underground and subsea applications), lower losses for long distance transmission, active power flow control, the absence of reactive power flow, limiting fault propagation and lower requirements for right of way. In addition, the converters can provide ancillary services to connected ac grid, as long as it is within the capability/availability of the converters. The demerits of HVDC are high investment cost, the requirement of filter and converter losses. As in any project, cost benefit analysis would be done for each case before deciding to use HVAC or HVDC.

2.2. Drivers and challenges

Some of the driving forces behind the increased number of HVDC installations and interest in MTDC grids are the integration of renewables, deregulation of the electricity market, aging power system that needs upgrade or reinforcement, and growing demand in load centers that are far from power generation sites [35, 36].

Integration of renewable energy sources (RES) into power grids has taken off in the last decade, strongly driven by energy policies and support schemes. Both large scale and distributed solar and wind power have proliferated in the power system. Public resistance to large-scale wind farms and lack of suitable onshore sites have made offshore sites an attractive alternative for building wind farms. A higher amount of energy can be harvested from an offshore site than an onshore site for the same rating of a wind farm, as there is more stable and sustained wind at offshore sites. HVDC links are used to transfer the generated power to onshore grids for offshore wind farms located close to 100km or more. Today, there are several HVDC links connecting offshore wind farms in the North Sea to onshore grid connection points with ratings up to ±320 kV and 900 MW. BorWin1, DolWin1, HelWin1 and BorWin2 are a few of the offshore wind farms that are connected to the German transmission grid through an HVDC links, while more are under construction.

Wind and solar power plants result in variable and intermittent production due to the inherent characteristics of the renewable resources. Therefore, balancing power is needed to compensate and reduce the power fluctuation in the grid. As the deregulation of the

electricity market has enabled cross-border electricity trading, the balancing power can come from other countries. Moreover, in times of surplus production, power from renewables can be traded at a low marginal price. This has been one of the driving factors for the increased number of HVDC interconnections between Scandinavia, continental Europe and the UK [37, 38].

Another reason for having more HVDC transmission is the aging and constrained power system that needs to be replaced or upgraded. There is a difficult and long permitting process for building of new ac transmission lines due to public resistance and environmental concerns. Therefore, HVDCs are considered to replace ac lines and provide higher power transfer capacity using existing right of ways. In addition, this would allow improved power flow control, a minor modification of existing lines and underground installations in populated areas. Furthermore, overlay MTDC concepts as a super grid [39-41] have been suggested as a comprehensive solution for integration of renewables, security of supply, congestion management, and for competitive and integrated power markets.

In addition, HVDC systems are increasingly being used for remote generation and load connection applications. In countries like Brazil, China and India, the supply of the ever-growing load demand in large cities from hydro and wind power plants located at remote sites is one of the drivers behind the increased number of HVDC installations. The oil and gas platforms in the North Sea that are connected to the Norwegian grid via HVDC links [42] are examples of remote loads connection application of the transmission system.

An MTDC grid is a large and complex infrastructure, which would require a lot of investment and time to build. Thus, MTDCs grid will most likely develop in a gradual and modular manner. Some of the challenges related to the development of dc grids are [36, 43, 44]:

- *Technology*

  DC circuit breakers that can detect and quickly interrupt dc fault currents have not yet been applied in large-scale projects. Therefore, there is a lack of knowledge and experience in control and protection of dc grids. The existing dc grids are operated with protection on the ac side. This means that in the case of a fault in the dc grid, the entire dc grid is put out of service, instead of isolating only the faulty line/equipment. In addition, high power dc-to-dc converters that can be used for

voltage level conversion and control of power flow in different branches of meshed dc grids are not available.

- *Standardization*

  The converters in each HVDC link built so far are delivered by a single manufacturer with their own control configurations and voltage levels. However, in meshed dc grids, the different components will be delivered by multiple vendors and, therefore, inter-operability of components from different manufacturers is crucial. In addition, standardization of voltage levels and performance requirements are vital for the emergence of dc grids.

- *Regulation*

  MTDC grids will interconnect multiple ac grids operated by multiple transmission system operators (TSOs). Whether the dc grid is operated by an independent TSO or by the multiple TSOs connected to the grid, a regulation is needed to define operation, maintenance and market integration of the grid. In addition, regulation is imperative to distribute both benefits and responsibilities (including cost) related to the dc grid.

2.3. Technologies

HVDC transmission systems can be categorized into Line Commutated Converters (LCC) and Voltage Source Converters (VSC) depending upon the type of converters used at the terminals.

2.3.1. LCC

LCC utilizes semi-controllable thyristor switches in the current source converters. Thyristors are turned on by control signal but are turned off when the current flowing through them goes to zero. Therefore, the converter uses the external grid for commutation. LCC has a two-quadrant operation; i.e. the current has uni-directional flow but the dc voltage can have either positive or negative polarity. As the current direction can not change, power flow reversal is achieved by changing dc voltage polarity, which complicates their use in MTDC topology. Active power can be controlled by LCC but not reactive power. Therefore, capacitor banks and capacitive filters are used to supply the reactive power absorbed by the converter and its transformer, which can reach up to 50-60% at rated load. In addition, other compensation devices such as synchronous

condensers or Flexible AC Transmission System (FACTS) devices can be used. Furthermore, tuned filters are required to remove low frequency harmonic currents generated on the ac side of the converter.

An LCC converter station has a large volume, mainly due to the filtering and compensation devices needed for proper operation of the system. This combined with the fact that LCC requires strong grid to connect to makes LCCs unattractive for offshore applications where space is a constraint. In addition, LCCs do not have fault ride through and black start capability and are susceptible to commutation failure. These issues are not of concern in VSC-based HVDC systems.

2.3.2. VSC

A VSC converter has insulated-gate bipolar transistor (IGBT) switches that operate at switching frequency higher than the grid frequency. IGBTs are turned on and off by control signals and do not require external grid for commutation. Both current direction and voltage polarity can be changed allowing a four-quadrant operation of the converter. Thus, power flow reversal can be achieved by changing the direction of the current while keeping the polarity of dc voltage constant. Figure 2-1 shows a block diagram of components in a typical VSC converter station.

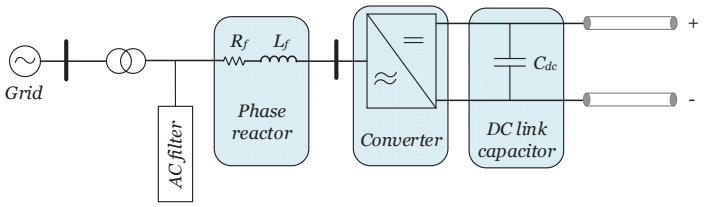

Figure 2-1 : VSC station components

The VSC is connected to the ac grid through a phase reactor and a transformer. Independent control of active and reactive power flowing into the grid is realized by controlling the current flowing through the phase reactor. The ac filters are tuned to eliminate the high-order voltage harmonics caused by the high frequency switching of the IGBTs, while the dc link capacitor acts as dc voltage source to the converter, and filters out dc voltage ripples caused by switching in the converter.

VSC can be a two-level, three-level or modular multi-level converter. A two-level converter switches between two voltage levels: either between $v_{dc}/2$ and $zero$ or between $v_{dc}/2$ and $-v_{dc}/2$. A three-level converter can switch between $v_{dc}/2$, $zero$ and $-v_{dc}/2$ because of a neutral point clamping that provides a third voltage level. A Modular Multi-level Converter (MMC) consists of hundreds of series connected bi-directional chopper cells called sub-modules. By inserting and isolating the sub-modules, the converter can switch in a large number of small steps between $v_{dc}/2$ and $-v_{dc}/2$. In two-level VSC, Pulse Width Modulation (PWM) technique varies the polarity of dc voltage and width of the pulse to generate converter ac voltage of desired magnitude, phase angle and frequency. Therefore, the voltage at the converter end is the output of PWM plus and minus values with different widths. On the other hand, in MMC converters, the output is close to a sinusoidal voltage with only high-order harmonics due to the large number of small steps. Hence, the filtering requirement for voltage output of MMCs is significantly reduced compared to 2-level VSCs.

To summarize, both LCC and VSC technologies are in use today. Even though LCC based systems have the aforementioned drawbacks, they have lower losses than VSC based systems and can handle higher voltage and power ratings. However, the introduction of MMC has brought forth attractive features such as modularity, scalability and higher availability due to the redundancy of the large number of submodules. In addition, converter losses are lower in MMCs than two/three-level VSCs, though not as low as LCC. Regardless, VSC is the technology that is suitable for offshore applications due to low footprint, ability to connect to weak grids, black start capability and control of both active and reactive power. Furthermore, VSC is the most appropriate technology for MTDC grids as fixed dc voltage polarity enables easier parallel connection of converters. Moreover, power flow reversal by changing current direction allows uninterrupted dc grid operation for both positive and negative power flows.

As the main focus of this thesis work is hybrid ac/dc grids with both ac grids and MTDC grids, hereinafter, HVDC link or dc grid refers to VSC based HVDC systems.

2.4. Topology

An HVDC transmission can have a monopolar, symmetric monopolar or bipolar configuration. A monopolar configuration has one converter at each end of the dc line. It uses a single conductor and metallic return or the earth. A symmetric monopolar configuration also has one converter at each end of the dc line, but it has two conductors

with opposite polarity. On the other hand, bipolar configuration has two converters connected in series at each end of the dc line with their connection point grounded. In case of fault on one of the converters of a bipolar system, the system can continue to operate as a monopolar system.

2.5. HVDC transmission system control

Typically, in point-to-point HVDC links, one terminal controls active power while the other terminal regulates dc voltage. On the other hand, MTDC terminal converters can operate in various types of active power and/or dc voltage control modes. Below is a brief review of the master-slave, voltage margin, dc voltage droop and dead-band droop control modes discussed in [18, 45, 46]. The active power versus dc voltage characteristics of each control mode is shown in Figure 2-2.

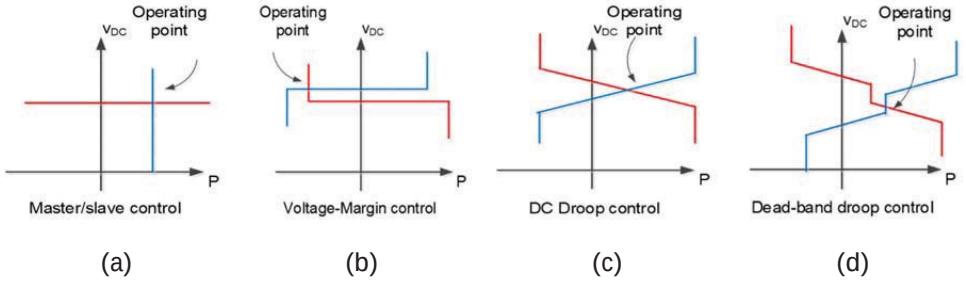

Figure 2-2 : Power vs. dc voltage characteristics of different types of MTDC converter terminal control strategies [45]

- *Master-slave control mode* is an extension of point-to-point HVDC control. In this control mode, one terminal controls dc-link voltage, while the remaining terminals control power flow, see Figure 2-2(a). The terminal controlling dc voltage balances any power flow variation in the dc grid and behaves like the slack bus in the system. The drawbacks of this control mode are large strains on the slack bus, as it is responsible for all balancing power, and the system is entirely dependent on the slack bus, which fails to meet the N-1 contingency criterion. In addition, the slack bus may need to be oversized.

- *Voltage margin control* is a modified version of master-slave control where constant power and constant dc voltage control characteristics are combined. The relationship between power and dc voltage for this control mode is illustrated in Figure 2-2(b).

Terminal nodes operate in constant power control in a certain voltage range and they switch to constant dc voltage control operation mode outside of this range. However, during steady state, master slave control mode applies and the problem related to one terminal being exposed to large power flow strains remains. In addition, when switching between control modes occurs, power transfer to the converter changes very fast, possibly causing a disturbance in the ac grid.

- *DC voltage droop control* is a distributed type of control where more than one terminal participates in active power and dc voltage control. In this control mode, there is a linear relationship between power flow and dc voltage at the MTDC terminal as shown in Figure 2-2(c). The slope of the linear curve is determined by a droop constant. DC voltage droop control neither requires communication nor is the system dependent on a single terminal. For these reasons, it is considered to be the most appropriate type of control mode for MTDC grid operation.

- *Dead-band droop control* mode, shown in Figure 2-2(d), is a combination of voltage margin and droop control modes. In this control mode, a terminal operates in constant power control for a given voltage range, and outside this range, it operates in dc voltage droop control mode. As in the case of voltage margin control, dead-band droop control allows discrimination between normal and disturbed operation conditions.

2.5.1. Hierarchical MTDC control structure

Power flow control in dc grids can have a hierarchical structure that is similar to ac grid power flow control. The initial power flow schedules will be set based on some market arrangement (day-ahead or intra-day), but there will naturally be deviations from schedules in real-time, e.g. due to forecast errors in wind power production feeding into the dc grid or outage of a converter. These deviations are managed through primary, secondary control and tertiary control stages.

As in the case of an ac grid, primary control in MTDC is the response of the system to a sudden change in power balance in the grid. In dc voltage droop control, more than one converter participate in dc voltage control and share compensation of the power imbalances. However, when fixed droop constants are used, power imbalance sharing is carried out proportionally according to converters' droop parameters and does not take into account the available capacity of the individual converter to take on more power flow.

This may lead to overloading of converters that were operating close to their ratings. To overcome this problem, an adaptive (variable) droop control can be used where droop constants are varied based upon the loading of the converter, thereby making converters with higher available headroom compensate for a larger share of the imbalance than converters operating close to their limits [47]. Note that the impact of the new droop parameters on the stability of the MTDC grid needs to be ascertained prior to implementation.

Secondary control in ac grids restores system frequency, and power flows in tie lines are returned back to scheduled levels. Unlike frequency, however, voltage in an MTDC is not a universal parameter and the dc terminal voltage variations in an MTDC resulting from the action of primary control are influenced by the dc line resistances, dc grid topology and location of power deficit/ surplus [16]. Therefore, the option of dc voltage restoration will not be straightforward as in the case of frequency restoration in an ac grid. On the other hand, power flow via the converters can be treated as a tie-line power flow, in which case the main purpose of secondary control in MTDC becomes to restore power flow at selected terminals back to original (scheduled) levels [19, 48-50]. It can be argued that restoration of power flow to originally scheduled levels (at some terminals) is more important than restoring dc voltages. Furthermore, power flow restoration to the scheduled levels will partially restore the dc bus voltage levels close to the original references. Other types of secondary controllers with optimal power flow (OPF) based algorithms have been proposed for bringing average voltage profile back to pre-disturbance operating condition [51] and minimizing cable and/or converter losses in MTDC grids [20].

In addition to the two control stages presented above, tertiary control acting at higher hierarchical level and involving system operator's action can also be included in MTDC power flow control.

2.5.2. Ancillary services

Large conventional generators and FACTS devices typically provided ancillary services that are vital for stable operation of a power system. However, nowadays, HVDC systems are also expected to provide such services as their use in the power system has increased. To this end, a considerable amount of research has been conducted on the provision of ancillary services from HVDC systems [52-58] and from renewable energy sources that are connected to the ac grid through HVDC systems [59-68]. Furthermore, grid codes are

being updated to include ancillary service requirements from HVDC systems to ensure continuous, secure and stable operation of the electrical grid.

The fast and independent active and reactive power control capability of VSC based HVDC system makes them suitable for provision of such services. The converters can produce reactive power locally limited only by the current rating of the power electronics. However, the converters do not produce the active power needed for ancillary services such as frequency and inertia support, unless the capacitive energy stored in the capacitors in the dc grid is used, which is very limited and can only last for a short period. Therefore, a converter's active power controller is modified and the HVDC system is in effect used to facilitate sharing of active power reserves between ac grids (and wind farm if any) connected to different terminals. It should be noted that for wind power plants to be able to render ancillary services, their controllers need to be modified and some equipment may need to be overrated. In addition, their power output may be curtailed during the service provision period, meaning operation at non-optimal generation level. This may entail added investment cost and lost income for plant owners.

In August 2016, the European Network of Transmission System Operators for Electricity (ENTSO-E) officially published the Network Code on High Voltage Direct Current Connections (NC HVDC) [69]. The grid code specifies requirements for grid connections of HVDC systems (both HVDC and MTDC) and dc-connected power park modules. It is expected that ENTSO-E's TSO members will use NC HVDC as a guideline while developing their own respective grid codes. Provision of ancillary service to connected ac grids is one of the requirements stated in the grid code. The required ancillary services include active power and frequency control, voltage and reactive power control and provision of damping torques.

- *Active power, Frequency and inertia support*: The active power flow at the converters' connection terminals can be modulated as a function of the frequency deviation from nominal value at the connection point in order to maintain stable system frequency. In addition, the HVDC systems are capable of rapidly adjusting their active power flow in order to limit the rate of change of frequency or provide a synthetic inertia.

- *Reactive power and voltage control*: The terminal converters can control reactive power and voltage at the ac connection points regardless of the active power flow. Thus, they behave as a Static Synchronous Compensator (STATCOM).

- *Power oscillation damping*: Furthermore, the systems are capable of contributing to the damping of power oscillations in connected ac networks, including electrical damping of torsional frequencies for damping of sub-synchronous torsional interaction (SSTI).

2.6. Chapter summary

This chapter gave a general overview of HVDC transmission systems, with a particular focus on MTDC grids. Technology, topology and control of HVDC systems were presented. In addition, main drivers and challenges for the development of HVDC transmission systems were discussed.

3. Modelling of hybrid ac/dc system

The power system is modelled with differential and algebraic equations (DAE). The first order differential equations describe the dynamics of the system, while the algebraic equations arise from the assumption that fast variables have already reached their steady state on the time horizon of interest [22, 46].

In electro-mechanical simulation studies, voltages and currents in ac grids are represented by time-varying phasors ignoring fast electro-magnetic transients (EMT). In addition, symmetrical components are assumed and lumped parameters are used instead of distributed parameters, for example in transmission lines. These approximations reduce computational burden and allow simulation of electromechanical transients in large and complex power systems. Generators are modelled by the dynamics associated with their rotors. On the other hand, average value models of converters are suited for integrated simulation of ac and dc grids. In these models, switching dynamics of the power electronics devices are neglected and the converter is regarded as a voltage source with controlled amplitude and phase angle.

This chapter presents differential and algebraic equations (DAE) that describe the dynamic behavior of the various components of an ac/dc power system, i.e. synchronous generators, power converters, and dc cables. The different DAE equations are combined to form an ac/dc power system model, which can be used for dynamic performance and control analysis of the system.

3.1. AC grid

An ac power system is composed of multiple generating units with controllers, loads, transmission lines and other devices that are essential for the proper and stable operation of the system. This section presents mathematical models that describe the dynamics of the main components of an ac grid: generators, exciters, turbines and their controllers.

3.1.1. Synchronous generators

Synchronous generators are modelled with a 6th order model, which represents machines with damper windings on both d- and q- rotor axes. The d-axis is aligned with the magnetic axis of the field windings, and the q-axis lags d-axis by 90 electrical degrees. In this model, the effect of rotor damper windings and field winding on the flux linkage is

considered, and the differential equations describe the change in the induced emfs as the flux linking the rotor circuit decays. The first order differential equations for a synchronous generator model are [70]:

$$\begin{aligned}
&\frac{d}{dt}\delta = \omega_0\left(\omega - \omega_s\right) = \omega_0\Delta\omega \\
&\frac{d}{dt}\Delta\omega = \frac{1}{2H}\left(P_m - P_e - D\Delta\omega\right) \\
&\frac{d}{dt}E_q^{'} = \frac{1}{T_{d0}^{'}}\left(E_{fd} - E_q^{'} + I_d\left(X_d - X_d^{'}\right)\right) \\
&\frac{d}{dt}E_d^{'} = \frac{1}{T_{q0}^{'}}\left(-E_d^{'} - I_d\left(X_q - X_q^{'}\right)\right) \\
&\frac{d}{dt}E_q^{''} = \frac{1}{T_{d0}^{''}}\left(E_q^{'} - E_q^{''} + I_d\left(X_d^{'} - X_d^{''}\right)\right) \\
&\frac{d}{dt}E_d^{''} = \frac{1}{T_{q0}^{''}}\left(E_d^{'} - E_d^{''} - I_q\left(X_q^{'} - X_q^{''}\right)\right)
\end{aligned} \tag{3.1}$$

where the subscripts d and q represent d- and q-axis components of each variable in the individual synchronous machine's rotor dq-axis. δ is the angle, in radians, between each machine's rotor q-axis and the reference machine's rotor q-axis. ω_0 is the rotor base angular speed in rad/s, ω is rotor speed, and ω_s is the synchronous speed or the speed of the reference machine. $\Delta\omega$ is deviation from synchronous speed in p.u.. E'' and E' are transient and sub-transient induced voltages while x, x' and x'' are synchronous, transient and sub-transient reactances, respectively, in p.u.. H is the inertia constant in seconds, and T_0' and T_0'' are the open-loop transient and sub-transient time constants, respectively. Field excitation voltages E_{fd} and mechanical power P_m are outputs of excitation and turbine/governor systems, respectively. The air gap electrical power, P_e, is calculated as:

$$P_e = E_d^{''}I_d + E_q^{''}I_q - \left(X_d^{''} - X_q^{''}\right)I_dI_q \tag{3.2}$$

The differential equations describing the generators are linked with the algebraic ac network equations through generator currents I_d and I_q.

Synchronous generator dynamics equations can also be written in terms of rotor flux dynamics as in [71-73]. Furthermore, the generators can be represented by reduced order of models, where the effect of damper winding, rotor body eddy currents and field

windings on the flux variation are neglected. For example, a second order or classical model, which is a model used widely for simplified dynamic analysis, assumes that the field excitation E_{fd} remains constant during transient state, and models the generator dynamics with only the first two equations in (3.1) or the swing equations.

In 6th order models, the generator is represented by subtransient emfs E_d'' and E_q'' behind subtransient impedances x_d'' and x_q'' as shown Figure 3-1.

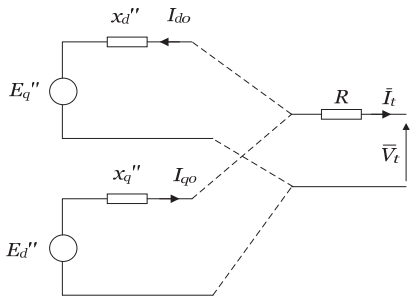

Figure 3-1 : Equivalent circuit diagram for a generator in the subtransient state

The subtransient voltages are calculated as:

$$\begin{bmatrix} E_d'' \\ E_q'' \end{bmatrix} = \begin{bmatrix} V_d \\ V_q \end{bmatrix} + \begin{bmatrix} R & X_q'' \\ -X_d'' & R \end{bmatrix} \begin{bmatrix} I_d \\ I_q \end{bmatrix} \tag{3.3}$$

where $\bar{V}_t = V_q + jV_d$ is generator terminal voltage and $\bar{I}_t = I_q + jI_d$ is generator terminal current flowing into the ac grid. Generator terminal voltages and currents are obtained from load flow calculations. Figure 3-2 shows phasor diagrams for $\bar{V}_t$ and $\bar{I}_t$. The Re-Im axes represent synchronous reference frame, while d_{rotor}-q_{rotor} axis represents the rotor dq-axis of a single synchronous machine. In a multi-machine system, one machine's rotor dq-axis is selected to be the synchronous reference frame, and the machine is referred as a reference machine. The synchronous reference frame is used in load flow calculation. Moreover, the rotor angle δ (in (3.1)) of all the other machines in the system is measured as the angle between their q-axis and the reference machine's q-axis.

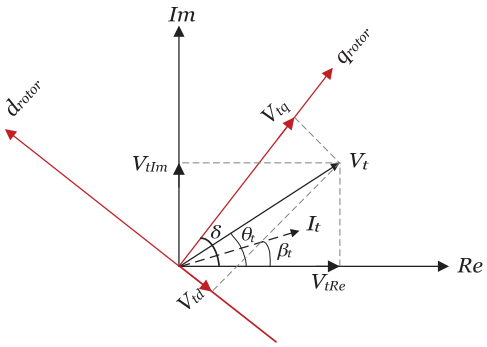

Figure 3-2 : Coordinate system definition

Note that q-axis is aligned with the real axis, while d-axis is aligned with the imaginary axis. Generator terminal voltage and current in the synchronous reference frame or Re-Im axis:

$$\begin{aligned} V_{t(Re\text{-}Im)} &= V_{tRe} + jV_{tIm} = |V_t|(\cos\theta_t + j\sin\theta_t) \\ I_{t(Re\text{-}Im)} &= I_{tRe} + jI_{tIm} = |I_t|(\cos\beta_t + j\sin\beta_t) \end{aligned} \tag{3.4}$$

Generator terminal voltage and current in a generator's rotor dq-axis frame are:

$$\begin{aligned} V_{g(d-q)} &= V_{gq} + jV_{td} = |V_t|\left[\cos(\delta-\theta_t) - j\sin(\delta-\theta_t)\right] \\ I_{g(d-q)} &= I_{gq} + jI_{td} = |I_t|\left[\cos(\delta-\beta_t) - j\sin(\delta-\beta_t)\right] \end{aligned} \tag{3.5}$$

The relationship between synchronous reference frame and generator's rotor dq-axis is according to the transformation:

$$\begin{aligned} \begin{bmatrix} Re \\ Im \end{bmatrix} &= \begin{bmatrix} \cos\delta & -\sin\delta \\ \sin\delta & \cos\delta \end{bmatrix} \begin{bmatrix} q \\ d \end{bmatrix} \\ Re + jIm &= (q + jd)e^{j\delta} \end{aligned} \tag{3.6}$$

3.1.2. Synchronous machine Controllers

For a wide range of operations, the generators should be able to participate in regulating voltage and frequency in the power system. This is achieved through excitation and

turbine/governor systems. Figure 3-3 shows an overview of excitation and turbine/governor systems and their connection with the generator and the grid.

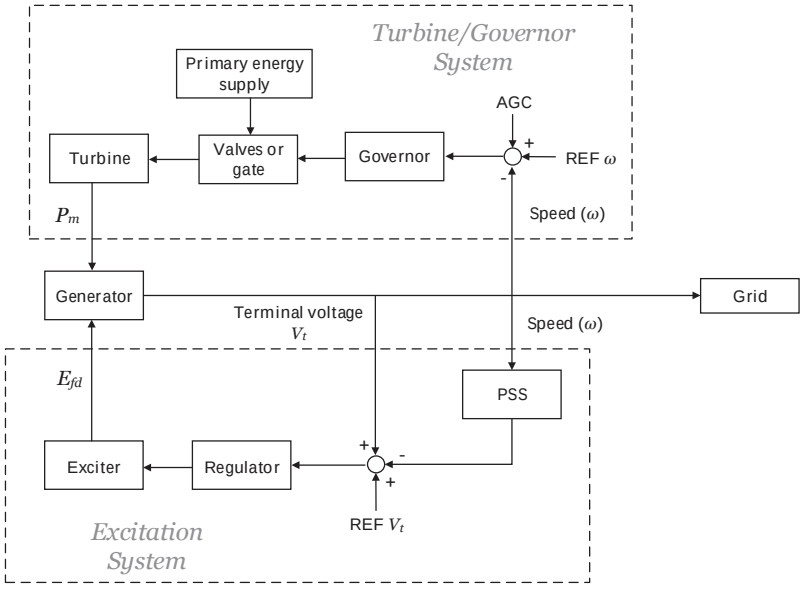

Figure 3-3: Synchronous generator control system

The following subsections briefly discuss the purpose of excitation and turbine/governor systems. In addition, the dynamic models of excitation and turbine/governor systems used in this thesis will be presented. The power system models used in this thesis represent a reduced equivalent model of a large power system, where several power plants and loads in an area are aggregated into few generators and loads. Thus, simple generic excitation and turbine/governor system models are used instead of specific types of generator controller models.

3.1.2.1. Excitation systems

An excitation system provides direct current to the field windings of a synchronous machine. It adjusts field voltage to change dc field current, which in turn changes the terminal voltage of the synchronous machine. An excitation system consists of a regulator, exciter, sensors, protective circuits, limiters and power system stabilizer. The regulator

compares measured and reference signals and provides actuating signal to the exciter. AC regulator maintains generator terminal voltage constant, while dc regulator, which is used at start up and as a backup in case of ac regulator failure, maintains constant field voltage. The exciter produces the field current according to the regulator signal. Sensors measure signals to be controlled, while protective circuits and limiters ensure that the capability of the synchronous generator and exciter are not exceeded. Power system stabilizer (PSS) provides damping torque for damping low frequency power oscillations in power systems. An excitation system contributes to effective voltage control and enhancement of system stability.

Figure 3-4 shows a simplified excitation system model (SEXS), which is used in this thesis. The governing equations for the model are listed in (3.7).

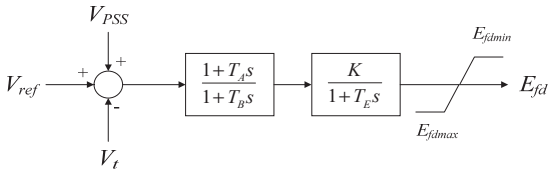

Figure 3-4: Simple excitation system (SEXS) model

$$\begin{aligned}\frac{d}{dt}E_{fd} &= \frac{1}{T_E}\left(Kx_{AVR}\left(1-\frac{T_A}{T_B}\right)+\frac{KT_A}{T_B}(V_{ref}-V_t+V_{PSS})-E_{fd}\right)\\ \frac{d}{dt}x_{AVR} &= \frac{1}{T_B}\left(V_{ref}-V_t+V_{PSS}-x_{AVR}\right)\end{aligned} \tag{3.7}$$

where T_A and T_B are lead-lag controller time constants, K is the controller gain parameter and T_E is the exciter time constant. E_{fd} is field voltage and x_{AVR} is a state variable associated with the lead-lag controller. The regulator takes in as an input reference voltage (V_{ref}), generator's terminal voltage (V_t) and output signal of the power system stabilizer (V_{PSS}).

A PSS improves power system dynamic performance by damping low frequency power oscillations that arise from groups of generators oscillating against each other. The PSS controller used in this thesis is a STAB1 and it uses rotor speed deviation as an input. It has a washout filter and two cascaded lead-lag controllers as shown in Figure 3-5. The DAE equations for the PSS are presented in (3.8).

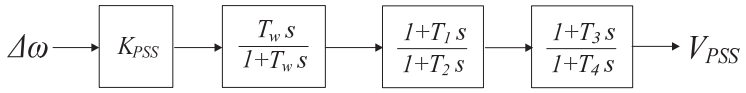

Figure 3-5: STAB1 power system stabilizer model

$$
\begin{aligned}
V_{PSS} &= \frac{T_1 T_3}{T_w T_2 T_4}\left(K_{PSS}\Delta\omega - x_{PSS3}\right) - \left(\frac{T_{1i} - T_2}{T_2 T_4}\right) T_3 x_{PSS2} - \frac{T_3 - T_4}{T_4} x_{PSS3} \\
\frac{d}{dt} x_{PSS1} &= \frac{1}{T_{wi}}\left(K_{PSSi}\Delta\omega - x_{PSS1}\right) \\
\frac{d}{dt} x_{PSS2} &= \frac{1}{T_w T_2}\left(K_{PSS}\Delta\omega - x_{PSS1}\right) - \frac{1}{T_{2i}} x_{PSS2} \\
\frac{d}{dt} x_{PSS3} &= \frac{T_1}{T_w T_2 T_4}\left(K_{PSS}\Delta\omega - x_{PSS3}\right) - \left(\frac{T_1 - T_2}{T_2 T_4}\right) x_{PSS2} - \frac{1}{T_4} x_{PSS3}
\end{aligned}
\tag{3.8}
$$

where $\Delta\omega$ is speed deviation from the reference, K_{PSS} is the controller gain constant, T_w is wash-out filter time constant, while T_1, T_2, T_3 and T_4 are lead-lag time constants. x_{PSS1}, x_{PSS2} and x_{PSS3} are states associated with the washout filter and lead-lag blocks.

3.1.2.2. Turbine/Governor systems

Turbine/Governor systems provide mechanical torque to the generator, and control speed/frequency and/or power/load. They consist of a governor, primary energy supply, valve/gate and turbine. A governor acts on speed/frequency error and controls valve/gate position. The valve/gate determines the amount of primary energy supply that goes into the turbine. The primary energy supply can be coal, water, gas, etc. The energy in these resources is converted into rotational energy by the turbine. The turbine drives the rotor of the synchronous machine. Typical turbine types are diesel/gasoline engines, steam turbines, hydro turbines, and gas turbines.

Governors are provided with droop characteristics to ensure stable parallel operation of multiple units. Droop is defined as the percentage change in speed required to move the valves from fully open to fully closed position[70]. If a linear relationship is assumed between the valve position and mechanical power output of the turbine, then the idealized power-speed characteristics become:

$$\frac{\Delta\omega}{\omega_n} = -\rho\frac{\Delta P_m}{P_n} \tag{3.9}$$

where ρ is droop constant in p.u., $\Delta\omega$ and ΔP_m are speed and turbine power output deviation from reference, while ω_n and P_n are rated speed and power, respectively. Typical p.u. droop values are between 4% and 12% with the lower values corresponding to turbo generators, and the higher values to hydro generators [70].

A simple steam turbine model, TGOV1, shown Figure 3-6 is used in this thesis. The model represents turbine-governor droop (ρ), the main steam control valve motion and limits (T_1, V_{MAX}, V_{MIN}) and a lead-lag block representing time constants associated with the motion of steam through the reheater and turbine stages [74]. D_t is a turbine damping constant, which represents a linearized approximation of the effect of speed on the power.

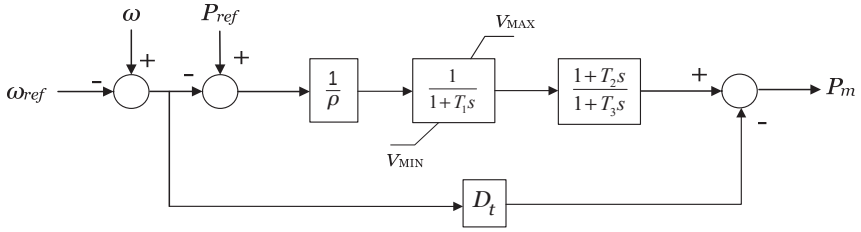

Figure 3-6: TGOV1 turbine-governor model [75]

The governing equations for TGOV1 model are:

$$\begin{aligned}
\frac{d}{dt}x_{GOV1} &= \frac{1}{T_1}\left(\frac{1}{R}\left(P_{ref} - \omega - \omega_{ref}\right) - x_{GOV1}\right) \\
\frac{d}{dt}x_{GOV2} &= \frac{1}{T_3}\left(x_{GOV1} - x_{GOV2}\right) \\
P_m &= x_{GOV1} + \left(x_{GOV1} - x_{GOV2}\right)\left(\frac{T_2 - T_3}{T_3}\right) - D_t\omega
\end{aligned} \tag{3.10}$$

where ω_{ref} and ω are reference and measured speeds, while P_{ref} is the generator load set point or power reference. x_{GOV1} is a state associated with the steam control valve and x_{GOV2} is a state associated with the lead-lag or the heater block.

3.2. DC grid

The dc grid model consists of converters and dc cables. In this section, dynamic models of Voltage Source Converters (VSC), both two-level converter and modular multi-level converter (MMC), and their controllers are presented. In addition, models of dc cables are included.

3.2.1. Voltage Source Converters

An average value model represents the converter as a voltage source producing a sinusoidal wave at fundamental frequency and neglects all other harmonics. This type of modelling allows fast simulation of large integrated ac/dc systems and is suitable for the study of small-signal, medium-term (time frame 400ms to 10s) and long-term (10s to several minutes) power systems dynamics in frequency domain or time-domain [76]. This section presents average value models of two-level and MMC converters, and their controllers that are used in the thesis.

Figure 3-7 shows a single line diagram of a VSC converter station.

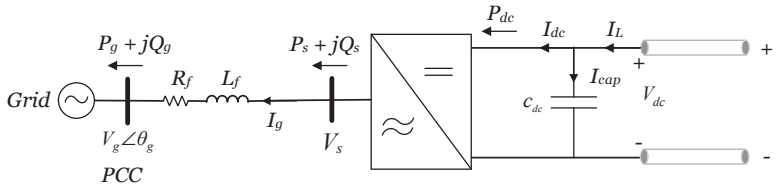

Figure 3-7 : VSC converter block diagram

The series impedance with R_f and L_f represents phase reactor, filters and transformer impedances, while V_s represents the internal VSC voltage. V_g is the voltage at the point of common coupling (PCC), which is the bus at which the converter station is connected to the grid. I_g is the grid current flowing from the converter to the grid.

In vector control, time varying three phase voltage and current are transformed into constant steady state values in dq-reference frame rotating at synchronous speed [77, 78]. Then, the magnitude and phase of V_s are varied to control the current flowing through the series impedance, thereby controlling active and reactive power flowing into the grid.

The voltage drop across the phase reactor in dq-reference frame is written as:

$$v_{s\_dq} - v_{g\_dq} = r_f i_{g\_dq} + \frac{l_f}{\omega_0}\frac{d}{dt} i_{g\_dq} + j\omega_{pll} l_f i_{g\_dq} \tag{3.11}$$

where the subscripts d and q represent d- and q-axis components of each variable in the rotating dq-reference frame, ω_o is base grid frequency ($2\pi f$) in rad/s, ω_{pll} is p.u. grid frequency measured by a Phase Locked Loop (PLL). Equation (3.11) is written in p.u. with $Z_{base} = \frac{V_{base}}{I_{base}} = L_{base}\omega_0$.

Rearranging (3.11) and expanding the equation, grid current dynamic equation in dq becomes:

$$\begin{aligned} \frac{d}{dt} i_{gd} &= \frac{\omega_o}{l_f}\left(v_{sd} - v_{gd} - r_f i_{gd} + \omega_{pll} l_f i_{gq}\right) \\ \frac{d}{dt} i_{gq} &= \frac{\omega_o}{l_f}\left(v_{sq} - v_{gq} - r_f i_{gq} - \omega_{pll} l_f i_{gq}\right) \end{aligned} \tag{3.12}$$

The active and reactive power flowing into the grid are calculated as:

$$\begin{aligned} S_g &= v_{g\_dq}\left(i_{g\_dq}\right)^* \\ P_g &= v_{gd} i_{gd} + v_{gq} i_{gq} \\ Q_g &= -v_{gd} i_{gq} + v_{gq} i_{gd} \end{aligned} \tag{3.13}$$

If losses in the converter are assumed to be negligible, then active power on the ac side of the converter equals power on the dc side.

$$\begin{aligned} P_s &= P_{dc} \\ v_{sd} i_{gd} + v_{sq} i_{gq} &= v_{dc} i_{dc} \end{aligned} \tag{3.14}$$

The voltage across the dc-link capacitor is calculated as:

$$\frac{d}{dt} v_{dc} = \frac{1}{c}\left(i_L - i_{dc}\right) \tag{3.15}$$

where i_{dc} is the dc current flowing into the converter and i_L is the current flowing from the dc cable as depicted in Figure 3-7.

The rotating dq- reference frame used in converter control has q-axis leading the d-axis by 90°. In addition, the d-axis is aligned with the real axis, while q-axis is aligned with the imaginary axis. This is different from the dq-axis definition used in synchronous machine modelling (and the synchronous reference frame) described in Section 3.1.1. Figure 3-8 shows the two reference frames. In synchronous generator modelling rotor dq-axis, the d-axis leads q-axis by 90° and its q-axis is aligned with the positive real axis.

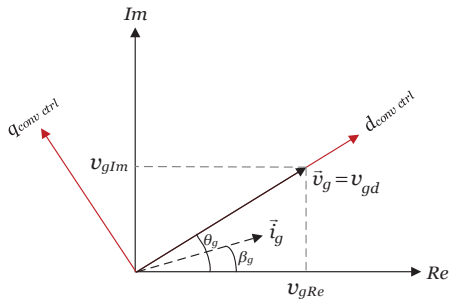

Figure 3-8 : Rotating dq-axis in converter control and synchronous reference frame

In Figure 3-8, the point of common coupling (PCC) voltage vector ($\vec{v}_g$) is perfectly aligned with the d-axis used in converter control. This is an ideal case where the converter dq-reference frame is rotating at a synchronous speed and the phase locked loop (PLL) estimates the PCC voltage angle accurately. The PLL estimates PCC voltage angle and continuously tries to align $\vec{v}_g$ with the d-axis of the converter dq- rotating reference frame. This makes v_{gq} equal to zero and makes decoupled control active and reactive power possible. With v_{gq}=0, active and reactive power equations in (3.13) become only proportional to d and q axis currents, respectively.

$$\begin{aligned} P_g &= v_{gd} i_{gd} \\ Q_g &= -v_{gd} i_{gq} \end{aligned} \tag{3.16}$$

Thus, i_{gd} and i_{gq} can independently be controlled to control P_g and Q_g. The PCC voltage and grid current in the converter dq-axis reference frame is:

$$v_{g\_dq} = v_{gd} + jv_{gq} = |\vec{v}_g|\left[cos\left(\theta_g - \theta_g\right) - j\,sin\left(\theta_g - \theta_g\right)\right]$$
$$\Rightarrow v_{gd} = |\vec{v}_g| \quad v_{gq} = 0 \tag{3.17}$$

$$i_{g\_dq} = i_{gd} + ji_{gq} = |\vec{i}_g|\left[cos\left(\theta_g - \beta_g\right) - j\,sin\left(\theta_g - \beta_g\right)\right] \tag{3.18}$$

The relationship between the converter dq-reference frame and the global synchronous reference frame is according to the transformation:

$$\begin{bmatrix} d \\ q \end{bmatrix} = \begin{bmatrix} cos\,\theta_g & sin\,\theta_g \\ -sin\,\theta_g & cos\,\theta_g \end{bmatrix} \begin{bmatrix} Re \\ Im \end{bmatrix}$$
$$d + jq = (Re + jIm)e^{-j\theta_g} \tag{3.19}$$

3.2.1.1. Phase Locked Loop (PLL)

As mentioned above, the PLL estimates the PCC voltage phase angle and grid frequency. When the converter control dq-frame rotates at synchronous speed with its d-axis perfectly aligned with the PCC voltage phasor ($\vec{v}_g$), then the PCC voltage will have only a d-axis component in the converter dq-frame and its q-axis component (v_{gq}) becomes zero. Thus, the PLL model, depicted in Figure 3-9, uses a PI controller to keep v_{gq} to zero. The model takes in as input PCC voltage from load flow calculations in the synchronous reference frame (Re-Im) and calculates v_{gq} according to (3.19):

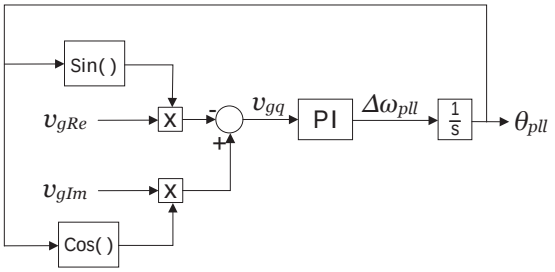

Figure 3-9 : PLL block diagram

where θ_{pll} is the estimated PCC voltage angle in radians, and $\Delta\omega_{pll}$ is the speed deviation of the converter control dq-frame from synchronous speed in rad/s. v_{gRe} and v_{gIm} are the

real and imaginary components of PCC voltage in the global synchronous reference frame, respectively. The first order differential equations of PLL model are:

$$\begin{aligned}\frac{d}{dt}\theta_{pll} &= k_{p,pll}\left(-v_{gRe}\sin\theta_{pll} + v_{gIm}\cos\theta_{pll}\right) + x_{pll}\\ \frac{d}{dt}x_{pll} &= k_{i,pll}\left(-v_{gRe}\sin\theta_{pll} + v_{gIm}\cos\theta_{pll}\right)\end{aligned} \tag{3.20}$$

where $k_{p,pll}$ and $k_{i,pll}$ are the proportional and integral constants of the PI controller respectively, while x_{pll} is a state variable associated with the integrator in the PI controller of the PLL. The grid frequency measured by the PLL and used in converter control is calculated as:

$$\omega_{pll} = \frac{\Delta\omega_{pll}}{\omega_0} + \omega_s \tag{3.21}$$

where ω_{pll} is measured grid frequency in p.u., ω_o is base grid frequency ($2\pi f$) in rad/s and ω_s is the speed of the reference machine (the speed of the global reference frame) in p.u..

3.2.1.2. VSC controllers

In average value model, voltage source v_s with controlled magnitude and phase represents the converter. The converter controller regulates active and reactive power flowing into the grid by controlling the current flowing through the series impedance, which in turn generates a reference for the magnitude and phase of v_s.

This section presents modelling of controllers for two-level and modular multi-level VSC converters. The controllers for the two types of VSC converters are the same, except for the additional energy and circulating current controllers in MMC. Therefore, the two-level converter control modelling is addressed first, and then the additional dynamics in MMC and its control is presented.

3.2.1.3. Two-level VSC controllers

Figure 3-10 shows a schematic of two-level converter dynamics and controller. A cascaded controller with inner and outer control loop is used for control of two-level VSC. The inner controller regulates ac grid current while the outer controller regulates active power/dc voltage and reactive power in the d and q axes, respectively.

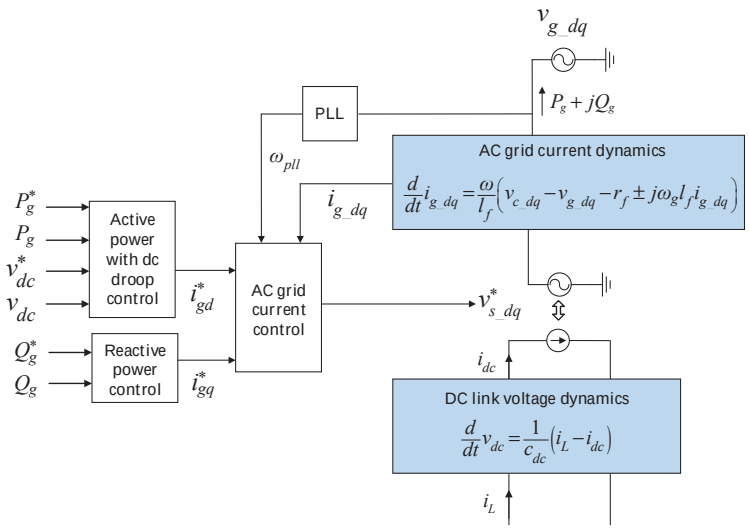

Figure 3-10 : Control structure for 2-level VSC converters

As shown in (3.16), active power and reactive power at the PCC are directly proportional to the d and q axis currents, respectively. Therefore, desired flow of active and reactive power can be realized by controlling the d- and q-axis currents independently. The outer controller uses PI controllers to remove the error between reference and measured signals, and generate ac grid d and q axis reference currents. DC voltage, active power or active power with dc voltage droop controller generates d-axis reference current, while reactive power or ac voltage controller generates the q-axis reference current. Figure 3-11 shows block diagrams of an outer loop active power with dc voltage droop and reactive power controllers.

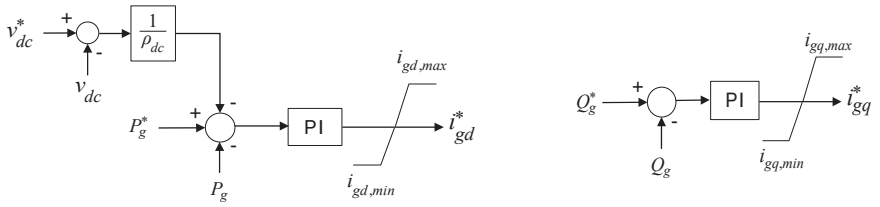

(a) (b)

Figure 3-11 : VSC outer controller (a) active power with dc voltage droop, and (b) reactive power

where the superscript * denotes reference signals, while v_{dc}, P_g and Q_g are dc voltage, active and reactive power, respectively. ρ_{dc} is the dc voltage droop constant. An infinite value of ρ_{dc} implies constant active power control, while a zero value of ρ_{dc} implies constant dc voltage control. Typical values of dc voltage droop constant in the literature are within 4-10%. The limiters determine whether active power or reactive power has priority. If ac voltage control is used to generate q-axis reference current, then the inputs in Figure 3-11(b) are replaced by $|v_g^*|$ and $|v_g|$, which are reference and measured PCC voltage magnitudes, respectively. Furthermore, if the converter provides ancillary services to the connected ac grid, then the outer loop of converter is modified accordingly. For example, Figure 3-12 shows how the outer d-axis controller is modified when the converter is involved in frequency or power oscillation control of the connected ac grid.

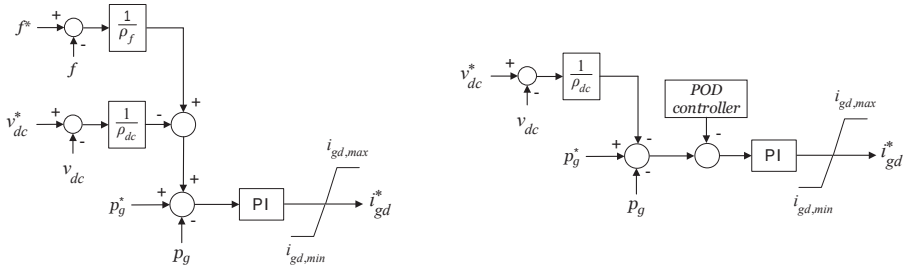

(a) (b)

Figure 3-12 : Converter outer d-axis controller with (a) frequency droop, and (b) power oscillation damping controllers

The governing equations for the outer controller with active power with dc voltage droop and reactive power control are:

$$\begin{aligned}
\frac{d}{dt}N_d &= k_{Pp}\left(P_g^* - P_g - \frac{1}{\rho_{dc}}\left(v_{dc}^* - v_{dc}\right)\right) \\
i_{gd}^* &= k_{Pi}\left(P_g^* - P_g - \frac{1}{\rho_{dc}}\left(v_{dc}^* - v_{dc}\right)\right) + N_d \\
\frac{d}{dt}N_q &= k_{Qp}\left(Q_g^* - Q_g\right) \\
i_{gq}^* &= k_{Qi}\left(Q_g^* - Q_g\right) + N_q
\end{aligned} \tag{3.22}$$

where k_{Pp} and k_{Pi} are proportional and integral gain constants of the PI in the active power controller with dc voltage droop, and k_{Qp} and k_{Qi} are proportional and integral gain constants of the PI in the reactive power controller, respectively. N_d and N_q are the states associated with the PI integrator in the active and reactive controllers, respectively.

A schematic for the inner current controller is presented in Figure 3-13. The inputs to the controller are reference currents generated by the outer loop controller and measured ac grid currents. A PI controller is used to remove the error between reference and measured currents. To remove the cross-coupling between d- and q-axis currents in the ac current dynamics in (3.12), a decoupling term, $\omega_g l_f i_{g\_dq}$, is introduced in the current controller.

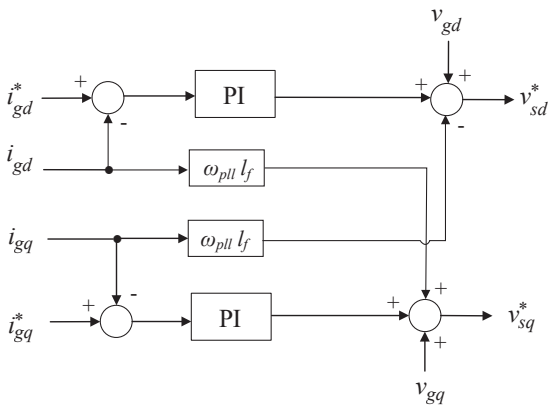

Figure 3-13 : Inner current controller

The DAE equations describing the inner controller are:

$$\begin{aligned}
\frac{d}{dt}M_d &= k_{ii}\left(i^*_{gd} - i_{gd}\right)\\
v^*_{sd} &= v_{gd} - \omega_g l_f i_{gq} + k_{ip}\left(i^*_{gd} - i_{gd}\right) + M_d\\
\frac{d}{dt}M_q &= k_{ii}\left(i^*_{gq} - i_{gq}\right)\\
v^*_{sq} &= v_{gq} + \omega_g l_f i_{gd} + k_{ip}\left(i^*_{gq} - i_{gq}\right) + M_q
\end{aligned} \tag{3.23}$$

where k_{ii} and k_{ip} are proportional and integral gains of the of the PI controllers, respectively. M_d and M_q are state variables associated with the PI in the d- and q-axes, respectively. The internal voltage of the VSC, v_s, is the same as the references passed through a low pass filter, which represents the switching time delay (T_{rconv}).

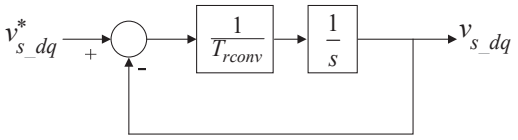

Figure 3-14 : Low pass filter representing a switching time delay

$$\frac{d}{dt}v_{s\_dq} = \frac{1}{T_{rconv}}\left(v^{*}_{s\_dq} - v_{s\_dq}\right) \tag{3.24}$$

3.2.1.4. MMC modelling and control

3.2.1.4.1. Basic operation principles

In this subsection, a brief overview of the basic principle of operation of an MMC converter is given before presenting modelling and control of MMC converters.

Figure 3-15 shows a schematic of a three-phase MMC converter. Each arm contains N number of series connected submodules (SM) and an arm inductor (L_a), which limits arm-current harmonics and fault currents. Two arms together form a leg, thereby $2N$ number of submodules are found in a leg. A three phase MMC has three legs and six arms. The number of submodules determines the number of steps in output voltage of an MMC.

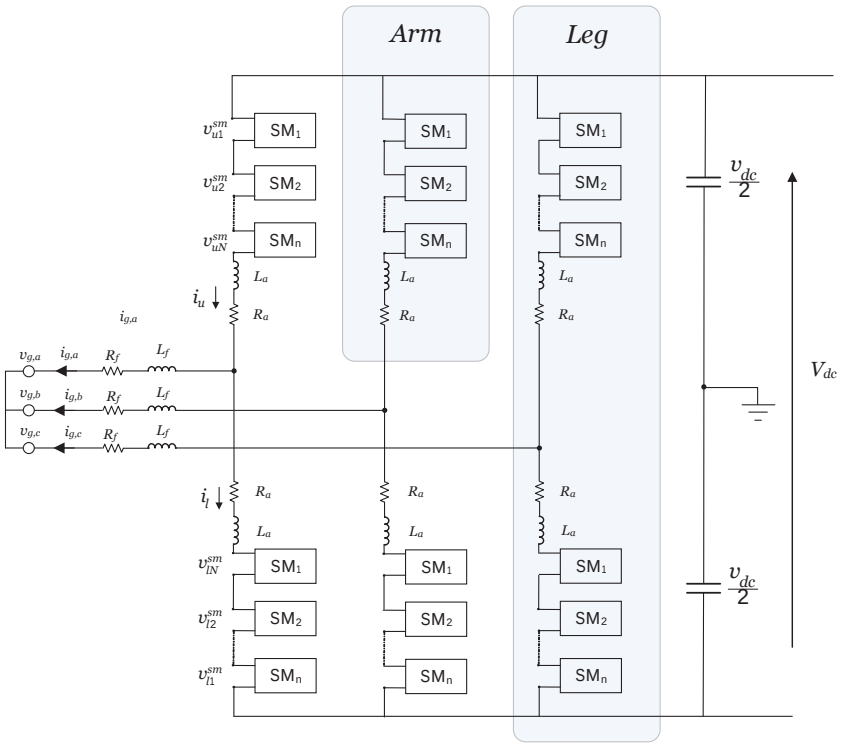

Figure 3-15: Typical MMC structure

In nearest level modulation, which is the most popular type of modulation for HVDC applications, N number of submodules are inserted in a leg at any time. An insertion index indicates how many submodules are inserted in an arm. In per unit, an insertion index of 1 indicates that all submodules are inserted and the arm voltage is at maximum value (v_{dc}). An insertion index of zero means no submodule is inserted and the arm voltage is zero. In case of submodule failure, the maximum voltage v_{dc} does not have any redundancy. However, all other voltage levels can be generated by inserting or bypassing different combinations of submodules.

When a submodule is inserted, the direction of current flow determines whether a capacitor is charged or discharged. If a submodule is bypassed or not inserted, then the capacitor charge remains constant. The voltages in each submodule capacitor need to be balanced. Therefore, a balancing algorithm tries to ensure equal voltage sharing among

the capacitors in each arm by dictating which combinations of submodules are inserted (out of the several possible combinations) at any instant. With high frequency balancing algorithm, it is possible to get an almost equal voltage in the capacitors in an arm. However, high frequency algorithm entails high switching losses. Thus, as a compromise between losses and perfect balancing of SM capacitor voltages, a balancing algorithm with lower frequency is used.

In addition to submodules capacitor voltage balancing control, the voltage balance between arms in a leg and circulating current need to be controlled.

3.2.1.4.2. Modeling of MMC

For a single submodule i shown in Figure 3-16, the voltage across its terminal is:

$$v_i^{sm} = n_i \cdot v_{c_i} \tag{3.25}$$

where v_i^{sm}, n_i and v_{c_i} are submodule voltage, insertion index and capacitor voltage, respectively.

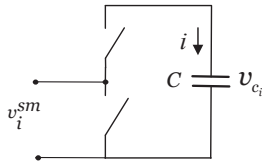

Figure 3-16 : A single submodule

If the submodule is inserted, n_i = 1, and if it is bypassed, n_i = 0. The voltage across the submodule capacitor (C) can then be calculated as:

$$C\frac{d}{dt}v_{c_i} = n_i \cdot i \tag{3.26}$$

Hereinafter, the subscript 'u' stands for the upper arm, while the subscript 'l' stands for the lower arm. In the following, the equations are derived for the upper arm. However, these equations are also valid for the lower arm.

Since the submodules are connected in series, the voltage across an arm is the summation of the voltage across each capacitor.

$$C\frac{d}{dt}v_{cu_1}+C\frac{d}{dt}v_{cu_2}+...+C\frac{d}{dt}v_{cu_N}=n_{u_1}\cdot i_u+n_{u_2}\cdot i_u+...+n_{u_N}\cdot i_u$$
$$C\frac{d}{dt}\sum_{i=1}^{N}v_{cu_i}=\sum_{i=1}^{N}n_{u_i}\cdot i_u \tag{3.27}$$

An insertion index for an arm, n_u, can be defined as the summation of the individual insertion indices as:

$$n_u=\frac{1}{N}\sum_{i=1}^{N}n_{u_i} \tag{3.28}$$

n_u ranges between 0 and 1. If n_u = 0, then all submodules in an arm are bypassed and if n_u = 1, then all the submodules in an arm are inserted. Substituting (3.28) into (3.27)

$$\left(\frac{C}{N}\right)\frac{d}{dt}v_{cu}^{\Sigma}=n_u\cdot i_u \tag{3.29}$$

where $v_{cu}^{\Sigma}=\sum_{i=1}^{N}v_{cu_i}$ is the total upper arm voltage.

Figure 3-17 shows a single leg of a three-phase MMC and is used to explain the current dynamics in MMC.

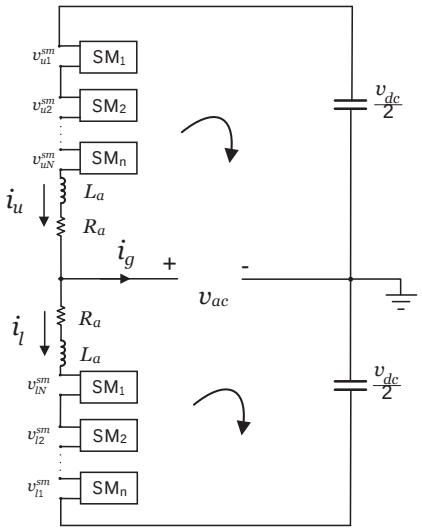

Figure 3-17 : MMC leg

According to Kirchhoff's law, the summation of voltage drops in the upper and lower arms should be zero. Following the direction of the arrow in the loop and the current flow directions, the voltage equations become:

$$\begin{aligned} -\frac{v_{dc}}{2} + \sum_{i=1}^{N} (n_{u_i} \cdot v_{cu_i}) + R_a i_u + L_a \frac{d}{dt} i_u + v_{ac} = 0 \\ -\frac{v_{dc}}{2} + \sum_{i=1}^{N} (n_{l_i} \cdot v_{cl_i}) + R_a i_l + L_a \frac{d}{dt} i_l - v_{ac} = 0 \end{aligned} \tag{3.30}$$

Assuming that all SM capacitors in the same arm have identical voltage, the individual submodule voltage becomes:

$$v_{c_i} = \frac{v_{cu}^{\Sigma}}{N} \tag{3.31}$$

Substituting (3.31) for both upper and lower SM voltages in (3.30), the equation simplifies as:

$$
\begin{aligned}
-\frac{v_{dc}}{2} + n_u \cdot v_{cu}^{\Sigma} + R_a i_u + L_a \frac{d}{dt} i_u + v_{ac} = 0 \\
-\frac{v_{dc}}{2} + n_l \cdot v_{cl}^{\Sigma} + R_a i_l + L_a \frac{d}{dt} i_l - v_{ac} = 0
\end{aligned}
\tag{3.32}
$$

where n_u and n_l are upper and lower arm insertion indices as defined in (3.28).

Under the assumption of ideal SM capacitor voltage balancing, an average model of one of the legs is represented by four dynamic equations (two for the upper arm and two for the lower arm):

$$
\left(\frac{C}{N}\right)\frac{d}{dt} v_{cu}^{\Sigma} = n_u \cdot i_u \tag{3.33}
$$

$$
\left(\frac{C}{N}\right)\frac{d}{dt} v_{cl}^{\Sigma} = n_l \cdot i_u \tag{3.34}
$$

$$
L_a \frac{d}{dt} i_u = -R_a i_u + \frac{v_{dc}}{2} - n_u \cdot v_{cu}^{\Sigma} - v_{ac} \tag{3.35}
$$

$$
L_a \frac{d}{dt} i_l = -R_a i_l + \frac{v_{dc}}{2} - n_l \cdot v_{cl}^{\Sigma} + v_{ac} \tag{3.36}
$$

Subtracting (3.36) from (3.35) gives the grid current dynamics as:

$$
\begin{aligned}
L_a \frac{d}{dt}\left(i_u - i_l\right) &= -R_a\left(i_u - i_l\right) + \left(-n_u \cdot v_{cu}^{\Sigma} + n_l \cdot v_{cl}^{\Sigma}\right) - 2v_{ac} \\
\frac{1}{2} L_a \frac{d}{dt} i_g &= -\frac{R_a}{2} i_g + \frac{\left(-n_u \cdot v_{cu}^{\Sigma} + n_l \cdot v_{cl}^{\Sigma}\right)}{2} - v_{ac}
\end{aligned}
\tag{3.37}
$$

where i_g is the grid current flowing from the converter to the ac grid.

$$
i_g = i_u - i_l \tag{3.38}
$$

Adding (3.35) and (3.36) gives the circulating current dynamics as:

$$
\begin{aligned}
L_a \frac{d}{dt}\left(i_u + i_l\right) &= -R_a\left(i_u + i_l\right) + v_{dc} - \left(n_u \cdot v_{cu}^{\Sigma} + n_l \cdot v_{cl}^{\Sigma}\right) \\
L_a \frac{d}{dt} i_c &= -R_a i_c + \frac{v_{dc}}{2} - \frac{\left(n_u \cdot v_{cu}^{\Sigma} + n_l \cdot v_{cl}^{\Sigma}\right)}{2}
\end{aligned}
\tag{3.39}
$$

where i_c is the circulating current flowing between different legs.

$$
i_c = \frac{i_u + i_l}{2} \tag{3.40}
$$

From (3.37) and (3.39), it can be seen that the grid current depends on the difference between the arm voltages, which is equivalent to the internal voltage of the converter (v_s), while the circulating current depends on the sum of the arm voltages, known as the common mode voltage (v_c).

$$
\begin{aligned}
v_s &= \frac{\left(-n_u \cdot v_{cu}^{\Sigma} + n_l \cdot v_{cl}^{\Sigma}\right)}{2} \\
v_c &= \frac{\left(n_u \cdot v_{cu}^{\Sigma} + n_l \cdot v_{cl}^{\Sigma}\right)}{2}
\end{aligned}
\tag{3.41}
$$

Solving upper (i_u) and lower (i_l) arm currents from (3.38) and (3.40), and substituting the expressions into (3.33) and (3.34) gives arm voltage dynamic equations as:

$$
\begin{aligned}
\left(\frac{C}{N}\right)\frac{d}{dt} v_{cu}^{\Sigma} &= n_u \cdot \left(i_c + \frac{i_g}{2}\right) \\
\left(\frac{C}{N}\right)\frac{d}{dt} v_{cl}^{\Sigma} &= n_l \cdot \left(i_c - \frac{i_g}{2}\right)
\end{aligned}
\tag{3.42}
$$

Then, the energy dynamics in the upper and lower arms can be calculated as:

$$
\begin{aligned}
\frac{d}{dt} w_{cu}^{\Sigma} &= \frac{d}{dt}\left(\frac{1}{2} \cdot \frac{C}{N} \cdot v_{cu}^{\Sigma}\right) \\
&= v_{cu}^{\Sigma}\left(\frac{C}{N}\right)\frac{d}{dt} v_{cu}^{\Sigma} = n_u \cdot v_{cu}^{\Sigma} \cdot \left(i_c + \frac{i_g}{2}\right)
\end{aligned}
\tag{3.43}
$$

$$\begin{aligned}\frac{d}{dt}w_{cl}^{\Sigma} &= \frac{d}{dt}\left(\frac{1}{2}\cdot\frac{C}{N}\cdot v_{cl}^{\Sigma}\right)\\ &= v_{cl}^{\Sigma}\left(\frac{C}{N}\right)\frac{d}{dt}v_{cl}^{\Sigma} = n_l\cdot v_{cl}^{\Sigma}\cdot\left(i_c-\frac{i_g}{2}\right)\end{aligned} \tag{3.44}$$

Adding and subtracting equations (3.43) and (3.44) gives the energy sum (w_{Σ}) and energy difference (w_{Δ}) equations:

$$\begin{aligned}&\frac{d}{dt}\left(w_{cu}^{\Sigma}+w_{cl}^{\Sigma}\right) = 2\left(\frac{n_u v_{cu}^{\Sigma}+n_l v_{cl}^{\Sigma}}{2}\right)\cdot i_c-\left(\frac{-n_u v_{cu}^{\Sigma}+n_l v_{cl}^{\Sigma}}{2}\right)\cdot i_g\\ &\frac{d}{dt}w_{\Sigma} = 2\cdot v_c\cdot i_c - v_s\cdot i_g\end{aligned} \tag{3.45}$$

$$\begin{aligned}&\frac{d}{dt}\left(w_{cu}^{\Sigma}-w_{cl}^{\Sigma}\right) = 2\left(\frac{n_u v_{cu}^{\Sigma}-n_l v_{cl}^{\Sigma}}{2}\right)\cdot i_c+\left(\frac{n_u v_{cu}^{\Sigma}+n_l v_{cl}^{\Sigma}}{2}\right)\cdot i_g\\ &\frac{d}{dt}w_{\Delta} = -2\cdot v_s\cdot i_c + v_c\cdot i_g\end{aligned} \tag{3.46}$$

To summarize, the four dynamic equations representing the MMC physical system are:

$$\begin{aligned}&\frac{1}{2}L_a\frac{d}{dt}i_g = -\frac{R_a}{2}i_g + v_s - v_{ac}\\ &L_a\frac{d}{dt}i_c = -R_a i_c + \frac{v_{dc}}{2} - v_c\\ &\frac{d}{dt}w_{\Sigma} = 2\cdot v_c\cdot i_c - v_s\cdot i_g\\ &\frac{d}{dt}w_{\Delta} = -2\cdot v_s\cdot i_c + v_c\cdot i_g\end{aligned} \tag{3.47}$$

The equations in (3.47) are for each leg or phase of the converter. The single-phase nature of the converter topology leads to double frequency oscillations in the power flow, which results in oscillations in the capacitor voltage of each arm in steady state [79]. This means simplifications need to be made to develop a model where the steady state variables remain constant in steady state and can be used in small-signal stability studies. Developing MMC models that are suitable for integrated study large ac/dc power system and small-signal studies is at a nascent stage. References [14, 79, 80] propose small-signal

models for MMC and this is a topic that is continuously being updated. As of now, there is no single model that is widely accepted and can be used as a standard. In this thesis, a model proposed in [79] is used.

The simplified state-space modeling approach of [79], which is derived from the average model described in [81] and [82], is dependent on the assumption of Compensated Modulation (CM). This implies that the control system includes an online compensation for the variations in the sum of the arm capacitor voltages when calculating the insertion indexes. More precisely, the upper and lower arm insertion indexes of the converter n_u and n_l for each phase k are calculated by dividing the output of the ac-grid and internal circulating current controllers v_s* and v_c* by the aggregated voltage, v_{cu}^{Σ} or v_{cl}^{Σ}, in the corresponding arm as indicated by Equation (3.48).

$$n_{u,k} = \frac{-v_{s,k}^{*} + v_{c,k}^{*}}{v_{cu,k}^{\Sigma}}, \quad n_{l,k} = \frac{v_{s,k}^{*} + v_{c,k}^{*}}{v_{cl,k}^{\Sigma}}; \quad for \quad k \in \{a,b,c\} \tag{3.48}$$

If this assumption is used, the voltages driving the ac-side currents v_s and voltage driving the circulating currents v_c become approximately equal to the output of their respective controllers, as indicated by (3.49).

$$\begin{aligned} v_{s,abc} = v_{s,abc}^{*} \rightarrow v_{s,dq} = v_{s,dq}^{*} \\ v_{c,abc} = v_{c,abc}^{*} \rightarrow v_{c,dqz} = v_{c,dqz}^{*} \end{aligned} \tag{3.49}$$

An additional effect of the CM assumption is the introduction of a significant degree of decoupling between the zero-sequence dynamics of the energy-sum $w_{\Sigma,z}$ from the individual energy difference oscillations w_{Δ}. Furthermore, it is possible to neglect the effect of the dq-components of v_c^{*} in the energy-sum zero-sequence dynamics, as they are significantly smaller than the zero-sequence component v_{cz} [79]. From these assumptions, a simplified representation of the MMC can be obtained by modelling only the zero-sequence dynamics of the energy-sum $w_{\Sigma z}$, and the circulating current i_{cz}, which are inherently time-invariant in steady state, and therefore suited for linearization and eigenvalue-based stability analysis.

Thus, the energy difference and the other frequency components of the circulating current can be neglected while still obtaining a model that is accurately representing an MMC, as seen from its ac- and dc-terminals. The MMC simplified zero-sequence model in p.u. is:

$$\begin{aligned}\frac{d}{dt}w_{\Sigma z} &\approx \left[-\tfrac{1}{2}\left(v_{sd}^{*}i_{vd}+v_{sq}^{*}i_{vq}\right)+2v_{cz}^{*}i_{cz}\right]\frac{\omega}{4c_{eq}}\\ \frac{d}{dt}i_{cz} &= -\frac{\omega}{l_a}\left(r_a i_{cz}-v_{cz}^{*}+v_{dc}\right)\end{aligned} \tag{3.50}$$

where c_{eq} is the total equivalent capacitance per arm of the MMC (i.e. C/N), r_a and l_a are the arm resistance and inductance represented in the ac-side p.u. system. All voltage and current variables in (3.50) are represented in the ac-side per unit system except v_{dc}, which is represented in the dc-side per unit system. Finally, $w_{\Sigma Z}$ is represented in the per unit system by means of the MMC energy base, defined as $W_b = \left(\frac{C}{N}\right) * V_{dc,b}^2$ [79].

To summarize, the physical system of the MMC is modelled for small-signal studies by the grid current, zero sequence energy and circulating current dynamics as:

$$\begin{aligned}\frac{d}{dt}i_g &= \frac{\omega}{l_v}\left(-r_v i_g+v_s-v_g\right)\\ \frac{d}{dt}w_{\Sigma z} &\approx \left[-\tfrac{1}{2}\left(v_{sd}^{*}i_{vd}+v_{sq}^{*}i_{vq}\right)+2v_{cz}^{*}i_{cz}\right]\frac{\omega_b}{4c_{eq}}\\ \frac{d}{dt}i_{cz} &= -\frac{\omega_b}{l_a}\left(r_a i_{cz}-v_{cz}^{*}+v_{dc}\right)\end{aligned} \tag{3.51}$$

where r_v is the sum of half of the arm resistance and filter resistance ($r_v = \frac{r_a}{2} + r_f$), l_v is the sum of half of the arm inductance and filter inductance ($l_v = \frac{l_a}{2} + l_f$), ω is base grid frequency, and v_g is the PCC voltage v_g. Both the grid current and the zero sequence circulating current can be controlled independently. The grid current i_g is controlled to regulate active and reactive power at PCC, similar to two-level VSC, while the circulating current $i_{c,z}$ is controlled to regulate the zero sequence energy sum dynamics.

The dc voltage dynamics of the cable capacitance connected in between the dc terminals of the MMC is given by (3.52), where c_{dc} is the border capacitance of the cable model that will be discussed in section 3.2.2. Furthermore, i_L is the cable current flowing into the converter. Finally, the zero-sequence of the circulating current is being multiplied by 4 instead of 3 since it is referred to the ac-side per unit system.

$$\frac{d}{dt}v_{dc} = \frac{\omega_b}{c_{dc}}\left(i_L - 4i_{c,z}\right) \tag{3.52}$$

3.2.1.4.3. MMC controllers

Figure 3-18 shows a schematic of an MMC converter dynamics and controller. Similar to two-level converter control, cascaded outer and inner loop controllers are used. Active and reactive power outer controllers generate grid current references, while the zero-sequence energy sum controller generates zero-sequence circulating current reference.

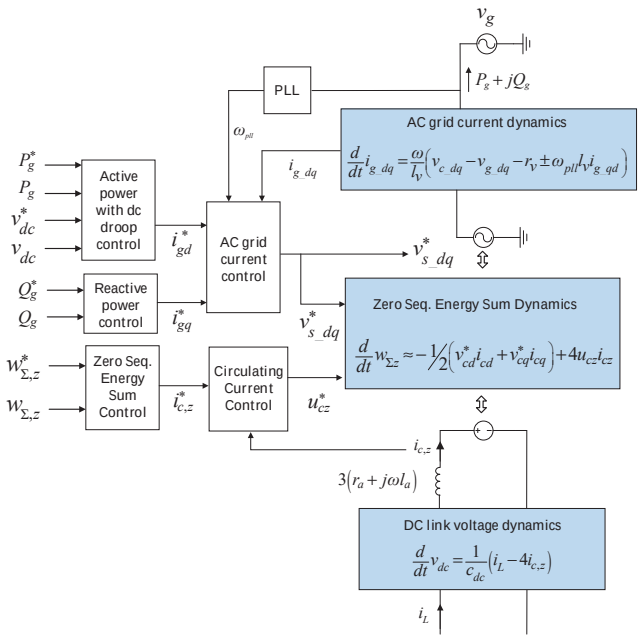

Figure 3-18 : Overview of configuration and control system for a single-terminal MMC

The outer active and reactive power controllers of an MMC converter are the same as the outer controllers for a two-level VSC converter shown in Figure 3-11. Therefore, the controllers' governing equation (3.22) remains the same for an MMC converter. Furthermore, the ac grid current controller for the MMC is the same as the 2-level current controller in Figure 3-13 and (3.23) with the r_f and l_f replaced by r_v and l_v.

$$r_v = \frac{r_a}{2} + r_f; \quad l_v = \frac{l_a}{2} + l_f \tag{3.53}$$

The zero-sequence energy sum $w_{\Sigma z}$ controller uses PI controller as defined in (3.54) and provides current reference for an inner loop i_{cz} controller.

$$\begin{aligned} i_{cz}^{*} &= k_{p\Sigma}\left(w_{\Sigma}^{*} - w_{\Sigma}\right) + k_{i\Sigma}\kappa \\ \dot{\kappa} &= w_{\Sigma}^{*} - w_{\Sigma} \end{aligned} \tag{3.54}$$

In turn, the inner control loop regulates i_{cz} to its reference by providing the reference value v_{cz}*, as given in (3.55).

$$\begin{aligned} u_{cz}^{*} &= -k_{pc}\left(i_{cz}^{*} - i_{cz}\right) - k_{ic}\xi \\ \dot{\xi} &= i_{cz}^{*} - i_{cz} \end{aligned} \tag{3.55}$$

In (3.54)-(3.55) with $k_{p\Sigma}$, k_{pc}, $k_{i\Sigma}$ and k_{ic} are the proportional and integral gain coefficients of the PI controllers, whereas κ and ξ are the states created by the integral part of the PI regulator.

3.2.2. DC cables

DC cable parameters are uniformly distributed along the line. Approximate models use lumped parameters and model a dc cable with series resistance, series inductance, shunt capacitance and shunt conductance. In the thesis, two cable models are used that have different levels of accuracy. The first cable model, which is used in most of the studies, is a single π-model with lumped resistance and shut capacitances as shown in Figure 3-19.

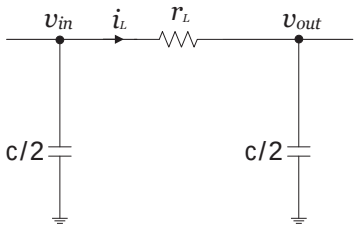

Figure 3-19 : A single π-section cable model

The shunt capacitances are added to the converter dc-link capacitance and their dynamics is considered in converter dc-link modeling in (3.15) and (3.52). The algebraic equation for the current flowing in each cable j is calculated according to (3.56). If more than one cable are connected to a terminal converter, then the current flowing into the converter, i_L, would be the sum of the currents flowing in all connected cables.

$$i_{L\_j} = \frac{v_{in\_j} - v_{out\_j}}{r_{L\_j}} \tag{3.56}$$

The second cable model is a cascaded π-section model with multiple parallel resistance and inductance (RL) branches, as shown in Figure 3-20. The model is first proposed in [83] and considers the frequency dependency of the dc cable's series resistance r and inductance l per unit length. The accuracy of the model increases as the number of parallel branches and π-sections increases. However, the complexity of the model also increases.

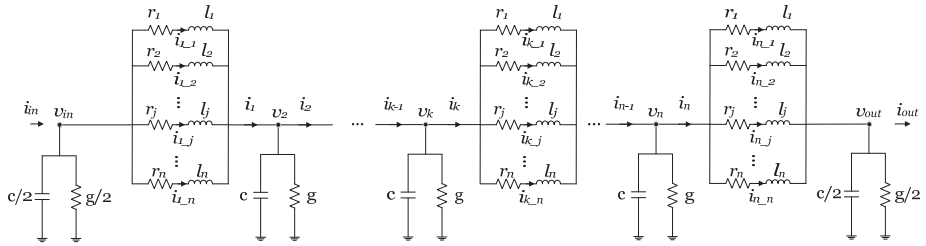

Figure 3-20 : Multiple π-section with multiple parallel branches cable model

The voltage and current dynamics can be written in terms of first-order differential equations, which makes it easy to straightforwardly use the model for the small-signal studies. The current in the series element of each π-section is split amongst different parallel branches, each with its own RL dynamics. This allows to account for the frequency-dependence of the series impedance. Following Kirchhoff's current law, the current in the series element is equal to the sum of the currents in the parallel branches. The current flowing in the j^{th} parallel branch of the k^{th} π-section has dynamics governed according to:

$$\frac{d}{dt} i_{k\_j} = \frac{1}{l_j}\left(v_k - v_{k+1} - r_j i_{k\_j}\right) \tag{3.57}$$

Similar to the lumped cable model, the shunt capacitances, thus the voltage dynamics, at the beginning and end of the cable are considered in the converter dc-link dynamics, whereas the voltage dynamics in the middle of the cable (v_2, v_3,..., v_k,..., v_n) are governed by the following first-order differential equation.

$$\frac{d}{dt}v_k = \frac{1}{c}\left(i_{k-1} - i_k - g v_k\right) \tag{3.58}$$

Both types of dc cable models have been used for different analyses in the thesis.

3.3. Complete Hybrid AC/DC Power System

The previous sections presented differential and algebraic equations that are used to model generators, excitation systems, governors/turbines, cables, PLL, converters and their controllers. These components are the main building blocks of a hybrid ac/dc power system model in stability studies. This section explains how the individual component models are interconnected to form a complete hybrid ac/dc power system model.

3.3.1. Reference frame transformation

The synchronous generators and converter control system models use different types of synchronously rotating dq reference frames. On the one hand, the rotating dq reference frame used for synchronous generator modelling has its d-axis aligned with the magnetic axis of the rotor field windings and leads the q-axis by 90 electrical degrees. On the other hand, the rotating dq reference frame used for converter control modelling has its d-axis aligned with the PCC voltage vector and lags the q-axis by 90 electrical degrees. A common global reference frame is necessary to connect the various components modelled in their own dq frames and to solve the algebraic load flow equations. This global reference frame can be set arbitrarily, but it is usually the dq rotor axis of one of the machines in the ac system, which is referred to as a reference machine. Figure 3-21 shows rotating dq reference frames for converter control and synchronous generator modelling together with their rotational shift compared to the global reference frame.

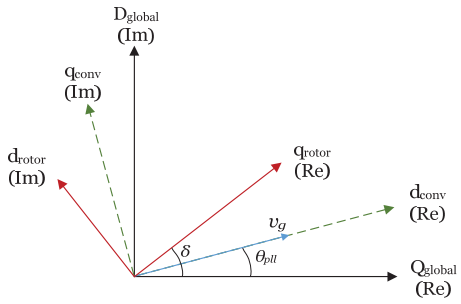

Figure 3-21: Rotating reference frames

The transformation from global dq reference frame to individual generator's dq-axis is according to:

$$\begin{bmatrix} q_{rotor} \\ d_{rotor} \end{bmatrix} = \begin{bmatrix} \cos\delta & \sin\delta \\ -\sin\delta & \cos\delta \end{bmatrix} \begin{bmatrix} Q_{global} \\ D_{global} \end{bmatrix}$$
$$q_{rotor} + jd_{rotor} = \left(Q_{global} + jD_{global}\right)e^{-j\delta} \tag{3.59}$$

The transformation from global dq reference frame to converter control dq-frame is according to:

$$\begin{bmatrix} d_{conv} \\ q_{conv} \end{bmatrix} = \begin{bmatrix} \cos\theta_{pll} & \sin\theta_{pll} \\ -\sin\theta_{pll} & \cos\theta_{pll} \end{bmatrix} \begin{bmatrix} Q_{global} \\ D_{global} \end{bmatrix}$$
$$d_{conv} + jq_{conv} = \left(Q_{global} + jD_{global}\right)e^{-j\theta_{pll}} \tag{3.60}$$

Note that q axis is aligned with the real axis in the rotor dq frame, while d is aligned with the real axis in converter dq frame.

3.3.2. AC Transmission Network Equations

Generators and converters are modelled as voltage sources behind appropriate impedances. In the network equations, generators and converters are represented by a Norton equivalent current source in parallel with their respective impedances. Figure 3-22 and (3.61) present the equivalent circuit and corresponding equation for the generators and converters representation in network equations.

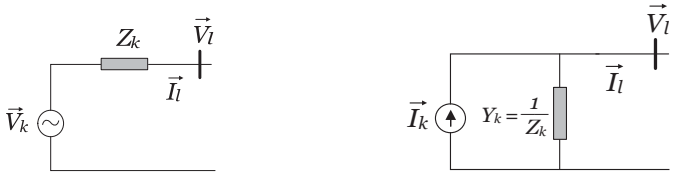

(a) (b)

Figure 3-22 : Equivalent circuit for generators and converters in network modelling

$$I_k = \frac{V_k}{Z_k} = \frac{V_l}{Z_k} + I_l \tag{3.61}$$

For a 6th order model of the synchronous generator, (3.1), V_k is subtransient voltage (E''), V_l is generator terminal voltages (V_t) and Z_k is $r_a + jx_d''$, where r_a is stator (armature) resistance. As for the VSC converters, V_k is the converter voltage driving the ac grid current (v_s), V_l is PCC voltage (v_g) and Z_k depends on the converter type. For two-level converters, Z_k is the filter impedance $r_f + j\omega_g l_f$, while for the MMC converters model, Z_k is MMC filter impedance plus half of the MMC arm inductance $r_v + j\omega_g l_v$.

In the ac load flow calculations, converters and synchronous generators are considered as current sources behind admittances as shown in Figure 3-22(b). These admittances are augmented to the ac grid admittance matrix $\mathbf{Y}_{ac}$ at the buses where the converters or the generators are connected.

$$\mathbf{Y}_{aug} = \mathbf{Y}_{ac} + \mathbf{Y}_{gen} + \mathbf{Y}_{conv} \tag{3.62}$$

Then, the overall ac network equation is:

$$\vec{\mathbf{I}} = \mathbf{Y}_{Aug}\vec{\mathbf{V}} \tag{3.63}$$

where $\mathbf{I}$ and $\mathbf{V}$ are current injection and bus voltage vectors in the global reference frame. $\mathbf{I}$ has non-zero elements at generator and converter buses, while it has zero elements at load buses because loads are modelled as constant impedances. Once bus voltages are computed, generator and terminal converter currents (depicted as I_l in Figure 3-22) are calculated according to (3.64). The current is expressed in the global reference frame and

need to be transformed into relevant local reference frames before being inserted into the generator and converter dynamic equations.

$$I_l = \frac{V_k - V_l}{Z_k} \tag{3.64}$$

The dc grid load flow uses dc grid admittance matrix $\mathbf{Y}_{dc}$ in (3.63), and $\mathbf{I}$ is a vector of dc currents injected into dc grid at the terminals, while $\mathbf{V}$ is a vector of dc bus voltages. In this thesis, an open source MATLAB based ac/dc power flow analysis tool, called MATACDC [84], is used for load flow calculations. The tool solves the ac/dc power flow problem sequentially, meaning that it solves the ac/dc power flow by iterating between the ac systems and the dc systems [85, 86].

3.3.3. Interfacing the different DAE

The different ac and dc components and their controllers modelled using DAE equations in the previous sections are connected with each other to form a hybrid ac/dc power system. Figure 3-23 shows interconnection of ac network, generators, governor/turbine, excitation system, PLL, converter and cable modelling equations. In addition, the blocks in the figure represent the equation numbers of components. Note that the figure shows a single ac grid with a converter and a dc cable. Other ac grids connected to a hybrid ac/dc system will have similar arrangement and a connection is formed through the dc cable model.

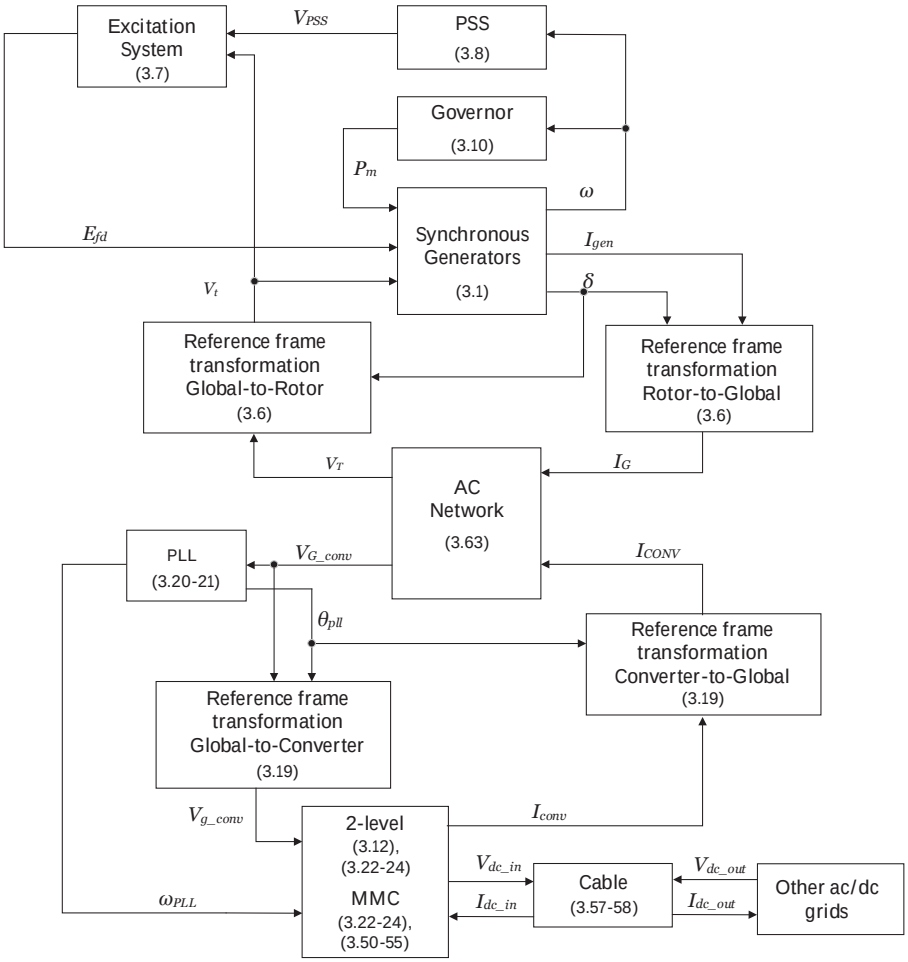

Figure 3-23 : Complete dynamic model for the test grid

3.3.4. Linear and Non-Linear Model Simulation

A two-area power system with eleven buses and four generators from [72] is used to validate the linear and non-linear ac grid model developed in MATLAB/Simulink. The initial power flow for the system is presented in Table 3-1.

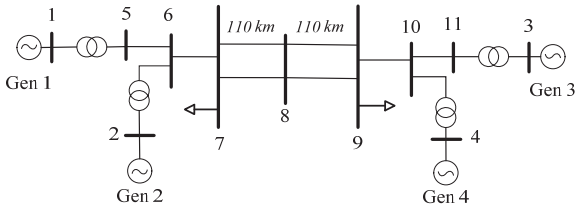

Figure 3-24 : A two-area system

Table 3-1 : Initial power flow

	P [MW]	Q [MVAr]	V_t [p.u.]
Gen 1	700	185	1.03 ∠ 20.2°
Gen 2	700	235	1.01 ∠ 10.5°
Gen 3	719	176	1.03 ∠ -6.8°
Gen 4	700	202	1.01 ∠ -17.0°

Generator and network data are taken from [72]. Gen 1 is fitted with SEXS type of excitation system model and TGOV1 type of turbine/governor model. An identical grid was developed in the power system simulation tool DIgSILENT *PowerFactory* [87] and was used to validate the SMATLAB model. DIgSILENT *PowerFactory* uses a generator model based on rotor winding flux linkage dynamics and inductances estimated from open-loop transient and sub-transient time constants. On the other hand, the MATLAB model uses a generator model that is based on induced voltages due to rotor flux linkages and open-loop transient and sub-transient time constants. Therefore, due to the small difference in modelling, perfect matching between the simulation tools is not expected. However, the dynamics captured by the two tools is expected to be similar.

Figure 3-25 shows eigenvalues from the linear analysis of the test system in an s-plane. The cross (x) marks indicate eigenvalues computed from the MATLAB model, while the circle (o) marks indicate eigenvalues computed from the *PowerFactory* model. The oscillatory modes with frequencies in the range 2-8 rad/s are electromechanical modes while the oscillatory modes with frequencies in the range 0-2 rad/s are exciter and governor modes. It can be seen from the figure that the positions of the eigenvalues in the complex plane for the two simulation tools is close to each other.

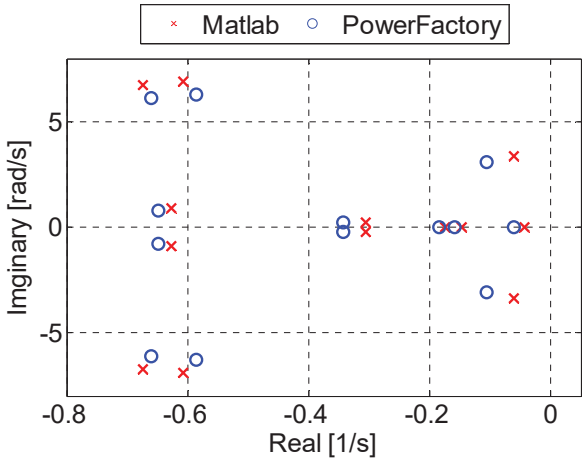

Figure 3-25 : Modes with real part greater than -1

A step change in load was used to validate in time domain the non-linear model developed in MATLAB. A 40 MW step increment of the load connected to bus 9 at t=20s was simulated in the two simulation tools. Power outputs and speeds of the generators in the system are presented in Figure 3-26 and Figure 3-27, respectively. As mentioned earlier, only Gen 1 has a turbine/governor system. Therefore, the change in load demand in the system is met by increasing the output of Gen 1 following the governor's droop characteristics. The other generators' power output is disturbed following the transient disturbance but return to the initial operating point. Frequency in the system is lowered from 1 p.u. due to the increment in load demand in the system and the new operating point on the generator droop characteristics.

From the speed curves, it can be seen that Gen 3 and Gen 4 exhibit an oscillatory response right after the disturbance. The small difference in the initial load flow values is translated into a minor difference in the steady state values both before and after the disturbance. The response in MATLAB has lower damping than the response in *PowerFactory*. This was also seen in the position of the eigenvalues for the two tools in Figure 3-25, where the electromechanical modes of the MATLAB model are located to the right of the *PowerFactory* modes. In general, there is a good correspondence between the non-linear models developed in MATLAB and *PowerFactory*.

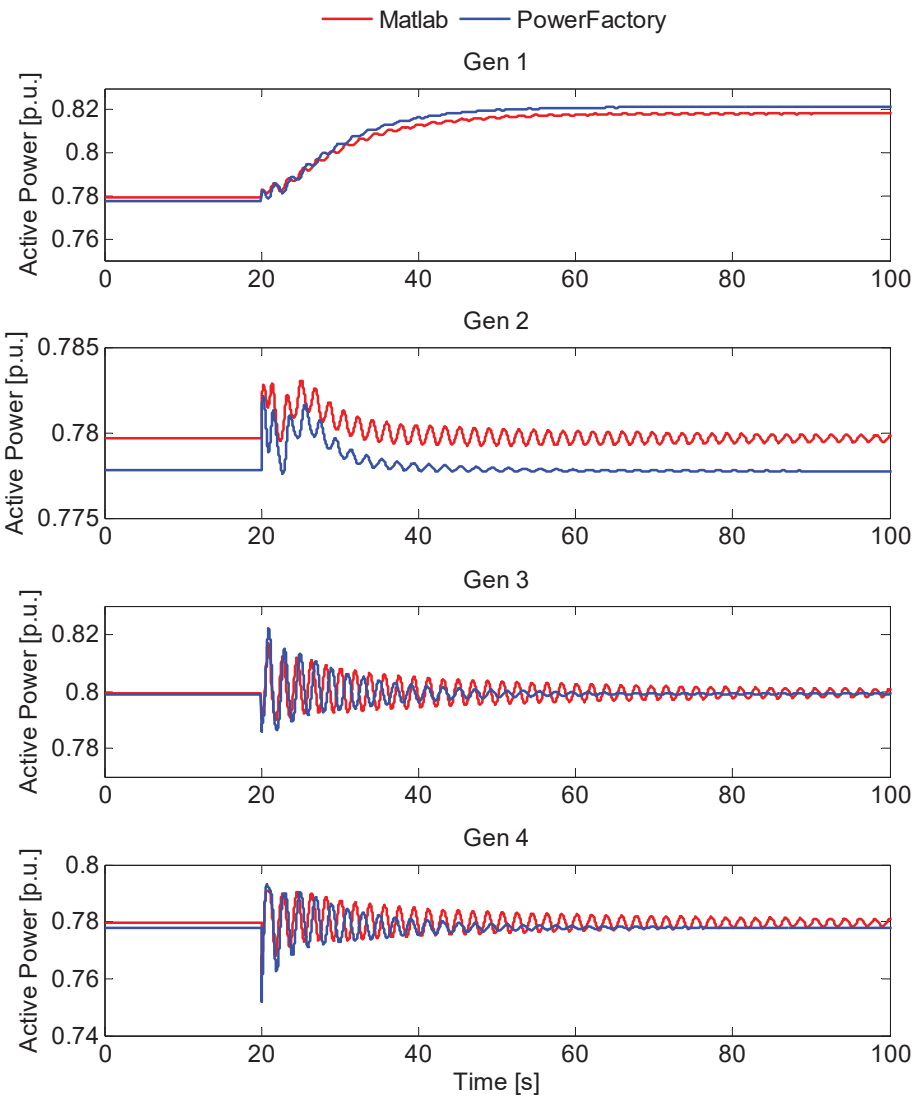

Figure 3-26 : Generators power output

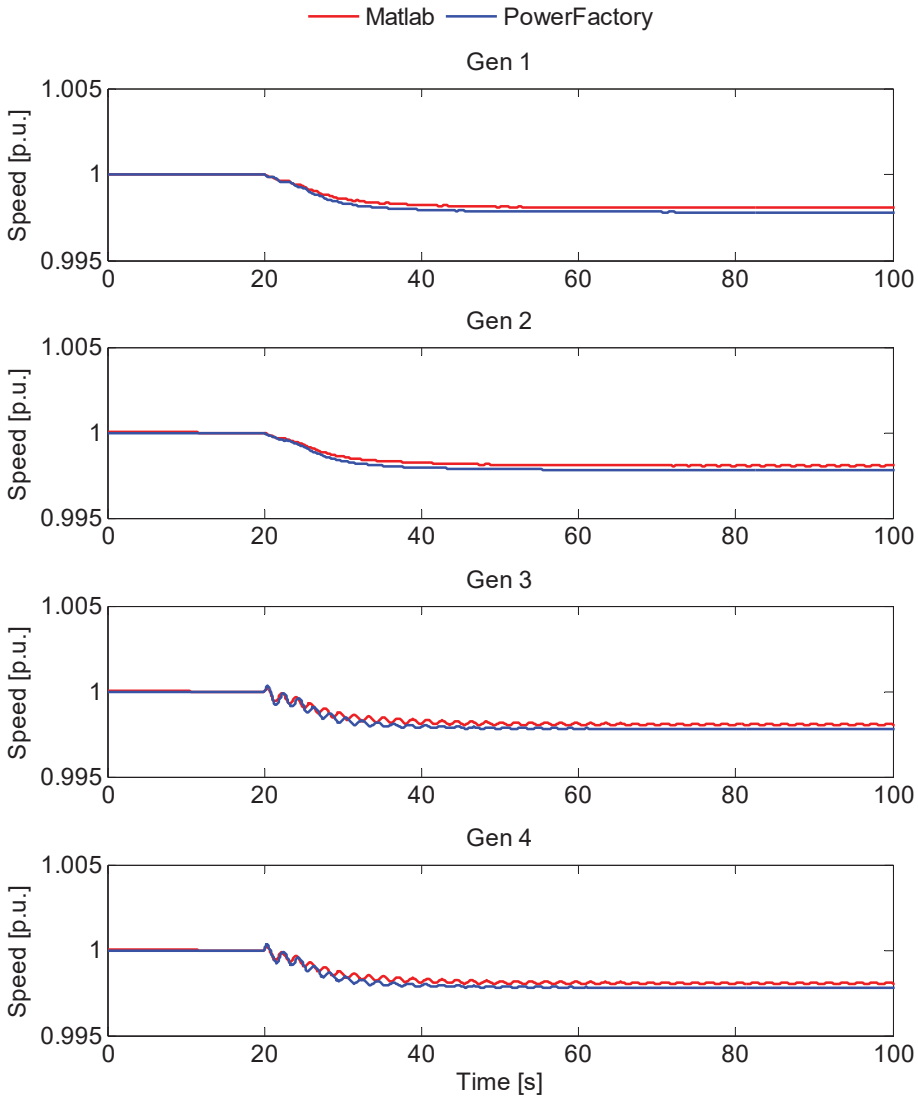

Figure 3-27 : Generator speeds

The performance of a non-linear hybrid ac/dc grid model developed in MATLAB/Simulink was tested using the two ac grid power systems connected by an HVDC link shown in Figure 3-28. Grid A the two-area model used earlier while, Grid B is a 9 bus system with three-generator and three loads from [71]. All machines in the test system are synchronous generators with automatic voltage regulators and governor controllers.

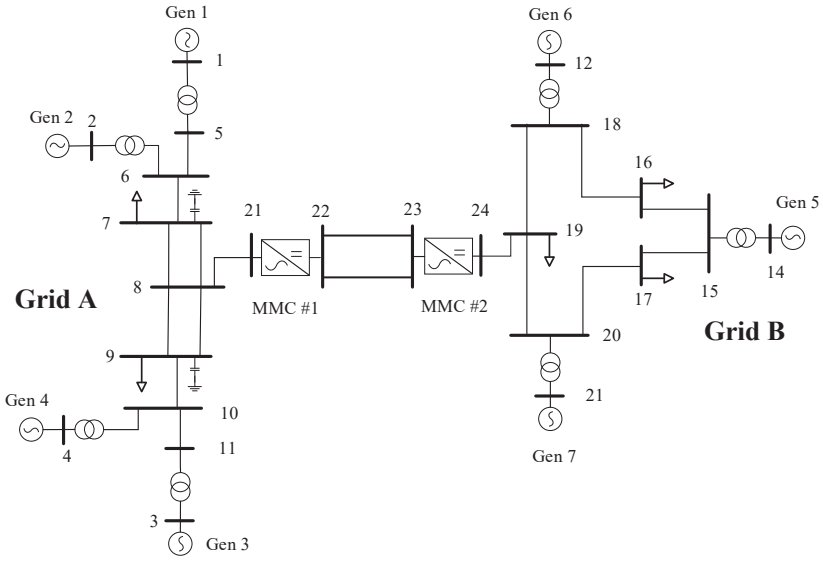

Figure 3-28 : Test hybrid ac/dc power system

MMC#1 is operating in dc voltage control, setting the dc link voltage equal to 1 pu, while MMC#2 is operating in power control mode importing 0.2 pu active power into Grid B. The reactive power reference for both converters is set to zero. At t=200s, the reference power was changed by 0.2 pu, meaning more power starts to flow into Grid B. This leads to an active power imbalance in both grids causing frequency disturbances shown in Figure 3-29.

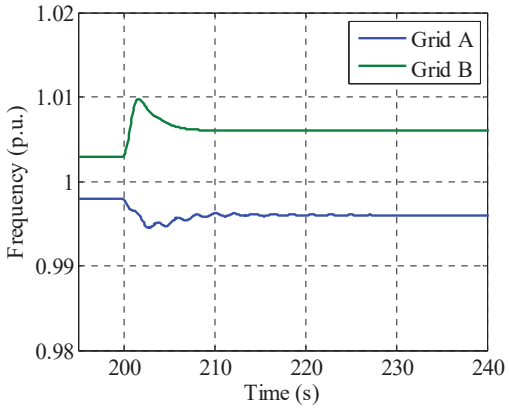

Figure 3-29 : Frequencies in Grid A and B after step change in power reference of MMC#2

The frequency in Grid A drops as there is more load demand in the system (due to the increased power demand through the HVDC from Grid B) than generation, and vice-versa for Grid B. The governors in both grids regulate the system frequency by changing generator power output according to their droop setting.

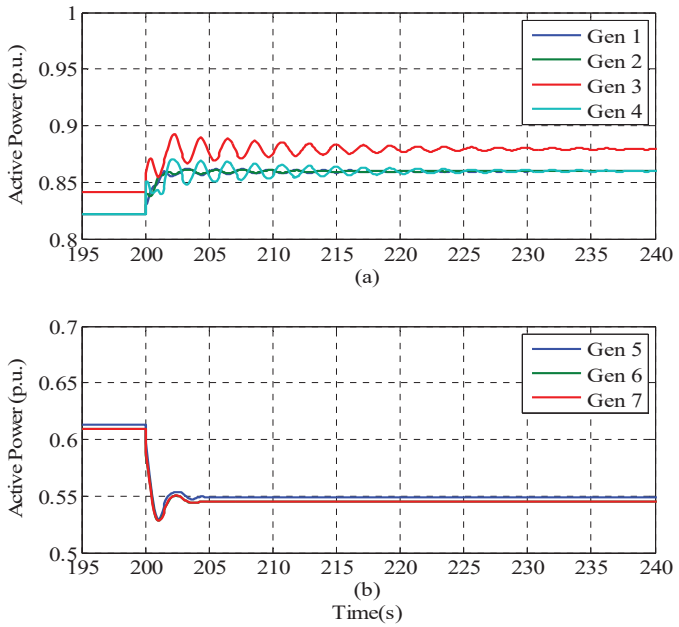

Figure 3-30 : Active power output of all generators

Figure 3-30 shows active power outputs of generators in both grids. There is power system oscillation in Grid A that is clearly visible in the time domain plots of frequency and power output in Figure 3-29 and Figure 3-30(a).

The effect of step change in power reference can be observed in the internal variables of the converters, in Figure 3-31. More precisely, Figure 3-31(a) shows the voltage between the dc terminals of MMC#1. Furthermore, Figure 3-31(b) depicts the zero-sequence of the circulating currents of both MMC converters. Note that this variable is strongly related to the dc current flowing out of the converter into the cable, carrying information on the active power transfer in both converters. In this case, the circulating current of MMC#2 is stepping up following the reference step change of the active power, whereas the MMC#1 is counteracting its effect such that its energy sum variable stays regulated to the desired reference, as illustrated in Figure 3-31(c).

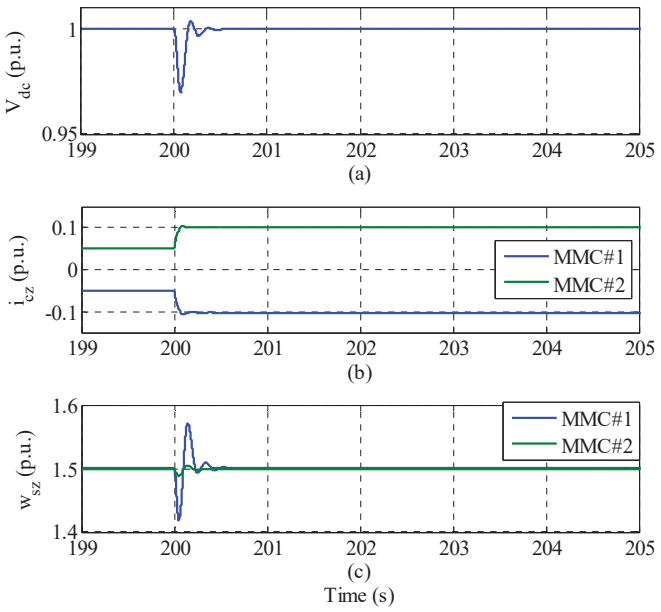

Figure 3-31 : (a) DC link voltage, (b) Zero sequence circulating current, and (c) zero sequence energy sum

3.4. Chapter summary

This chapter presented detailed modelling of both the ac and dc grids in a hybrid ac/dc power system. The differential and algebraic equations that describe the dynamic behavior of the various components of the power system were described. The ac grid modelling included synchronous generators and their controller systems, namely excitation and turbine/governor systems. The dc grid modelling included VSC converters and dc cables. Modelling of both two-level and multi-level converters and their controllers were discussed. Furthermore, an overview was given on how the different DAE equations are combined to form a complete ac/dc power system model, which can be used for dynamic performance and control analysis. Finally, both linear and non-linear model of the ac grid were validated against a commercial simulation tool, DIgSILENT/*PowerFactory*, while the performance of a non-linear hybrid ac/dc power system with two asynchronous ac grids connected via an HVDC link was tested for a step change in power reference.

4. Methods for interaction analysis in hybrid ac/dc power systems

This chapter introduces the analytical methods used in this thesis for dynamic performance assessment and control of a hybrid ac/dc power system.

A hybrid ac/dc power system is a non-linear system and its dynamics are described by non-linear equations. The stability of a non-linear system can be classified into local, finite and global stability [72]. Local stability or stability in a small implies that the system remains within a small region surrounding the equilibrium point when subjected to small perturbation. In the context of a power system, stability in a small (or small-signal stability) refers to the ability of the system to maintain synchronism when subject to a small disturbance [72]. Finite and global stability imply that when the system is subjected to a disturbance, it remains within a finite region or the entire finite space, respectively. Global stability, which refers to transient stability, is also known as stability in the large.

Small-signal stability analysis is conducted using linearized systems. It is based on the assumption that the disturbances are so small that the non-linear differential and algebraic equations describing a system can be linearized at selected steady-state operating condition. The advantages of linearizing the system equations are [88]:

- Analytical methods developed in linear control theory can be applied to analyze the stability and characteristics of a linearized system. In addition, the methods can be used to tune controllers to ensure satisfactory performance of the system.
- If the linearized system is stable at a selected steady-state operating point, then the non-linear system is also stable for the same operating point.
- For very small disturbances, the transient response of the linearized system is the same as that of the original non-linear system. Responses predicted by the linearized model are often sufficiently accurate for practical analysis and design purposes.
- Dynamic performance, such as damping of modes, nature of transient response, etc., of the linearized system can be characterized by the locations of poles in the complex s-plane. Such information can not be gleaned from the results of time domain analysis.

In this thesis, linearized system models are used to study small-signal dynamic interactions in a hybrid ac/dc grid and interaction between control loops, while non-linear system models are used to validate and corroborate findings from the small-signal stability analysis. In addition, non-linear models are used to study frequency stability and large signal interaction between asynchronous ac grids interconnected with a dc grid. Modal analysis and decentralized control analysis methods are introduced in the following sections. These methods are used in this thesis for identification and analysis of interactions in a hybrid ac/dc power system.

4.1. Modal analysis

4.1.1. Concept of a state and state equations

The state of a system represents the minimum amount of information about the system, at any time t_o, that is necessary to determine the system's future behavior without reference to the input before t_o [88]. State variables are a minimum set of linearly independent system variables that can be used to describe the state of a system. The future behavior of a system and its outputs can be determined from the initial values of the state variables at time t_o, inputs signals at time $t \geq t_o$ and equations describing the dynamics of the system. The state of a system is unique regardless of the choice of state variables.

The state-space model of a dynamic system represents a system in terms of a set of n first-order non-linear differential equations of the form:

$$\dot{\mathbf{x}} = \mathbf{f}(\mathbf{x}, \mathbf{u}, t) \tag{4.1}$$

where $\mathbf{x}$ is the state vector with n state variables, $\mathbf{u}$ is the input vector with r input variables, t is time and $\dot{\mathbf{x}}$ is a vector of derivatives of the state variables x with respect to time. Derivatives of state variables of autonomous systems, such as the power system, are not explicit functions of time [72]. In such systems, (4.1) becomes only a function of the state and input variables. Similarly, the outputs of a dynamic system are described as a function of the state and input variables as:

$$\mathbf{y} = \mathbf{g}(\mathbf{x}, \mathbf{u}) \tag{4.2}$$

where $\mathbf{y}$ is vector with m output variables and $\mathbf{g}$ is a function relating state and input vectors to the output vector.

Assume that the small signal stability of a system is investigated at an equilibrium point, where the initial state and input vectors are $\mathbf{x_o}$ and $\mathbf{u_o}$, respectively. Equilibrium or steady state points are those points where all system variables are constant and unvarying with time, and all derivatives of the state variables are zero. For a small perturbation, the state and initial vectors become:

$$\mathbf{x} = \mathbf{x_o} + \Delta\mathbf{x} \qquad \mathbf{u} = \mathbf{u_o} + \Delta\mathbf{u} \tag{4.3}$$

where the prefix Δ denotes small deviation. As the perturbations are assumed to be small, the non-linear function $f_i(\mathbf{x},\mathbf{u})$ in (4.1), for i=1,2,...,n ,can be expressed in terms of Taylor's series expansion with second and higher order terms neglected:

$$\begin{aligned} \dot{x}_i = \dot{x}_0 + \Delta\dot{x}_i &= f_i[(\mathbf{x_o} + \Delta\mathbf{x}),(\mathbf{u_o} + \Delta\mathbf{u})] \\ &= f_i(\mathbf{x_o},\mathbf{u_o}) + \frac{\partial f_i}{\partial x_1}\Delta x_1 + ... + \frac{\partial f_i}{\partial x_n}\Delta x_n + \frac{\partial f_i}{\partial u_1}\Delta u_1 + ... + \frac{\partial f_i}{\partial u_r}\Delta u_r \end{aligned} \tag{4.4}$$

Since $\dot{x}_{i0} = f_i(\mathbf{x_o},\mathbf{u_o})$, (4.4) can be simplified as:

$$\Delta\dot{x}_i = \frac{\partial f_i}{\partial x_1}\Delta x_1 + ... + \frac{\partial f_i}{\partial x_n}\Delta x_n + \frac{\partial f_i}{\partial u_1}\Delta u_1 + ... + \frac{\partial f_i}{\partial u_r}\Delta u_r \tag{4.5}$$

Similarly, the linearized form of the output equation (4.2) is written as:

$$\Delta y_j = \frac{\partial g_j}{\partial x_1}\Delta x_1 + ... + \frac{\partial g_j}{\partial x_n}\Delta x_n + \frac{\partial g_j}{\partial u_1}\Delta u_1 + ... + \frac{\partial g_j}{\partial u_r}\Delta u_r \tag{4.6}$$

where j=1,2,...,m. The linearized state space equations in (4.5) and (4.6) can be written in a compact form as:

$$\begin{aligned} \Delta\dot{\mathbf{x}} &= \mathbf{A}\Delta\mathbf{x} + \mathbf{B}\Delta\mathbf{u} \\ \Delta\mathbf{y} &= \mathbf{C}\Delta\mathbf{x} + \mathbf{D}\Delta\mathbf{u} \end{aligned} \tag{4.7}$$

where $\mathbf{A}$, $\mathbf{B}$, $\mathbf{C}$, and $\mathbf{D}$ are called state, input, output, and feed-forward matrices, respectively. The elements of $\mathbf{A}$ and $\mathbf{B}$ are the coefficients of the state variables and input variables in (4.5), respectively, whereas the elements of $\mathbf{C}$ and $\mathbf{D}$ are the coefficients of the state variables and input variables in (4.6), respectively. The Laplace transform of the state equation (4.7) gives:

$$
\begin{aligned}
s\Delta\mathbf{x}(s) - \Delta\mathbf{x}(0) &= A\Delta\mathbf{x}(s) + \mathbf{B}\Delta\mathbf{u}(s) \\
\Delta\mathbf{y}(s) &= \mathbf{C}\Delta\mathbf{x}(s) + \mathbf{D}\Delta\mathbf{u}(s)
\end{aligned}
\tag{4.8}
$$

Rearranging and simplifying (4.8):

$$
\begin{aligned}
\Delta\mathbf{x}(s) &= (s\mathbf{I} - \mathbf{A})^{-1}\left[\Delta\mathbf{x}(0) + \mathbf{B}\Delta\mathbf{u}(s)\right] \\
&= \frac{adj(s\mathbf{I} - \mathbf{A})}{det(s\mathbf{I} - \mathbf{A})}\left[\Delta\mathbf{x}(0) + \mathbf{B}\Delta\mathbf{u}(s)\right] \\
\Delta\mathbf{y}(s) &= \mathbf{C}\frac{adj(s\mathbf{I} - \mathbf{A})}{det(s\mathbf{I} - \mathbf{A})}\left[\Delta\mathbf{x}(0) + \mathbf{B}\Delta\mathbf{u}(s)\right] + \mathbf{D}\Delta\mathbf{u}(s)
\end{aligned}
\tag{4.9}
$$

The poles of $\Delta\mathbf{x}$(s) and $\Delta\mathbf{y}$(s) in (4.9) are roots of the equation:

$$
det(s\mathbf{I} - \mathbf{A}) = 0 \tag{4.10}
$$

Equation (4.10) is referred as the *characteristic equation* of matrix $\mathbf{A}$, and the real or complex values of s, which satisfy the *characteristic equation*, are called *eigenvalues* of matrix $\mathbf{A}$. The small-signal stability of a non-linear system is given by its eigenvalues. If all eigenvalues have negative real parts, then the system is asymptotically stable or returns to its original state. If at least one of the eigenvalues has a positive real part, then the system is unstable.

Eigenvalues or modes are usually denoted by the symbol $\lambda = \sigma \pm j\omega$. The real component of an eigenvalue gives the damping, while the imaginary component gives the frequency of oscillation.

$$
\begin{aligned}
f &= \frac{\omega}{2\pi} \\
\zeta &= \frac{-\sigma}{\sqrt{\sigma^2 + \omega^2}}
\end{aligned}
\tag{4.11}
$$

where f is the frequency of oscillation and ζ is the damping ratio. Real eigenvalues ($\lambda = \sigma$) are associated with a monotonic response, which in time domain has the form $y(t)=Ke^{\sigma t}$ (where K is a constant). Complex conjugate pair of eigenvalues ($\lambda = \sigma \pm j\omega$) are associated with an oscillatory response, which in time domain has the form $y(t)=Ke^{\sigma t}\sin(\omega t+\phi)$. A negative real part implies damped oscillations whereas a positive real part implies oscillations of increasing amplitude.

4.1.2. Eigenvectors

Each eigenvalue of an n-by-n state matrix $\mathbf{A}$, λ_i, is the non-trivial solution of:

$$\mathbf{A}\boldsymbol{\phi}_i = \lambda_i \boldsymbol{\phi}_i \tag{4.12}$$

where $\boldsymbol{\phi}_i$ is an n-element column vector called the right eigenvector of matrix $\mathbf{A}$ associated with the eigenvalue λ_i. For a non-trivial solution, i.e. $\boldsymbol{\phi}_i \neq \mathbf{o}$, the determinant of $\lambda_i\mathbf{I}-\mathbf{A}$ must be zero or $det(\lambda_i\mathbf{I}-\mathbf{A})=0$, which is the same as the characteristics equation given in (4.10).

Similarly, there exists an n-element row vector $\boldsymbol{\psi}_i$ = [ψ_{i1} ψ_{i2}...ψ_{in}] which satisfies the equation:

$$\boldsymbol{\psi}_i\mathbf{A} = \lambda_i\boldsymbol{\psi}_i \tag{4.13}$$

$\boldsymbol{\psi}_i$ is called left eigenvector of matrix $\mathbf{A}$ corresponding to eigenvalue λ_i. Elements of $\boldsymbol{\phi}_i$ indicate the relative activity of the state variables when λ_i is excited, while elements $\boldsymbol{\psi}_i$ indicate which combination of state variables display only λ_i [72].

The left and right eigenvectors corresponding to different eigenvalues are orthogonal, i.e. their dot product is zero. However, the dot product of left and right eigenvectors corresponding to the same eigenvalue is a non-zero constant. Both (4.12) and (4.13) are homogenous equation, i.e. any scalar k multiple of the vectors, $k\boldsymbol{\phi}_i$ and $k\boldsymbol{\psi}_i$, are also valid solutions. By making use of this property, it is common to normalize the vectors so that their dot product becomes one. Therefore, for any eigenvalue, $\boldsymbol{\psi}_i\boldsymbol{\phi}_i$=1 due to the normalization.

If $\boldsymbol{\Phi}$ is defined as a matrix of the n-column right eigenvector, and $\boldsymbol{\Psi}$ as a matrix of n-row left eigenvectors corresponding to the eigenvalues λ_1, λ_2, λ_3, ... λ_n as in:

$$\begin{aligned}\boldsymbol{\Phi} &= \begin{bmatrix}\boldsymbol{\phi}_1 & \boldsymbol{\phi}_2 & \cdots & \boldsymbol{\phi}_n\end{bmatrix} \\ \boldsymbol{\Psi} &= \begin{bmatrix}\boldsymbol{\psi}_1^T & \boldsymbol{\psi}_2^T & \cdots & \boldsymbol{\psi}_n^T\end{bmatrix}^T\end{aligned} \tag{4.14}$$

then (4.12) and (4.13) can be written in terms of the $\boldsymbol{\Phi}$ and $\boldsymbol{\Psi}$ as:

$$\mathbf{A}\boldsymbol{\Phi} = \boldsymbol{\Phi}\boldsymbol{\Lambda} \qquad \boldsymbol{\Psi}\mathbf{A} = \boldsymbol{\Lambda}\boldsymbol{\Psi} \tag{4.15}$$

where $\mathbf{\Lambda}$ is a diagonal matrix with all eigenvalues along the diagonal, diag($\lambda_1, \lambda_2, \lambda_3, \ldots \lambda_n$). Due to normalization of right and left eigenvectors corresponding to the same eigenvalue, the product of $\mathbf{\Phi}$ and $\mathbf{\Psi}$ is an identity matrix, i.e. $\mathbf{\Psi\Phi = I}$ and $\mathbf{\Psi = \Phi^{-1}}$. Accordingly, (4.15) can be re-written as:

$$\mathbf{\Phi^{-1}A\Phi = \Lambda} \qquad \mathbf{\Psi A\Phi = \Lambda} \tag{4.16}$$

4.1.3. Observability and Controllability for decoupled systems

Equation (4.7) represents the physical system, and the rate of change of each state variable is a linear combination of all the state variables. Thus, a cross-coupling exists between the states variables. This cross-coupling makes it difficult to understand the relationship between eigenvalues and state variables. Therefore, a decoupled state equation is derived where the rate of change of a pseudo-state variable is a function of a single mode and the pseudo-state variable itself. The pseudo-state variable z is related to the original state variable x according to the transformation:

$$\mathbf{\Delta x = \Phi z} \qquad \mathbf{\Delta \dot{x} = \Phi \dot{z}} \tag{4.17}$$

Substituting (4.17) into (4.7):

$$\begin{aligned} \mathbf{\Phi \dot{z} &= A\Phi z + B\Delta u} \\ \mathbf{\Delta y &= C\Phi z + D\Delta u} \end{aligned} \tag{4.18}$$

Simplifying (4.18) and using (4.16), a decoupled state equation is written as:

$$\begin{aligned} \mathbf{\dot{z} &= \Lambda z + B'\Delta u} \\ \mathbf{\Delta y &= C'z + D\Delta u} \end{aligned} \tag{4.19}$$

where

$$\mathbf{B' = \Phi^{-1}B = \Psi B} \tag{4.20}$$

$$\mathbf{C' = C\Phi} \tag{4.21}$$

Contrary to (4.7), there is no cross-coupling between the pseudo-states variables in (4.19) as $\mathbf{\Lambda}$ is a diagonal matrix. Thus, the name decoupled state equation. The rate of change of each pseudo-states variable is related to itself through a single mode, which means the response of the pseudo-states variable is related to a single mode only.

The nxr matrix $\mathbf{B}' = \mathbf{\Psi B}$ is called mode controllability matrix, while the mxn matrix $\mathbf{C}' = \mathbf{C\Phi}$ is called mode observability matrix. A mode λ_i is controllable from input u_q if and only if the product of the i^{th} row of the left eigenvector matrix and the q^{th} column of the input matrix is different from zero, i.e. $b'_{iq} = \mathbf{\psi}_i \mathbf{b}_q \neq 0$. Thus, b'_{iq} measures the controllability λ_i of from input u_q. If the i^{th} row of $\mathbf{B}'$ is zero, then λ_i can not be controlled from any of the inputs. In such cases, the mode is said to be uncontrollable. Likewise, mode λ_i is observable in output signal y_m if and only if the product of m^{th} row of the output matrix and the i^{th} column of the right eigenvector matrix is different from zero, i.e. $c'_{mi} = \mathbf{c}_m \mathbf{\phi}_i \neq 0$. Thus, c'_{mi} is measures the observability of λ_i in the output y_m. If the i^{th} column of $\mathbf{C}'$ is zero, then λ_i can not be observed on any of the outputs. In such cases, λ_i is said to be unobservable.

For a controller to be effective at modal frequency of λ_i, the feedback signal y and the control input u should have a high relative observability and controllability, respectively, of the mode. Selection of controller input and output signals based on mode controllability and observability measures is presented in Chapter 6.

4.1.4. Free motion (natural) response

From (4.8), the state variable x in the frequency domain is:

$$\mathbf{\Delta x}(s) = (s\mathbf{I} - \mathbf{A})^{-1}\mathbf{\Delta x}(0) + (s\mathbf{I} - \mathbf{A})^{-1}\mathbf{B}\mathbf{\Delta u}(s) \tag{4.22}$$

The first term on the right side of (4.22) is referred as the natural or unforced response while the second term is referred as the forced response. The natural response is response of the system to non-zero initial conditions only, with zero inputs to the system ($\mathbf{\Delta u}(s) = \mathbf{o}$). The forced response is the response of the system to the inputs only, with the zero initial conditions ($\mathbf{\Delta x}(0) = \mathbf{o}$).

With the relationship between the original and pseudo-states variables defined as $\mathbf{\Delta x} = \mathbf{\Phi z}$, and the decoupled state equation defined as $\dot{\mathbf{z}} = \mathbf{\Lambda z} + \mathbf{B}'\mathbf{u}$, the natural time domain response of the system with no external excitation at the inputs is:

$$\begin{aligned} \mathbf{z}(t) &= L^{-1}\left\{(s\mathbf{I} - \mathbf{\Lambda})^{-1}\right\} \cdot \mathbf{z}(0) \\ &= L^{-1}\left\{ diag\left(\frac{1}{s-\lambda_1}, \frac{1}{s-\lambda_2}, ..., \frac{1}{s-\lambda_n} \right) \right\} \cdot \mathbf{z}(0) \end{aligned} \tag{4.23}$$

Solving (4.23) gives:

$$\mathbf{z}(t)=\begin{bmatrix} e^{\lambda_1 t} & 0 & \dots & 0 \\ 0 & e^{\lambda_2 t} & \dots & 0 \\ \vdots & \vdots & \ddots & \vdots \\ 0 & 0 & \dots & e^{\lambda_n t} \end{bmatrix}\cdot\mathbf{z}(0)=diag\left(e^{\lambda_1 t},e^{\lambda_2 t},...,e^{\lambda_n t}\right)\cdot\mathbf{z}(0) \tag{4.24}$$

Expressing (4.24) in terms of the original state variables but retaining the decoupled modes gives:

$$\begin{aligned} &\Delta\mathbf{x}(t)=\mathbf{\Phi}\mathbf{z}(t) \\ &\Delta\mathbf{x}(t)=\mathbf{\Phi}\underbrace{diag\left\{e^{\lambda_1 t},e^{\lambda_2 t},...,e^{\lambda_n t}\right\}\overbrace{\mathbf{\Psi}\cdot\mathbf{x}(0)}^{\mathbf{z}(0)}}_{\mathbf{z}(t)}, \quad or \\ &\Delta\mathbf{x}(t)=\sum_{i=1}^{n}\boldsymbol{\phi}_i e^{\lambda_i t}\left[\boldsymbol{\psi}_i\mathbf{x}(0)\right] \end{aligned} \tag{4.25}$$

Then, the free motion time response of the i^{th} state variable is expressed in terms of all eigenvalues of the system, and left and right eigenvectors as:

$$\Delta x_i(t)=\phi_{i1}c_1e^{\lambda_1 t}+\phi_{i2}c_2e^{\lambda_2 t}+\dots+\phi_{in}c_ne^{\lambda_n t} \tag{4.26}$$

where $\mathbf{c}_i=\boldsymbol{\psi}_i\Delta\mathbf{x}(0)$ represents the magnitude of excitation of the i^{th} mode resulting from the initial conditions. If the initial conditions of the states are set equal to the right eigenvector of the j^{th} eigenvalue, then $\mathbf{c}_i$ becomes a zero vector except for the j^{th} element, which has a value $\boldsymbol{\psi}_j\boldsymbol{\phi}_j=1$. This means, only mode j is excited. Therefore, (4.26) becomes:

$$\Delta x_i(t)=\phi_{ij}e^{\lambda_j t} \tag{4.27}$$

which is the modal response of i^{th} state variable to the j^{th} eigenvalue. Any initial condition vector can be represented by a linear combination of the n right eigenvectors. Then, the response of the system will be the superposition of the response of the n modes.

4.1.5. Mode shapes

The natural response of a system when the initial conditions lie along one of its right eigenvectors is called modal response of the system. The modal responses for any mode λ_i, $\Delta\mathbf{x}(t)=\boldsymbol{\phi}_i e^{\lambda_i t}$, have identical form. This means all variables in $\Delta\mathbf{x}$ will have a

monotonically decaying response if λ_i is negative real value or a monotonically decaying oscillatory response with the frequency of λ_i if the λ_i is complex. However, the initial amplitude of each variable's response, referred as mode shape, is determined by the elements of $\boldsymbol{\phi}_i$.

A mode shape gives the relative activity of a state variable when a particular mode is excited. The degree of activity of the state variable x_k in the i^{th} mode is given by the element of ϕ_{ki} of the right eigenvector $\boldsymbol{\phi}_i$. However, the numerical values of $|\phi_{ki}|$ depend on the units selected for the associated state variables, e.g. speed in p.u. and angle in radians. Therefore, the values are not dimensionless and are scaling dependent. The relative phase between mode shapes reveals the relative phase between the modal responses of the state variables. For example, the relative phase between modal responses of speed state variables shows how machines in a system are swinging with respect to each other.

The application of mode shapes in interaction analysis, and their relationship with the observability matrix $\mathbf{C}'$ in (4.21) is explained in detail in Chapter 5.

4.1.6. Participation factor analysis

As mentioned above, mode shapes show the relationship between states and a mode. However, due their dependency on dimension and scaling, they can not be used to make a comparison between the all states. On the other hand, participation factors are dimensionless and can be used to determine the degree to which a mode participates in a state or states participate in a mode.

Participation of a mode in a state: Assume that only the k^{th} state is excited in the initial condition with a unit vector, i.e.

$$\mathbf{x(0)} = \begin{bmatrix} x_1(0) \\ \vdots \\ x_k(0) \\ \vdots \\ x_n(0) \end{bmatrix} = \begin{bmatrix} 0 \\ \vdots \\ 1 \\ \vdots \\ 0 \end{bmatrix} \tag{4.28}$$

Then, the time domain equation (4.25) becomes:

$$\Delta\mathbf{x}(t)=\sum_{i=1}^{n}\phi_i e^{\lambda_i t}\left[\boldsymbol{\psi}_i\mathbf{x}(0)\right]$$

$$\begin{bmatrix}\Delta x_1(t)\\ \vdots\\ \Delta x_k(t)\\ \vdots\\ \Delta x_n(t)\end{bmatrix}=\begin{bmatrix}\phi_{11}\\ \vdots\\ \phi_{k1}\\ \vdots\\ \phi_{n1}\end{bmatrix}\psi_{1k}e^{\lambda_1 t}+\ldots+\begin{bmatrix}\phi_{1k}\\ \vdots\\ \phi_{kk}\\ \vdots\\ \phi_{nk}\end{bmatrix}\psi_{kk}e^{\lambda_k t}+\ldots+\begin{bmatrix}\phi_{1n}\\ \vdots\\ \phi_{kn}\\ \vdots\\ \phi_{nn}\end{bmatrix}\psi_{nk}e^{\lambda_n t} \tag{4.29}$$

Even though only the k^{th} state is excited in the initial conditions, all eigenvalues are excited in (4.29). If only $\Delta x_k(t)$ is considered:

$$\Delta x_k(t)=\phi_{k1}\psi_{1k}e^{\lambda_1 t}+\ldots+\phi_{kk}\psi_{kk}e^{\lambda_k t}+\ldots+\phi_{kn}\psi_{nk}e^{\lambda_n t} \tag{4.30}$$

The participation of the i^{th} eigenvalue in the k^{th} state is:

$$p_{ik}=\phi_{ki}\psi_{ik}=\psi_{ik}\phi_{ki} \tag{4.31}$$

Thus, (4.30) can be re-written in terms of participation factors as:

$$\Delta x_k(t)=p_{1k}e^{\lambda_1 t}+\ldots+p_{kk}e^{\lambda_k t}+\ldots+p_{nk}e^{\lambda_n t}=\sum_{i=1}^{n}p_{ik}e^{\lambda_i t} \tag{4.32}$$

Due to the normalization of eigenvectors corresponding to the same eigenvalue, the summation of all participation factors of a state is equal to one. $\boldsymbol{\phi}_k\boldsymbol{\psi}_k=1$ is dimensionless. Therefore, the elements of the participation factors $\phi_{ki}\psi_{ik}$ are also dimensionless and invariant under the changes in the units of the state variables of the system. p_{ik} provides a measure of the relative extent to which the i^{th} eigenvalue participates in the state k at time t=0: it is therefore known as the participation factor of the i^{th} eigenvalue in the k^{th} state.

Participation of a state in a mode: Assume that all states are excited in turn in the initial conditions with a unit vector. This is the same as (4.28), but this time, the excitation is done for all states and one state at a time. Then, the equation for each state for the different excitations, which is equivalent to (4.30), is:

$$\begin{aligned}
\Delta x_1(t) = &\ \phi_{11}\psi_{11}e^{\lambda_1 t} + \cdots + \phi_{1k}\psi_{k1}e^{\lambda_k t} + \cdots + \phi_{1n}\psi_{n1}e^{\lambda_n t} \\
&\cdots \qquad\qquad \cdots \qquad\qquad \cdots \\
\Delta x_k(t) = &\ \phi_{k1}\psi_{1k}e^{\lambda_1 t} + \cdots + \phi_{kk}\psi_{kk}e^{\lambda_k t} + \cdots + \phi_{kn}\psi_{nk}e^{\lambda_n t} \\
&\cdots \qquad\qquad \cdots \qquad\qquad \cdots \\
\Delta x_n(t) = &\ \phi_{n1}\psi_{1n}e^{\lambda_1 t} + \cdots + \phi_{nk}\psi_{kn}e^{\lambda_k t} + \cdots + \phi_{nn}\psi_{nn}e^{\lambda_n t}
\end{aligned} \tag{4.33}$$

Substituting (4.31) into the coefficients of the exponential terms in equation (4.33) (e.g. $p_{1k} = \phi_{k1}\psi_{1k}$):

$$\begin{bmatrix} \Delta x_1(t) \\ \vdots \\ \Delta x_k(t) \\ \vdots \\ \Delta x_n(t) \end{bmatrix} = \begin{bmatrix} p_{11} \\ \vdots \\ p_{1k} \\ \vdots \\ p_{1n} \end{bmatrix} e^{\lambda_1 t} + \ldots + \begin{bmatrix} p_{k1} \\ \vdots \\ p_{kk} \\ \vdots \\ p_{kn} \end{bmatrix} e^{\lambda_k t} + \ldots + \begin{bmatrix} p_{n1} \\ \vdots \\ p_{nk} \\ \vdots \\ p_{nn} \end{bmatrix} e^{\lambda_n t} \tag{4.34}$$

The sum of the participation factors in the columns is equal to 1. For the k^{th} eigenvalue, p_{kn} provides a measure of the relative extent to which n^{th} state participates in the mode. The elements of the k^{th} column of the participation factor matrix show the extent to which each state participates in the k^{th} eigenvalue.

4.2. Control loop interaction analyses

4.2.1. Multiple-Input Multiple-Output power system

The power system is a complex system that is composed of many controllers regulating different variables to achieve the desired level of system performance. Therefore, the power system can be considered as a multiple-input-multiple-output (MIMO) system.

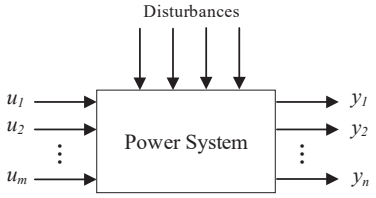

Figure 4-1: MIMO system

A characteristic feature of MIMO systems is the existence of multiple control loops, and the presence of interaction between these loops, i.e. each manipulated variable can simultaneously affect several controlled variables. To illustrate this feature, consider the power system representation depicted in Figure 4-1, where u_i, $i=1,2,...,m$ are the manipulated variables and y_i, $i=1,2,...,n$ are the controlled variables. The MIMO transfer function, $G(s)$, from outputs y to inputs u for the system depicted in Figure 4-1, is given by:

$$\mathbf{G}(s)=\begin{bmatrix} g_{11}(s) & g_{12}(s) & \cdots & g_{1m}(s) \\ g_{21}(s) & g_{22}(s) & \cdots & g_{2m}(s) \\ \vdots & \vdots & \ddots & \vdots \\ g_{m1}(s) & g_{m2}(s) & \cdots & g_{mm}(s) \end{bmatrix} \tag{4.35}$$

where $g_{ij}(s)$ is the transfer function from input j to output i. For convenience, it is assumed in (4.35) that the number of manipulated variables is equal to the number of controlled variables, i.e. $m=n$, such that a single controlled variable or output is paired with a single manipulated variable via a single feedback controller $G_{ci}(s)$. In general, a change in a manipulated variable, say u_1, will affect several or all of the controlled variables to different degrees. Suppose a disturbance causes the output y_1 to deviate from its set point. Then, the following sequence of events can occur:

1) The controller, $G_{c1}(s)$, will manipulate u_1 to restore the value of y_1. However, changing u_1 also affects the other outputs $y_2, y_3, \ldots, y_m$ through the transfer functions $g_{21}(s), g_{31}(s), \ldots, g_{m1}(s)$, respectively

2) The effect of u_1 on the other outputs triggers respective controllers to act to restore the outputs to their set-point values by manipulating the respective variables $u_2, u_3, \ldots, u_m$. However, changing $u_2, u_3, \ldots, u_m$ also affects u_1 through $g_{12}(s), g_{13}(s), \ldots, g_{1m}(s)$.

Therefore, controller actions will proceed continuously and simultaneously until a new steady state is attained. Hence, control action on y_1 is twofold: (i) a direct effect resulting from manipulation of u_1, and (ii) an indirect effect via control loop interactions.

The level of interaction between inputs and outputs in MIMO systems can be assessed using several measures [89-92]. One such measure, which is used in this thesis, is relative gain array [92].

4.2.2. Relative Gain Array

Relative gain array (RGA) is a measure of influence of one control loop on another. The two-input two-output plant model shown in Figure 4-2 is used to illustrate the interpretation of relative gain array.

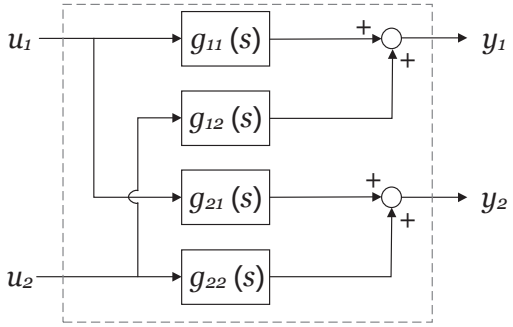

Figure 4-2: 2x2 plant model

The plant equation is:

$$\begin{aligned} y_1 &= g_{11}(s)u_1 + g_{12}(s)u_2 \\ y_2 &= g_{21}(s)u_1 + g_{22}(s)u_2 \end{aligned} \tag{4.36}$$

Here, we are only concerned about input or output deviations. Assume that u_1 is used to control y_1. First consider the extreme case where the other loop is open, i.e. u_2 = 0. The relationship between y_1 and u_1 becomes:

$$u_2 = 0: \quad y_1 = g_{11}(s)u_1 \tag{4.37}$$

Then, consider another extreme case where the other loop is closed with perfect control, i.e. y_2 is kept constant (deviation of y_2 =0). The gain from u_1 to y_1 becomes:

$$\begin{aligned} y_2 = 0: \quad y_1 &= \left(g_{11}(s) - \frac{g_{21}(s)}{g_{22}(s)} g_{12}(s) \right) \cdot u_1 \\ &= \hat{g}_{11}(s) \cdot u_1 \end{aligned} \tag{4.38}$$

It should be noted that perfect control is only possible at steady state (provided that there is an integral action), but it is a good approximation at frequencies within the bandwidth of each loop [93]. From (4.37) and (4.38), it can be observed that the gain between u_1 and y_1 changes when the other loop is closed. A relative gain array element μ_{11} for loop y_1- u_1 is the ratio of (4.37) to (4.38):

$$\mu_{11} = \frac{open\ loop\ gain(with\ u_2=0)}{closed\ loop\ gain(with\ y_2=0)} = \frac{g_{11}(s)}{\hat{g}_{11}(s)} = \frac{1}{1-\frac{g_{12}(s)g_{21}(s)}{g_{11}(s)g_{22}(s)}} \tag{4.39}$$

μ_{11} equal to 1 represents an ideal case where the loop y_1-u_1 has no interaction with other loops in the plant. However, μ_{11} different from 1 indicates that the gain from u_1 to y_1 changes when the other loops are closed. This implies interaction between the loops. If RGA elements for the other loops, i.e. y_1-u_2, y_2-u_1, y_2-u_2, are calculated following the same procedure outlined above, then the RGA matrix for the plant in Figure 4-2 becomes:

$$\mathrm{M}(G) = \begin{bmatrix} \mu & 1-\mu \\ 1-\mu & \mu \end{bmatrix} \tag{4.40}$$

where μ is as in (4.39).

Relative gain array (RGA) is defined as the ratio of open loop gain when all other inputs are zero to closed loop gain when all the other outputs are closed with perfect control. For a general MIMO system with non-singular square complex matrix $G(s)$, as in (4.35), the RGA element on the i^{th} row and j^{th} column is calculated as:

$$\mu_{ij} = \frac{open\ loop\ gain(with\ u_k=0, \forall k \neq j)}{closed\ loop\ gain(with\ y_k=0, \forall k \neq i)} \tag{4.41}$$

As much as possible, pairings with close to one RGA should be selected and pairings that result in negative RGA element should be avoided. Some of the important algebraic properties of RGA include[92, 93]:

- The sum of rows and columns of the RGA matrix is equal to 1
- It is independent of input and output scaling, i.e. $M(G)= M(D^{-1}GD)$, where D^{-1} and D are two general diagonal matrices

- RGA is an identity matrix if *G* is upper or lower triangular

When the RGA was first introduced by Bristol in 1966 [92], it only considered steady-state gain, G(0), at s=0. Later, a dynamic extension of RGA (DRGA) was proposed, where the RGA can be evaluated at any frequency. Dynamic RGA is a square complex matrix:

$$RGA = \mathrm{M}(G(j\omega)) \triangleq G(j\omega).*(G(j\omega)^{-1})^{T} \tag{4.42}$$

where .* denotes element-by-element multiplication or Hadamard product. In decentralized control, it is important that the *M(G(jω))* is close to identity matrix at the cross-over frequency [93].

4.2.3. Performance relative gain array

Consider a square *mxm* multi-variable plant *G(s)*, where a decentralized control is going to be implemented. The columns and rows of *G(s)* can be rearranged so that the paired elements are along the diagonal of *G(s)*. Then, decentralized feedback controller's transfer function, *K(s)*, becomes a diagonal matrix. $\tilde{G}(s)$ is defined as a matrix consisting of the diagonal elements of *G(s)*, as in (4.43).

$$\tilde{G}(s) \triangleq diag\{g_{ii}\} = \begin{bmatrix} g_{11}(s) & & & \\ & g_{22}(s) & & \\ & & \ddots & \\ & & & g_{mm}(s) \end{bmatrix} \tag{4.43}$$

With decentralized feedback control, the off-diagonal elements of $G(s)-\tilde{G}(s)$, which is the difference between the plant transfer function *G(s)* and the diagonal matrix $\tilde{G}(s)$, gives the interactions between different inputs and outputs loops. The performance relative gain array (PRGA) is calculated as:

$$PRGA = \Gamma(s) \triangleq \tilde{G}(s)\, G^{-1}(s) = \begin{bmatrix} \gamma_{11} & \gamma_{12} & \cdots & \gamma_{1m} \\ \gamma_{21} & \gamma_{22} & \cdots & \gamma_{2m} \\ \vdots & \vdots & \ddots & \vdots \\ \gamma_{m1} & \gamma_{m2} & \cdots & \gamma_{mm} \end{bmatrix} \tag{4.44}$$

The PRGA is frequency dependent. The diagonal elements of the PRGA are the same as the diagonal elements of the RGA, i.e. $\gamma_{ii} = \mu_{ii}$. The off-diagonal elements are the ones that indicate interactions, i.e. PRGA element γ_{ij} indicates the effect input *j* has on output *i*. At frequencies where feedback controller is effective, large PRGA elements, compared to 1 in magnitude, entail that the interactions *"slow down"* the overall response. On the other hand, small PRGA elements, compared to 1, mean interactions actually *augment* performance. Γ=1 entails perfect decoupling.

PRGA differs from the RGA/DRGA in that the PGRA gives information on "*one-way interaction*" between loops, i.e. it provides an indication of the nature as well as the extent of interactions. On the other hand, RGA gives information on "*two-way interaction*", i.e. it is merely indicative of the existence of interaction [93].

4.3. Chapter summary

In this chapter, modal analysis and control loop interaction analysis methods were presented. These methods are used in this thesis for dynamic performance assessment and control of a hybrid ac/dc power system. Modal analysis method is used to study the small-signal stability of a non-linear system. The concept of state was introduced before discussing eigenvalues, eigenvectors, participation factors and their interpretations. In addition, methods for decentralized controllers design and interaction analysis in multi-input-multi-output (MIMO) systems such as the power system were also presented in this chapter. Relative gain array measures the level of interactions between inputs and outputs in MIMO systems; while a variation of relative gain array called performance relative gain array gives an insights into the nature of interactions.

5. Interaction analyses – Electro-mechanical dynamics

In this chapter, interaction between asynchronous ac grids connected through a multi-terminal dc (MTDC) grid is analyzed. The term interaction is used to refer to the existence of dynamic coupling between subsystems. The interaction could be significant or insignificant, and it could affect positively or negatively the stability of a subsystem. However, the main objective of this chapter is the identification of the existence of the interactions or the dynamic couplings. In addition, the work presents how the level of interaction is influenced by different factors. The topics addressed here are:

- How are ac system dynamics influenced by the introduction of dc grid?
- Identification of interaction between ac grids connected via MTDC or ac-to-ac interaction
- How do converter type, MTDC grid control strategy and converter controller tuning affect the level of the interactions?
- How are the interactions levels influenced by ancillary services such as frequency support?
- What kind of conditions amplify the interaction level?

The study uses modal analysis, particularly mode shapes and participation factors, and time domain analysis is used to support results from the modal analysis. Some of the results presented in this chapter are published in [94, 95].

A test system consisting of a four terminal dc grid interconnecting three asynchronous ac grids, which is shown in Figure 5-1, is used in the study. All three ac grids are multi-machine systems representing aggregated power system models of different sizes. Grid A is a two area power system [72] with two generators in each area. Grid B and Grid C are smaller systems with two generators and two loads. The two grids have similar topologies except for the length of the transmission line between the generators, which is 50 km in Grid B and 75 km in Grid C. Simple excitation and turbine/governor systems are used to capture the relevant dynamics of the ac grids in the simplest way possible. Thus, a simple

excitation system (SEXS) model is used with each generator, while steam turbine/governor model TGOV1 is used for power-frequency regulation on generators 1, 3, 5 and 7.

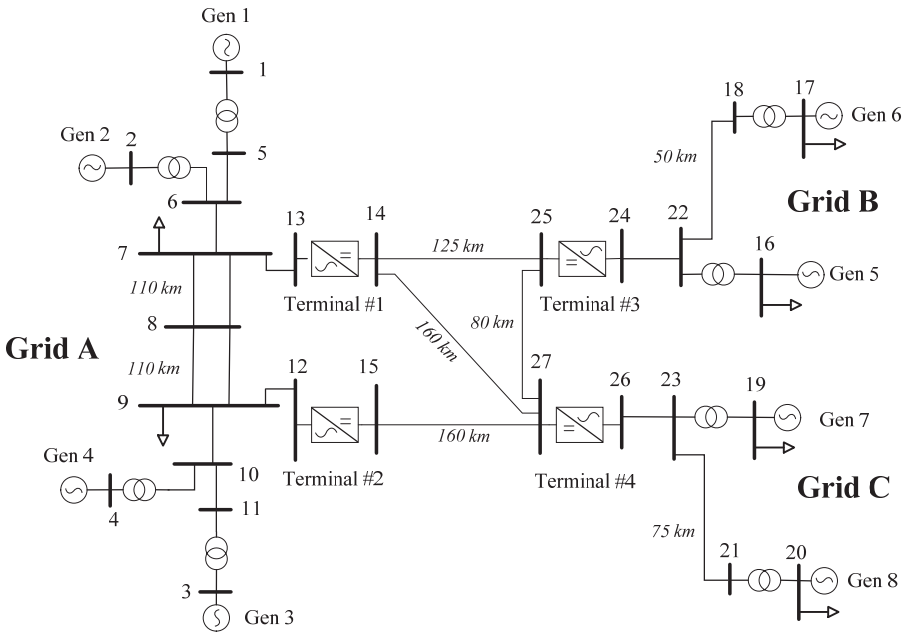

Figure 5-1: Study system

The dc grid has a symmetric monopole configuration with a rating of ±200kV, and all converters in the dc grid have ratings of 900 MW. Unless otherwise specified, the converters are modelled as 2-level VSC and dc cables are modelled as π-models with lumped parameters. The study system was modelled in Simulink/MATLAB.

Two of the dc grid terminals (#1 and #2) are connected to Grid A with two long transmission lines between them on the ac side. The other two dc grid terminals (#3 and #4) are connected to Grid B and C. In the initial operating condition considered for the linear analysis, converters at terminals #1 and #2 operate in rectifier mode, while converters at terminals #3 and #4 operate in inverter mode. All terminals operate in dc voltage droop control mode with 4% droop constant and constant reactive power control model. The initial steady state dc grid voltages and ac side power flow values at the

terminal converters are presented in Table 5-1. A power flow out of the dc grid and into the ac system is defined as positive.

Table 5-1 : Initial power flow values for the study system

	Terminal #1	**Terminal #2**	**Terminal #3**	**Terminal #4**
P [MW]	-496.9	-801.4	591.1	679.8
Q [Mvar]	-50	-50	0	0
Vdc [kV]	401.2	403.6	400	400.8
ρ_{dc} [%]	4	4	4	4
Rating [MVA]	900	900	900	900

5.1. Effect of DC grid interconnection

Two modal analyses were carried out to study how the dynamic behavior of ac grids is affected by the introduction of MTDC systems. First, a linear analysis is carried out separately for each of the three asynchronous ac grids in Figure 5-1. Then, a linear analysis is carried out for the hybrid ac/dc test power system with four terminal dc grid interconnecting the three asynchronous ac grids. The hybrid ac/dc system is studied with focus on ac grid modes. The locations of the ac modes in the complex plane is observed to see whether they change after a dc grid is added compared to the case where the ac grids were operating independently.

In the case of eigenvalue analysis for the individual isolated ac grids, it was found that Grid A has 41 modes, while both Grid B and Grid C have 19 modes each. All eigenvalues have negative real parts indicating stable operating conditions. The state variables are associated with the generators, AVRs and governors in the ac grids. Table 5-2 shows poorly damped modes with damping ratio less than 15% for the different ac grids.

Table 5-2 : AC grid modes with less than 15% damping ratio

Name	Eigenvalue	f [Hz]	ζ [%]	Dominant states
Grid A				
λ_{A1}	-0.21 ± j3.69	0.59	5.7	$\Delta\omega_{A3}$, δ_{A1}, δ_{A2}, $\Delta\omega_{A4}$, E'_{qA4}
λ_{A2}	-0.69 ± j6.91	1.10	9.9	δ_{A3}, $\Delta\omega_{A3}$, $\Delta\omega_{A4}$, E'_{dA4}, δ_{A1}
λ_{A3}	-0.68 ± j6.73	1.07	10.0	δ_{A2}, $\Delta\omega_{A1}$, $\Delta\omega_{A2}$, δ_{A1}, δ_{A3}
Grid B				
λ_{B}	-0.71 ± j6.52	1.04	10.09	δ_{B6}, $\Delta\omega_{B5}$, $\Delta\omega_{B6}$, E'_{dB5}, E'_{dB6}
Grid C				
λ_{C}	-0.57 ± j5.82	0.93	9.7	δ_{C8}, $\Delta\omega_{C8}$, $\Delta\omega_{C7}$, E'_{dC8}, E''_{dC8}

The poorly damped modes in each grid are referred as λ_A, λ_B, and λ_C for simplicity and to make identification of the eigenvalues easier in future references. The last column in Table 5-2 lists state variables that have the top five participation factor for each mode. The most dominant states in all poorly damped eigenvalues are speed and rotor angle. Thus, the eigenvalues are classified as electromechanical modes. Based on the frequency of the modes, it can be estimated that λ_{A1} is an inter-area oscillation mode, where groups of generators in one area oscillate against groups of generators in another area, since frequencies of inter-area modes are typically in the range of 0.4 to 0.7 Hz [72]. Meanwhile, the frequencies of modes λ_{A2}, λ_{A3}, λ_B, and λ_C indicate local plant oscillations (typically 0.7 to 2 Hz), where generators in one area oscillate against each other.

Next, a second eigenvalue analysis was done for a system with an MTDC grid interconnecting the three asynchronous ac grids and creating a hybrid ac/dc grid as shown in Figure 5-1. DC voltage droop control was implemented at all dc grid terminal converters. In this case, the total number of modes in the system increased to 123. In addition to the state variables associated with the generators and their controllers in each ac grid (41+19+19=79), the states in the hybrid ac/dc system include 44 state variables associated with the phase locked loops (PLL), converters and converters controllers. Figure 5-2 shows the position of eigenvalues of the individual grids and the hybrid ac/dc grid on the same s-plane.

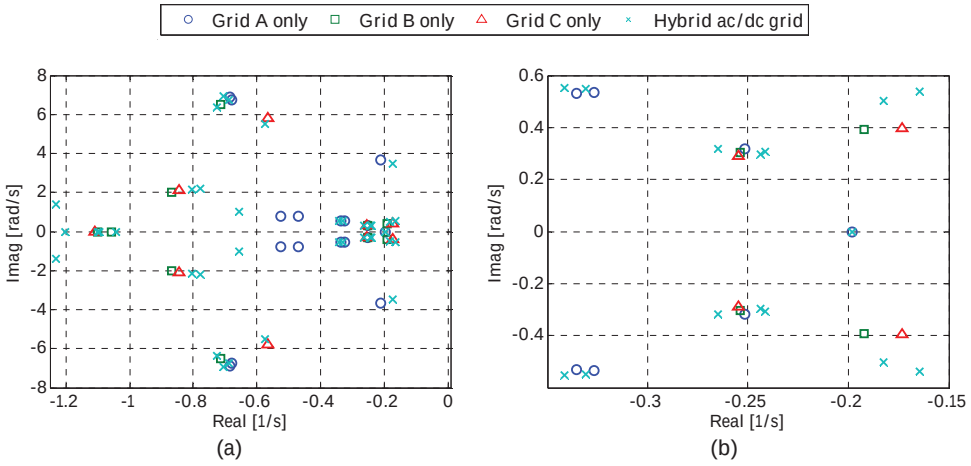

Figure 5-2 : Eigenvalues for individual and hybrid ac/dc grids (a) real part higher than -1.2 and (b) zoomed view

In general, the modes in the hybrid ac/dc system are a mere combination of the modes in the individual ac grids, and the additional modes that are related to the dc grid, converters and their controllers. It can be seen from Figure 5-2 that most of the ac grid modes of the hybrid ac/dc system are in the vicinity of the modes of the individual ac grids. Their position did not change significantly except for the two oscillatory Grid A modes (with a real part between -0.6 and -0.4), which have shifted to the left to a new position and now have real part around -0.7 and -1.2. The least damped modes, with damping ratio less than 15%, in the hybrid ac/dc system are presented in Table 5-3. It can be observed from comparing Table 5-2 and Table 5-3 that there is a change in the position of the eigenvalues after the addition of the dc grid but not to the extent where the stability of the grid was affected significantly.

Table 5-3 : Poorly damped modes in hybrid ac/dc grid with dc droop control in MTDC converters

Name	Eigenvalue	f [Hz]	ζ [%]	Dominant States
λ_{A1}	-0.17 ± j3.46	0.55	5.02	δ_{A1}, $\Delta\omega_{A3}$, δ_{A2}, $\Delta\omega_{A4}$, $\Delta\omega_{A1}$
λ_{A2}	-0.70 ± j6.94	1.10	10.09	δ_{A4}, $\Delta\omega_{A4}$, $\Delta\omega_{A3}$, δ_{A2}, E'_{dA4}
λ_{A3}	-0.69 ± j6.74	1.07	10.17	δ_{A2}, $\Delta\omega_{A2}$, $\Delta\omega_{A1}$, δ_{A1}, E'_{dA2}
λ_{B}	-0.73 ± j6.36	1.01	11.35	δ_{B6}, $\Delta\omega_{B5}$, $\Delta\omega_{B6}$, E'_{dB6}, E''_{dB6}
λ_{C}	-0.58 ± j5.53	0.88	10.36	δ_{C8}, $\Delta\omega_{C8}$, $\Delta\omega_{C7}$, E'_{dC8}, E''_{dC8}

This implies that the ac grids' stability remained the same for converter and generator controller settings used. Similar conclusions were drawn for a case where the dc grid is operated in a master-slave type of control mode. It is important to highlight that this conclusion is only valid for the case studied here. For different controller settings or grid set up, undesired interactions might occur between converter and generator the controllers. This is addressed in Chapter 7.

5.2. Mode shapes as a measure of dynamic interaction

If $\boldsymbol{\phi}_i$ is a right eigenvector of state matrix $\mathbf{A}$ associated with the eigenvalue λ_i, then its elements indicate the relative activity of state variables when the i^{th} mode is excited. For example, the degree of activity of the state variable x_k in the i^{th} mode is given by the magnitude of the k^{th} element of the right eigenvector $\boldsymbol{\phi}_i$, i.e. $|\phi_{ki}|$. However, the numerical values of $|\phi_{ki}|$ depend on scaling and units of the associated state variables e.g. speed in pu and rotor angle in rad. Therefore, relative amplitudes and phases of elements of the right eigenvectors associated with similar state variables are used to analyze modal responses. For example, for an electromechanical mode, λ_h, the elements in the right eigenvector corresponding to speed state variables, $\phi_{\Delta\omega,h}$, of all generators are selected to reveal the speed mode shape. Their relative amplitudes or mode shapes are computed as:

$$\frac{\left[\left|\phi_{\Delta\omega_1 h}\right| \quad \left|\phi_{\Delta\omega_2 h}\right| \quad \cdots \quad \left|\phi_{\Delta\omega_g h}\right| \quad \cdots \quad \left|\phi_{\Delta\omega_n h}\right|\right]}{\left|\phi_{\Delta\omega_g h}\right|}, \; or$$

$$\left[\frac{\left|\phi_{\Delta\omega_1 h}\right|}{\left|\phi_{\Delta\omega_g h}\right|} \quad \frac{\left|\phi_{\Delta\omega_2 h}\right|}{\left|\phi_{\Delta\omega_g h}\right|} \quad \cdots \quad 1 \quad \cdots \quad \frac{\left|\phi_{\Delta\omega_n h}\right|}{\left|\phi_{\Delta\omega_g h}\right|}\right] \tag{5.1}$$

where $\phi_{\Delta\omega_g h}$ is the speed state associated $\boldsymbol{\phi}_h$ element with the largest magnitude. A large relative amplitude in (5.1) implies a significant involvement of the speed state variable in the electro-mechanical mode λ_h.

Hereinafter, as the discussion is only about mode shapes of speed state variables, speed state mode shapes are simply referred as mode shapes.

The relative phase between the mode shapes indicates how the machines swing relative to each other. For example, for the three poorly damped modes in Grid A listed in Table 5-2,

the mode shapes of the generators (Gen1-4) speed state variables are shown in Figure 5-3. The polar plot shows both the relative magnitudes and relative phases of the mode shapes.

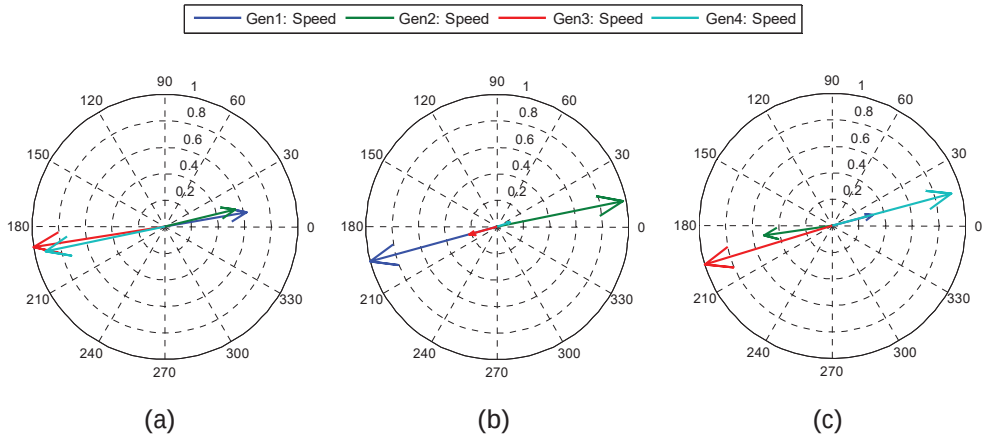

Figure 5-3 : Mode shapes of Grid A generator speed states for (a) Mode λ_{A1}, (b) Mode λ_{A2}, and (c) Mode λ_{A3}

The relative magnitudes of the speed state variables of Gen3&4 are large in Figure 5-3(a), while the relative magnitudes for Gen1&2 are around 60% of the mode shape magnitudes of Gen3&4. The relative phase between the mode shapes indicates that Gen1&2 oscillate together swinging against Gen3&4, which also oscillate together. In Figure 5-3(b), which shows mode shapes of speed state variables for mode λ_{A2}, Gen1&2 have high involvement in the mode and they are swinging against each other. Similarly, Figure 5-3(c) shows that Gen3&4 have significant involvement in the mode λ_{A3} and they oscillate against each other. The mode shapes of generator speed state variables for λ_B and λ_C are shown in Figure 5-4. They reveal that the generators in Grid B and Grid C have comparable involvement in the modes and that they oscillate against each other.

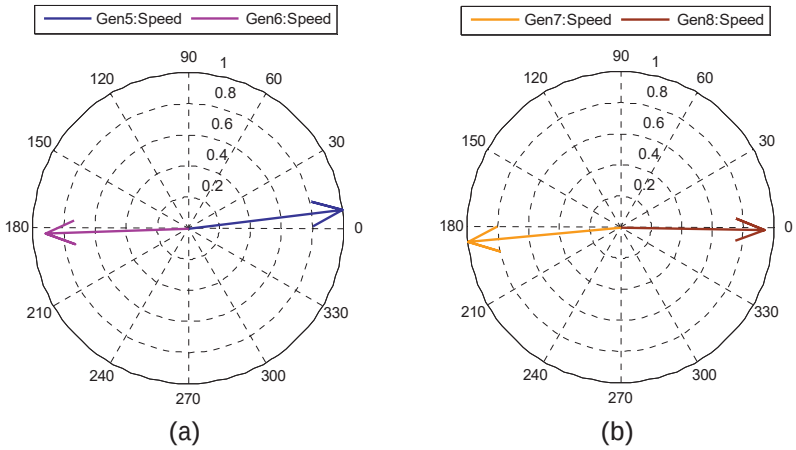

Figure 5-4 : Mode shapes (a) Grid B generator speed states for Mode λ_B, (b) Grid C generator speed states for λ_C

To corroborate the findings of the modal analysis, a time domain analysis was done using a non-linear model. In each ac grid, a complete short circuit fault was applied: one fault analysis at a time. The transient disturbance was applied on Bus8, Bus22, and Bus23 in Grid A, B, and C, respectively, at t=1s and lasted for 150ms. Figure 5-5(a) shows generators' speed response in Grid A when the fault is applied on Bus8. Figure 5-5(b) and Figure 5-5(c) show speed curves for generators in Grid B and Grid C, respectively, for a fault in the respective grids. In the transient period following the disturbance, the poorest damped modes in each grid are observable in the time domain response of the speeds. In addition, the time domain responses show that generators Gen1&2, Gen5, and Gen7 oscillate against Gen3&4, Gen6, and Gen8, respectively. This was also what was observed in the mode shape analysis.

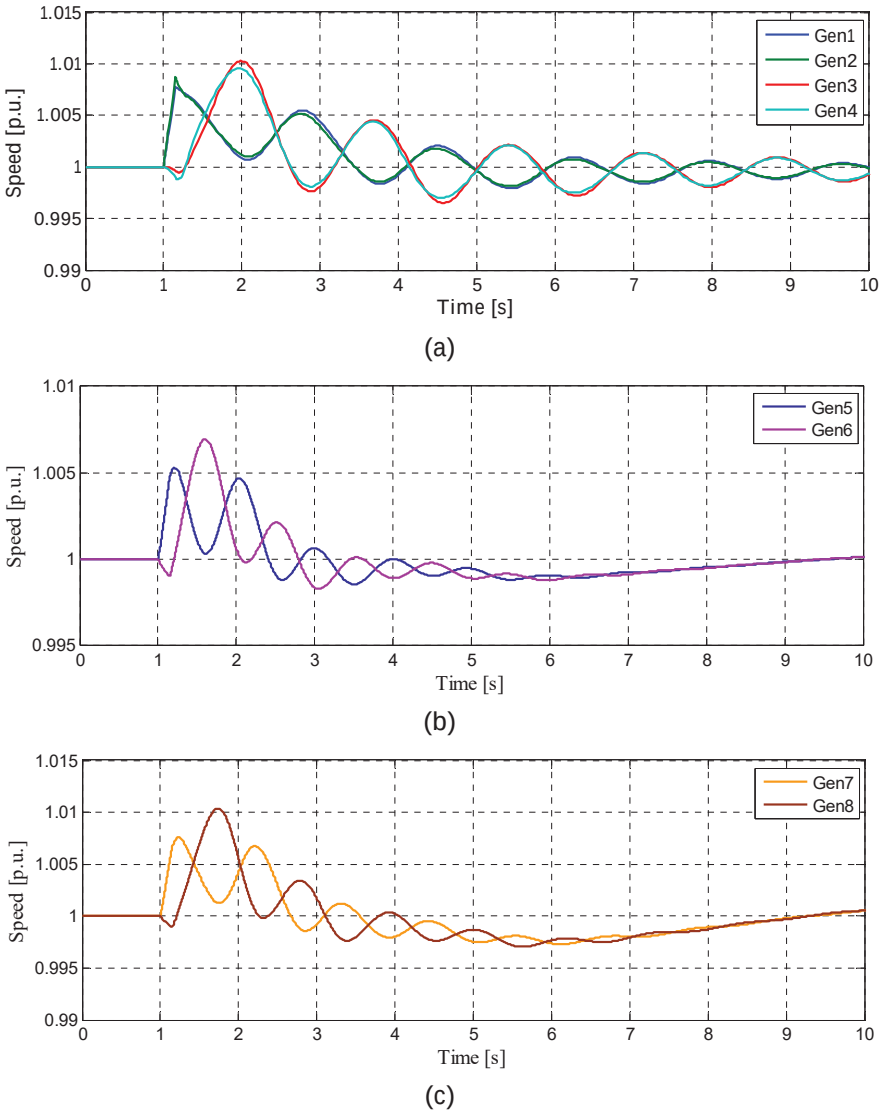

Figure 5-5: Transient speed response for large disturbances in (a) Grid A, (b) Grid B, and (c) Grid C

Another way of understanding mode shapes is using the modal observability concept introduced in Section 4.1.3. It was explained that a for a mode λ_h to be observed in output signal y_m, the product of m^{th} row of the output matrix and the h^{th} column of the right eigenvector matrix should be different from zero, i.e.

$$c'_{mh} = \mathbf{c}_m \boldsymbol{\phi}_h \neq 0 \tag{5.2}$$

where c'_{mh} measures the observability of a mode in the output y_m. If the output signal is selected to be a state variable, speed in this case, then the output row vector $\mathbf{c}_{\Delta\omega}$ will have zero elements except for the column corresponding to the speed state variable. Thus, the value of c'_{mh} will be the same as the speed state associated element of $\boldsymbol{\phi}_h$. Thus, mode shapes can serve as a measure of observability of a mode in a state variable. Non-zero elements of $\boldsymbol{\phi}_h$ indicate that λ_h is observable in the corresponding state variables and zero elements of $\boldsymbol{\phi}_h$ indicate that λ_h is not observable in the corresponding state variables. Higher magnitudes imply higher observability and vice versa.

5.3. AC-AC Interaction Identification

This section identifies electromechanical interactions between generators located in asynchronous grids, which are connected through an MTDC grid. Mode shapes of generators' speed state variables are used for identification of small-signal interaction, and time domain analysis is used support the findings.

As explained earlier, the magnitudes of mode shapes show the relative activity of state variables when a particular mode is excited, while their relative phases show how the state variables are interacting with each other. If the relative magnitude of the mode shape is high, then it implies a significant involvement of the state variable in the mode. On the other hand, if the relative magnitude of the mode shape is low, then the state variable has low involvement in the mode. If mode shape is zero, then the state variable is not involved in the mode. Using the concept of observability, a mode is observable in a state variable if it has a high mode shape magnitude for the state variable. If the magnitude of a mode shape is low or zero for a state variable, then the mode is weakly observable or not observable in the state variable, respectively.

Table 5-4 presents mode shapes of speed state variables for the poorly damped electromechanical modes in the hybrid ac/dc test system (listed in Table 5-3). Eigenvalues λ_A, λ_B and λ_C have the highest observabilities in speed state variables of generators found in grids where the modes originate from, i.e. Grid A, Grid B, and Grid C, respectively. For example, eigenvalues λ_{A1} is most observable in speed state variables of Gen3. The next highest observability for the mode is in Gen4, Gen1 and Gen2, respectively. Albeit low magnitude, the mode is also observable in generators 5 to 8. These are generators located

in distant ac grids that are connected to Grid A via MTDC only. Despite the absence of a synchronous connection between the grids, a dominant mode in Grid A is observable in the speed state variables of generators found in Grid B and Grid C. This shows that the MTDC grid leads to a weak dynamic coupling between the asynchronous ac grids. The mode shapes of the other electro-mechanical modes in Grid A are also non-zero for Gen5-8. Furthermore, the poorly damped modes in other grids, i.e. λ_B and λ_C, exhibit similar characteristics. These modes are dominant modes in Grid B and Grid C with the highest observability in generators' state variables in these grids. However small, they are also observable in the other asynchronous ac grid where the modes did not originate.

Table 5-4 : Mode shapes of generator speed states for electromechanical modes in the hybrid ac/dc system with VSC based MTDC grid

	State	AC grid	λ_{A1}	λ_{A2}	λ_{A3}	λ_B	λ_C
Gen1: speed	$\Delta\omega_{A1}$	A	0.172	0.125	0.878	0.002	0.002
Gen2: speed	$\Delta\omega_{A2}$	A	0.079	0.066	1	0.001	0
Gen3: speed	$\Delta\omega_{A3}$	A	1	0.79	0.187	0.002	0.002
Gen4: speed	$\Delta\omega_{A4}$	A	0.982	1	0.153	0.001	0
Gen5: speed	$\Delta\omega_{B5}$	B	0.009	0.013	0.011	0.971	0.001
Gen6: speed	$\Delta\omega_{B6}$	B	0.013	0.007	0.007	1	0.006
Gen7: speed	$\Delta\omega_{B7}$	C	0.008	0.01	0.006	0.005	0.84
Gen8: speed	$\Delta\omega_{B8}$	C	0.016	0.002	0.002	0.002	1

From the mode shapes of the electromechanical modes presented in Table 5-4, it can be observed that in the hybrid system all generator state variables are involved in each mode, though their degree of involvement varies. Therefore, the observability of a mode, which originally belonged to one grid, in a non-synchronously connected ac grids indicates the existence of an ac-ac interaction or a dynamic coupling between the asynchronous power systems. The physical interpretation of this phenomenon is that generators located in asynchronous grids interconnected with an MTDC grid oscillate against each other. Inter-area oscillation refers to oscillation of groups of generators in one area against groups of generators in another area. By the same token, the observed phenomena can be understood as inter-grid oscillation.

Time domain simulation of the test system for a fault in Grid A supports the findings of the modal analysis. A short circuit fault was applied for 10ms on Bus 8. The fault causes a small disturbance in Grid A and excites all the modes in the system. However, as λ_{A1} is the poorest damped mode in Grid A, it has the longest damping time constant. Therefore, this

mode will be observable in the speed of the generators. The relative phase of the mode shapes for λ_{A1} in Table 5-5 indicates that Gen1&2 oscillate against Gen3&4. Furthermore, the generators in Grid B (Gen5&6) and Grid C (Gen7&8) oscillate together at almost 90° phase shift with respect to the oscillations of generators in Grid A.

Table 5-5 : Mode shape magnitude and phase for λ_{A1}

	State	AC grid	λ_{A1}	
			Magnitude	*Angle [deg]*
Gen1: speed	$\Delta\omega_{A1}$	A	0.172	7.8
Gen2: speed	$\Delta\omega_{A2}$	A	0.079	20.0
Gen3: speed	$\Delta\omega_{A3}$	A	1	-167.0
Gen4: speed	$\Delta\omega_{A4}$	A	0.982	-165.0
Gen5: speed	$\Delta\omega_{B5}$	B	0.009	89.9
Gen6: speed	$\Delta\omega_{B6}$	B	0.013	91.4
Gen7: speed	$\Delta\omega_{B7}$	C	0.008	87.1
Gen8: speed	$\Delta\omega_{B8}$	C	0.016	88.0

Figure 5-6 shows the response of Gen1-4 found in Grid A for the small disturbance in the grid. The frequency of oscillation of the generators' speed curves is 0.55 Hz, which is the same frequency as the poorest damped mode in Grid A (λ_{A1}).

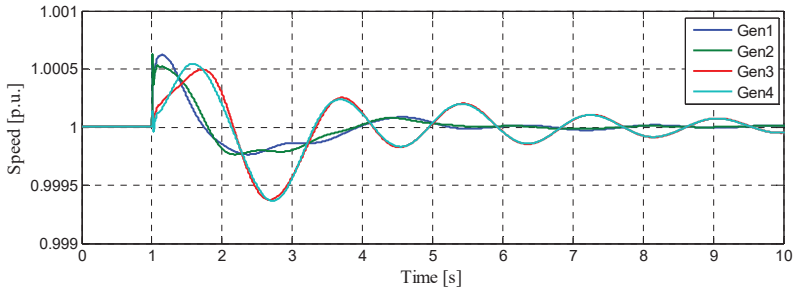

Figure 5-6 : Transient response of generators in Grid A for a small disturbance in the grid

Even though its effect is most noticeable in Grid A, the disturbance is also observed in the other asynchronous grids in the test system. It should be highlighted here that the propagation of the disturbance was not due to current limits in the inner converter controllers, as these limits were not reached. Figure 5-7 shows the speed curves for the generators in the asynchronous grids where the fault did not occur, i.e. Grid B and Grid C. A closer look at the curves shows that the speeds of the generators oscillate with a

frequency of 0.55 Hz. Note that the frequency of the poorly damped modes in Grid B and C are 1.01 Hz and 0.88 Hz (Table 5-3). In addition, Grid B and C generators in Figure 5-7 are oscillating together, not against each other as in Figure 5-5. Thus, in Figure 5-7 the dominant mode in the generators' oscillation is λ_{A1}, which is the poorest damped mode in Grid A. This is also supported by the relative phase of the mode shapes of λ_{A1} in Table 5-5. The disturbance in Grid A has excited this mode, and as a result, it is observed in the generator speed oscillations throughout the hybrid ac/dc system. It should be noted that the magnitude of oscillations of speeds of Gen5&6 and Gen7&8 are very small. This is also seen from the small mode shape magnitudes in Table 5-5.

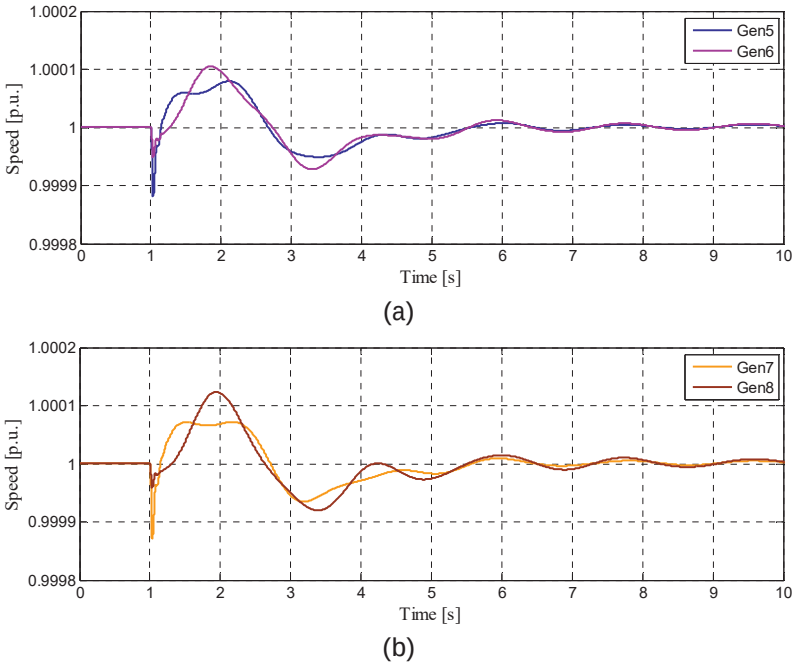

Figure 5-7: Transient response of generators in Grid B and Grid C for a small disturbance in Grid A

In the above analysis, the converters at the MTDC grid terminals were modelled as a 2-level VSC converters. The dc grid was changed to an MMC based MTDC, and a similar methodology as above was used to find speed mode shapes for the electromechanical modes in the new hybrid ac/dc grid. The results are presented in Table 5-6.

Table 5-6 : Mode shapes of generator speed states for electromechanical modes in the hybrid ac/dc system with MMC based MTDC grid

	State	AC grid	λ_{A1}	λ_{A2}	λ_{A3}	λ_{B}	λ_{C}
Gen1: speed	$\Delta\omega_{A1}$	A	0.172	0.127	0.878	0.001	0.002
Gen2: speed	$\Delta\omega_{A2}$	A	0.079	0.066	1	0.001	0
Gen3: speed	$\Delta\omega_{A3}$	A	1	0.792	0.189	0.002	0.001
Gen4: speed	$\Delta\omega_{A4}$	A	0.982	1	0.155	0.001	0
Gen5: speed	$\Delta\omega_{B5}$	B	0.012	0.011	0.012	0.91	0
Gen6: speed	$\Delta\omega_{B6}$	B	0.016	0.005	0.007	1	0.001
Gen7: speed	$\Delta\omega_{B7}$	C	0.011	0.01	0.007	0.001	0.782
Gen8: speed	$\Delta\omega_{B8}$	C	0.021	0.002	0.002	0	1

By comparing the relative mode shape magnitudes of the electromechanical modes in Table 5-4 and Table 5-6, it can be concluded that a weak dynamic coupling between the asynchronous ac systems exists and the degree of coupling does not change significantly when the type of MTDC grid terminal converter changes.

The next section evaluates the sensitivity of the mode shape magnitudes for different scenarios. Since the magnitudes of modes shapes are fairly similar for 2-level based and MMC based MTDC grids, the sensitivity analysis is carried out only for the 2-level VSC based MTDC grids.

5.4. Sensitivity to converter controller strategy and parameter settings

In the previous section, dynamic interactions between asynchronous ac grids interconnected via MTDC were identified using modal and time domain analyses. This section investigates how the level of dynamic interactions between asynchronous ac grids connected through a dc grid varies for different dc grid operation modes and terminal converter settings. In each case, speed mode shapes of poorly damped eigenvalues in the hybrid ac/dc system are analyzed in detail to identify the interactions. The sensitivity analysis hereinafter considers only one mode from each grid, i.e. λ_{A1}, λ_{B} and λ_{C}, as the results and conclusions drawn are also valid for the other two electromechanical modes (λ_{A2} and λ_{A3}) in Grid A. Therefore, λ_{A2} and λ_{A3} are not included in analyses and discussions further.

5.4.1. Master slave

A master-slave control strategy is implemented for dc grid operation. In this dc grid operation mode, one terminal controls dc grid voltage and the rest of the terminals in the

grid control active power flow at their ac grid connection points. Thus, in the study case considered here, converters at Terminals #1, #2, and Terminal #4 operate in constant power mode while the converter at Terminal #3, which is connected to Grid B, operates in constant dc voltage control mode.

As previously mentioned, the positions of the eigenvalues on the complex plane do not change significantly when dc voltage droop or master-slave control strategies are used. Thus, the least damped eigenvalues of the test system remain the same under both types of dc grid controls modes. However, the interaction between the asynchronous ac grids is different under the different MTDC control strategies. When a master-slave control strategy is used, the poorly damped modes are most observable in the grids they originate from, but their second highest observability is in Grid B, which is the ac grid connected to the master controller (the dc voltage controlling terminal); see Table 5-7. Meanwhile, the modes have zero observability in distant (asynchronously connected) ac grids behind a constant power controlled terminal.

Table 5-7: Mode shapes of poorly damped modes with master-slave control mode implemented in MTDC terminals

State variables		**AC grid**	λ_{A1}	λ_{B}	λ_{C}
Gen1: speed	$\Delta\omega_{A1}$	A	0.171	0	0
Gen2: speed	$\Delta\omega_{A2}$	A	0.077	0	0
Gen3: speed	$\Delta\omega_{A3}$	A	1	0	0
Gen4: speed	$\Delta\omega_{A4}$	A	0.981	0	0
Gen5: speed	$\Delta\omega_{B5}$	B	0.038	0.962	0.004
Gen6: speed	$\Delta\omega_{B6}$	B	0.057	1	0.026
Gen7: speed	$\Delta\omega_{B7}$	C	0	0	0.84
Gen8: speed	$\Delta\omega_{B8}$	C	0	0	1

Comparing the mode shape magnitudes of λ_{A1} for the two MTDC control methods evaluated (Table 5-4 and Table 5-7), it can be seen that under master-slave control mode the mode is highly observable in state variables of generators found in Grid A. The mode is also observable in state variables of generators in Grid B but not in Grid C. In the case where dc voltage droop control is used, Table 5-4, the magnitude of modes shapes related to Gen5-8 are generally low and similar in scale. On the other hand, when master-slave control mode is used, Table 5-7, the magnitude of the mode shapes for Gen5&6 have larger magnitudes. In addition, the magnitude of the mode shapes for Gen7&8, in the case of master-slave MTDC control, is zero: indicating that no activity is measured in these state

when mode λ_{A1} is excited. Similarly, the relative magnitude of mode shape of λ_C is largest in Grid C, where the modes dominates, but at the same time have small magnitudes for speed states in Grid B. The mode is not observable in the generator states found in Grid A. An interesting observation is that only speed states of Gen5&6 are involved in λ_B and the mode is not observable in neither Grid A nor Grid C. Hence, it can be concluded from the findings in Table 5-7 that when the dc grid is operating in master-slave control strategy, there is interaction between asynchronous grids connected to active power and dc voltage controlling terminals. However, this interaction is only one-way, meaning the modes of ac grids behind active power controlling terminals are observable in the ac grid behind the dc voltage-controlling terminal, but the reverse is not true. Moreover, there is no interaction between grids behind active power controlling terminals.

5.4.2. Frequency support

If primary frequency reserves are to be shared among ac grids connected through an MTDC grid, then frequency droop control can be used in addition to dc voltage droop. The decentralized control scheme uses droop controller on the frequency error to modify active power flow at a terminal converter of an MTDC (see Figure 3-12 (a)). Then, ac grids connected to the MTDC respond to remove power imbalance resulting from the frequency droop controller and regulate MTDC voltage and indirectly contribute to frequency regulation.

Mode shapes of poorly damped electromechanical modes of the test system with frequency and dc voltage droop control mode of operation of the dc grid are presented in Table 5-8. For the modes studied, the observability of the modes in distant ac grids is an order of magnitude higher when frequency droop is used than when only dc voltage droop is used (Table 5-4). This means that using frequency droop in addition to dc voltage droop for frequency reserve sharing increases the dynamic coupling of asynchronous grids connected through an MTDC.

Table 5-8 : Observability of studied modes for frequency droop control in MTDC

	State	AC grid	λ_{A1}	λ_{B}	λ_{C}
Gen1: speed	$\Delta\omega_{A1}$	A	0.17	0.02	0.011
Gen2: speed	$\Delta\omega_{A2}$	A	0.083	0.011	0.002
Gen3: speed	$\Delta\omega_{A3}$	A	1	0.017	0.014
Gen4: speed	$\Delta\omega_{A4}$	A	0.981	0.007	0.003
Gen5: speed	$\Delta\omega_{B5}$	B	0.039	0.971	0.007
Gen6: speed	$\Delta\omega_{B6}$	B	0.057	1	0.04
Gen7: speed	$\Delta\omega_{B7}$	C	0.04	0.04	0.842
Gen8: speed	$\Delta\omega_{B8}$	C	0.078	0.018	1

5.4.3. Controller Tuning

To investigate the effect the tuning of converter controllers has on the interaction, and the extent to which this is translated into changes of the modes shapes, the bandwidth of the outer control loop of the 2-level VSC converters, i.e. active and reactive controllers (see Figure 3-10), was changed. The results of the modal analysis in Table 5-4 are used as a reference base case where the bandwidth of the outer control loop is 10 times lower than the bandwidth of the inner current control loop. Two cases of outer control bandwidth values were considered. In the first case, the bandwidth was set to 5 times slower than the inner current control loop, which made the converter respond faster compared to the base case. In the second case, the bandwidth was set to 20 times slower than the inner current control loop, which made the response of the converter slower than the base case. The mode shapes of the poorly damped electromechanical modes were calculated for the two cases, and their magnitude changes compared to the base case are presented in Table 5-9. The relative change in mode shape magnitudes are presented in percentage.

Table 5-9: Effect of converter parameter variation on mode shapes of poorly damped modes

	State	AC grid	λ_{A1}		λ_B		λ_C	
			Faster	*Slower*	*Faster*	*Slower*	*Faster*	*Slower*
			[%]	*[%]*	*[%]*	*[%]*	*[%]*	*[%]*
Gen1: speed	$\Delta\omega_{A1}$	A	0	1	-50	150	-50	50
Gen2: speed	$\Delta\omega_{A2}$	A	0	1	0	200	-	-
Gen3: speed	$\Delta\omega_{A3}$	A	0	0	-50	100	-50	100
Gen4: speed	$\Delta\omega_{A4}$	A	0	0	-100	100	-	-
Gen5: speed	$\Delta\omega_{B5}$	B	-56	89	0	1	-100	100
Gen6: speed	$\Delta\omega_{B6}$	B	-46	92	0	0	-50	100
Gen7: speed	$\Delta\omega_{B7}$	C	-50	100	-60	80	0	1
Gen8: speed	$\Delta\omega_{B8}$	C	-50	100	-50	100	0	0

The change in mode shapes is small for generators in the grid where the modes originate from. The largest relative changes occur in mode shapes for the generator speeds found in remote MTDC connected ac grids. Generally, compared to the base case, the observability of the modes in the generators' state variables decreases in Case 1 (faster response) and increases in Case 2 (slower response). This means that when the converter response becomes faster, the interaction between the asynchronous grids is reduced and vice versa.

5.4.4. Resonant conditions

This section analyses the extent of interaction between generators in asynchronous grids when the dominant modes in different grids have similar damped frequency. The test power system shown in Figure 5-1 is used again. The converters at the dc grid terminals operate in dc voltage droop control and power flows at the terminals remain the same. The focus is on the dynamic coupling between Grid B and Grid C. Poorly damped modes from the grids are shown in Table 5-10.

Table 5-10 : Electromechanical modes in Grid B&C with lower damping ratios

Name	Eigenvalue	f [Hz]	ζ [%]	Dominant States
λ_B	-0.73 ± j6.36	1.01	11.35	$\delta_{B6}, \Delta\omega_{B5}, \Delta\omega_{B6}, E'_{dB6}, E''_{dB6}$
λ_C	-0.58 ± j5.53	0.88	10.36	$\delta_{C8}, \Delta\omega_{C8}, \Delta\omega_{C7}, E'_{dC8}, E''_{dC8}$

The inertia constant parameter of Gen7&8 in Grid C was varied between H=3.8 s and H=6.8 s. The change in H parameter was used to move the position of dominant mode in the grid and find a position where the damping frequencies of the dominant modes in Grid

B and Grid C are similar. Table 5-11 shows the change in the dominant mode for five values of inertia time constants. For H=4.9 s, the damped frequency of the dominant mode in Grid C, i.e. 1.02 Hz, is close to that of the frequency of the dominant mode in Grid B, i.e. 1.01 Hz.

Table 5-11 : Dominant mode in Grid C for different values of inertia time constants for Gen7&8

H [s]	λ_C	f**[Hz]**
3.8	$-0.66 \pm j\,7.31$	1.16
4.25	$-0.64 \pm j\,6.86$	1.09
4.9	$-0.62 \pm j\,6.39$	1.02
5.7	$-0.59 \pm j\,5.89$	0.94
6.8	$-0.57 \pm j\,5.34$	0.85

Figure 5-8 traces the movement of λ_C (the square marks) on the complex plane for the different inertia constants considered. In addition, the original positions of λ_B and λ_C are indicated by 'o' and 'x' marks, respectively, in the figure. The position λ_B of does not change when H is changed in Gen7&8.

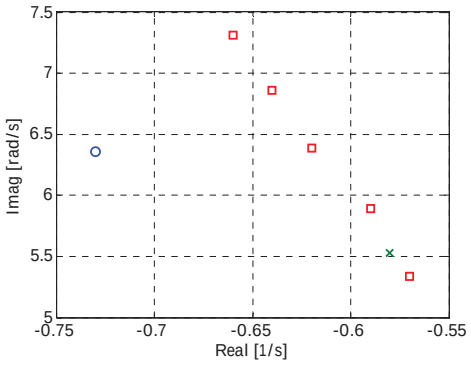

Figure 5-8 : λ_B ('o' marker) and λ_C ('x' and rectangular marker) for different H values of Gen7&8

Mode shapes of λ_C was calculated for all cases of the inertia time constants considered. The magnitudes of the mode shapes related to the speed state variable of all generators' in the hybrid ac/dc system are shown in Table 5-12.

Table 5-12 : Mode shape of λ_C for different values of inertia time constant in Gen 7&8

	State	AC grid	H [s]				
			3.8	*4.25*	*4.9*	*5.7*	*6.8*
Gen1: speed	$\Delta\omega_{A1}$	A	0.001	0.008	0.004	0.002	0.002
Gen2: speed	$\Delta\omega_{A2}$	A	0.003	0.011	0.002	0	0
Gen3: speed	$\Delta\omega_{A3}$	A	0.002	0.009	0.003	0.002	0.002
Gen4: speed	$\Delta\omega_{A4}$	A	0.005	0.01	0.002	0	0.001
Gen5: speed	$\Delta\omega_{B5}$	B	0.005	0.008	0.027	0.004	0
Gen6: speed	$\Delta\omega_{B6}$	B	0.002	0.005	0.028	0.009	0.006
Gen7: speed	$\Delta\omega_{B7}$	C	0.89	0.88	0.87	0.85	0.83
Gen8: speed	$\Delta\omega_{B8}$	C	1	1	1	1	1

Focusing on the observability of λ_C in the speed state variables of generators in Grid B, it can be seen that the level of interaction is highest when the dominant modes both in Grid B and Grid C have the same damped frequency, i.e. H=4.9 s. This is clearly shown in the plot of mode shapes of λ_C for Gen5&6 speed state variables in Figure 5-9.

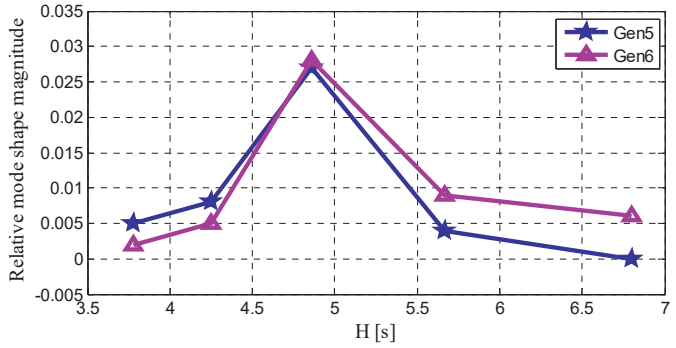

Figure 5-9 : Observability of λ_C in speed state of generators in Grid B for different H values

The change of inertia constant of generators in Grid C has no effect on the poorly damped mode in Grid B. The mode remains at -0.73 ± j6.36 for all H values evaluated. However, the observability of the mode in generators speed state variables in Grid C changes. Table 5-13 shows the mode shape of λ_B for all speed state variables. Again, the observability of the mode in speed state variables of the generators in Grid C is highest for H=4.9 s.

Table 5-13 : Mode shape of dominant mode in Grid B for different values of inertia time constant in Gen 7&8

	State	AC grid	H [s]				
			3.8	*4.25*	*4.9*	*5.7*	*6.8*
Gen1: speed	$\Delta\omega_{A1}$	A	0.002	0.002	0.002	0.002	0.002
Gen2: speed	$\Delta\omega_{A2}$	A	0.001	0.001	0.001	0.001	0.001
Gen3: speed	$\Delta\omega_{A3}$	A	0.002	0.002	0.002	0.002	0.002
Gen4: speed	$\Delta\omega_{A4}$	A	0.001	0.001	0.001	0.001	0.001
Gen5: speed	$\Delta\omega_{B5}$	B	0.971	0.971	0.971	0.971	0.971
Gen6: speed	$\Delta\omega_{B6}$	B	1	1	1	1	1
Gen7: speed	$\Delta\omega_{B7}$	C	0.002	0.006	0.03	0.008	0.004
Gen8: speed	$\Delta\omega_{B8}$	C	0.008	0.011	0.035	0.005	0.001

Figure 5-10 shows the relative magnitude of mode shapes of λ_B for Gen7&8 speed state variables. It is clear from the plot that the observability of the mode in the speed state variables is highest when the damped frequency of the dominant modes in the two systems matches for H=4.9 s. This indicates higher interaction level compared to the other studied cases.

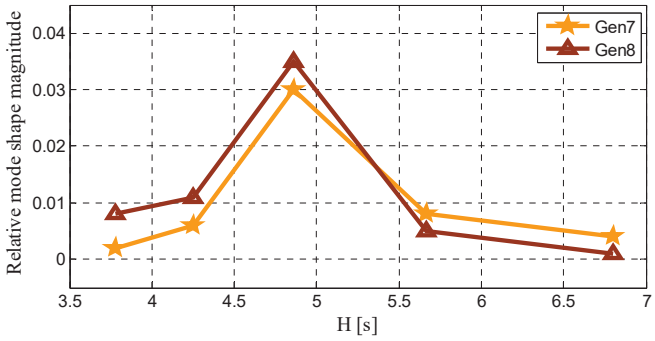

Figure 5-10 : Observability of dominant mode in Grid B in speed state of generators in Grid C for different H values

The analysis in this sub-section showed that the interaction between ac grids in hybrid ac/dc power systems is influenced by the frequency of the dominant modes in each grid. More specifically, it was found that the interaction increases when the dominant modes in each ac grid have similar damped frequency.

5.5. Participation factor based interaction analysis

The analysis in this subsection uses a participation factor based interaction mode identification method proposed in [96]. In the method, a system is divided into smaller subsystems, and modes with participation from more than one subsystems are identified as interaction modes. This means a hybrid ac/dc grid can be divided into ac subsystem, dc subsystem and converter subsystem. A mode that has a participation from two or more subsystems, for example, an ac sub system and a converter subsystem, represents a dynamic interaction between the subsystems. Thus, modes with a certain degree of participation from more than one subsystem are labeled as ac-to-converter, ac-to-dc, converter-to-converter, etc. interaction modes.

A parameter $\eta_{\alpha i}$ is defined in [96] as a measure of the cumulative participation of subsystem α in mode λ_i. Mathematically, $\eta_{\alpha i}$ is defined as in (5.3). It is the ratio of L_1-norm of the vector of participation factors of state variables of subsystem α in mode λ_i ($p_{\alpha,i}$) to the L_1-norm of the vector of participation factors of all state variables in mode λ_i (p_i). In essence, the measure calculates the degree of participation of each subsystem (a group of state variables) in a mode, while a participation factor measures the participation of a state variable in a mode.

$$\eta_{\alpha i} = \frac{\|p_{\alpha i}\|}{\|p_i\|} \tag{5.3}$$

Modes where more than one subsystem participate are classified as interaction modes. For a threshold value of χ, an interaction mode j is a mode where $\eta_{\alpha j} > \chi$ for at least two subsystems.

The study system used for the analysis in this subsection is shown in Figure 5-11. The system has three asynchronous ac grids connected through a three terminal MMC based MTDC grid. All three ac grids contain multiple generators, and represent large power systems. System topology and data for Grid A, Grid B, and Grid C are taken from benchmark systems given in [72], [71], and [97], respectively. The dc grid is a symmetric monopolar system with ±200 kV voltage rating. The multiple π-section with multiple parallel resistance and inductance branches model, presented in Section 3.2.2, is used to model dc cables. As a compromise between model complexity and accuracy, three π-sections with three-parallel branches was chosen. Initial dc grid load flow values are presented in Table 5-14.

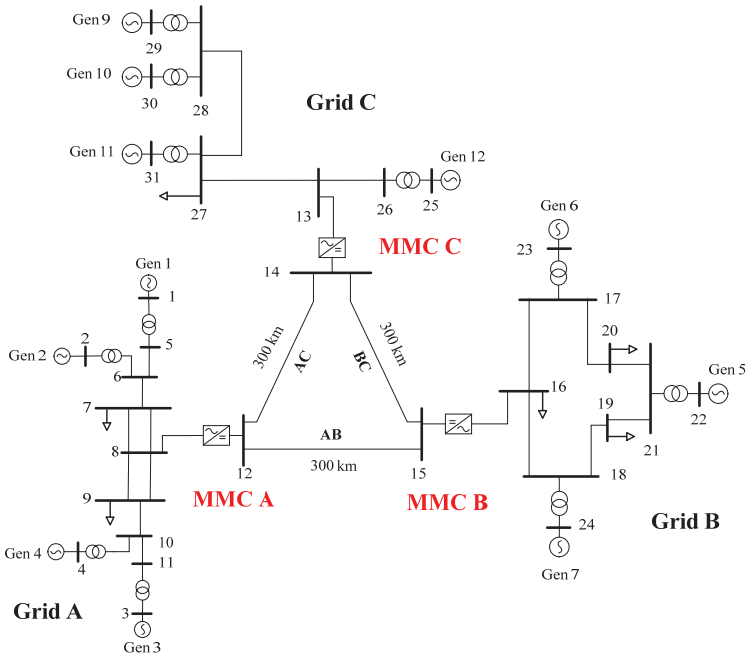

Figure 5-11: Hybrid ac/dc study system

Table 5-14 : Initial dc grid load flow

Terminal	P [MW]	Q [MVAr]	V_{dc} [kV]	ρ_{dc} [%]
A	-300.8	0	388	4
B	397.3	0	385.6	4
C	-100.9	0	387.2	4

Following the method, the study system was divided into seven subsystems: three ac grid subsystems (Grid A, Grid B, Grid C), three converter subsystems (MMC A, MMC B, MMC C), and a dc grid subsystem. Each subsystem is formed by grouping the appropriate state variables. For example, an ac grid subsystem is made up of all state variables associated with generators, excitation systems and turbines/governors. Similarly, state variables associated with a PLL, an MMC converter and its controllers make up a converter subsystem. All three dc cables, i.e. cables AB, AC and BC, are grouped into one subsystem and make up the dc grid subsystem. Equation (5.4) lists the state variables that make up ac, converter and dc subsystems.

$$
\begin{aligned}
\mathbf{x}_{ac} &= [\delta \quad \Delta\omega \quad E_q^{'} \quad E_d^{'} \quad E_q^{''} \quad E_d^{''} \\
&\quad E_{fd} \quad x_{AVR1} \quad x_{AVR2} \quad x_{GOV1} \quad x_{GOV2} \quad x_{GOV3}]^T \\
\mathbf{x}_{MMC} &= [i_{g,d} \quad i_{g,q} \quad N_d \quad N_q \quad M_d \quad M_q \quad v_{sd} \quad v_{sq} \\
&\quad v_{dc} \quad i_{c,z} \quad \xi_z \quad w_{\Sigma} \quad \kappa_{\Sigma} \quad \theta_{pll} \quad x_{pll}]^T \\
\mathbf{x}_{dc} &= [i_{dc11} \quad i_{dc12} \quad i_{dc33} \quad i_{dc21} \quad i_{dc22} \quad i_{dc23} \\
&\quad i_{dc13} \quad i_{dc23} \quad i_{dc33} \quad v_{dc2} \quad v_{dc3}]^T
\end{aligned}
\tag{5.4}
$$

where the subscripts d and q indicate generator/converter d and q reference frame axes, and the variables indicate:

E'	Transient voltage
E''	Sub-transient voltage
E_{fd}	Field excitation voltages
i_{cz}	Zero-sequence circulating current
i_g	Current flowing from converter into grid
M	State variable associated with the PI in converter outer controller
N	State variable associated with the PI in converter inner current controller
v_{dc}	DC voltage
v_g	PCC voltage
v_s	Internal VSC voltage
$w_{\Sigma,z}$	Zero-sequence energy-sum
x_{AVR}	State variable associated with AVR
x_{GOV}	State variables associated with turbine/governor
x_{pll}	State variable associated with PI controller of the PLL
δ	Rotor angle
$\Delta\omega$	Rotor speed deviation from synchronous speed
κ	State variable associated with PI in zero-sequence energy controller
θ_{pll}	PLL estimated PCC voltage angle
ξ	State variable associated with PI in zero-sequence circulating current controller

This participation factor based method gives a good overview of interaction modes. However, it has some limitations. It can be misleading if subsystems are not selected properly. Furthermore, when the number of state variables in each subsystem is not comparable, e.g. the dc cable subsystem has 33 state variables in contrast to the converter subsystem that has 15 state variables, adding participation factors can result in misleading conclusions. In addition, the method does not differentiate between modes, e.g. poorly damped modes and well damped modes, hence not all results might be important or relevant. Therefore, it is important to study further the interaction modes identified through the method to establish which controllers/components participate most and if

the modes could determine the stability of the entire system. It is mentioned in the discussions when these limitations are encountered. Otherwise, the method is an easy way to find subsystem interaction modes, and if an identified mode is critical, the method points out which subsystems can contribute to making the mode, thus the system, more stable.

Linear analysis result of the hybrid ac/dc study system carried out in MATLAB/Simulink show that the system has 183 total number of modes. Table 5-15 compares the total number of interaction modes involving a different number of subsystems for two cases of MMC converter control strategies; namely dc voltage droop and dc voltage droop with frequency droop. In the first case, Case 1, each converter is operating in dc voltage droop control mode with droop constant ρ_{dc}=4%. In the second case, Case 2, a frequency droop with a droop constant of ρ_f=6% is added to the outer MMC converter controller in addition to the dc voltage droop with ρ_{dc}=4%. The minimum cumulative participation (η) threshold is set to χ =10%. Therefore, modes that have participation from two or more subsystems with η>10% are regarded as interaction modes.

Table 5-15 : Total number of Interaction modes for different number of subsystems

Number of subsystems	**Case1 (ρ_{dc}=4%)**	**Case 2 (ρ_{dc}=4%+ ρ_f=6%)**
2	39	58
3	12	18

In general, there are more interaction modes in Case 2 than in Case 1. The number of interaction modes between any two subsystems is three times more than the number of interaction modes between any three subsystems. It should be mentioned that no interaction modes were found with participation from more than three subsystems. Comparing Case 1 and 2, it can be observed that the number of interaction modes increases when a frequency droop control is added to MTDC converter controllers for asynchronous systems frequency reserve sharing. This implies that when frequency droop control is used in addition to dc voltage droop control, the coupling between the different subsystems increases.

Table 5-15 only shows how many interaction modes exist and how many subsystems participate, but does not indicate which subsystems are participating in the interaction modes. In the following analysis, interaction modes are studied further focusing on ac-converter, ac-ac and converter subsystems interaction. No interaction modes were found

with participation from any of the ac grid subsystems and the cable subsystem. Therefore, ac-to-dc subsystem interaction is not studied. In addition, a suffix A, B or C is added in the subscript of each ac grid and converter state to indicate which subsystem the state belongs to. Likewise, a suffix AB, AC or BC is added to the subscript of each dc subsystem state variable to indicate which dc cable the state is associated with.

5.5.1. AC-Converter interaction modes

Hereinafter, ac-converter interaction modes are defined as modes with participation from an ac subsystem and a converter subsystem.

Figure 5-12 shows η factor for six interaction modes with at least 10% cumulative participation from Grid A and MMC A subsystems. Except for mode λ_{84}, all other identified interaction modes have participation almost exclusively from subsystems Grid A and MMC A.

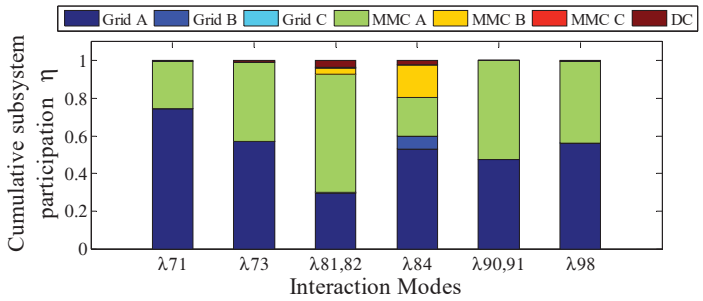

Figure 5-12 : Interaction modes between Grid A and MMC A subsystems

Further analysis of the interaction modes shows, sub transient voltage states of generators in Grid A and q-axis PI controller states of MMC A participate most to these modes, see Table 5-16. Furthermore, the identified interaction modes are well damped and are located far from the imaginary axis.

Table 5-16 : Dominant state variables interaction modes between Grid A and MMC A

Mode #	Eigenvalue	ζ [%]	Dominant states
λ_{71}	-36.5	100	E''_{qA2}, N_{qA}, E''_{qA1}, M_{qA}, I_{gqA}
λ_{73}	-35.61	100	E''_{qA1}, N_{qA}, M_{qA}, I_{gqA}, E''_{dA2}
$\lambda_{81,82}$	-29.77 ± j1.91	99.8	N_{qA}, E''_{dA2}, ξA, M_{dA}, I_{gqA}
λ_{84}	-26.86	100	E''_{dA1}, E''_{dA2}, ξA, M_{dA}, M_{dB}
$\lambda_{90,91}$	-23.24 ± j0.12	99.99	M_{dA}, E''_{dA1}, E''_{dA2}, ξA, M_{qA}
λ_{98}	-20.48	100	E''_{dA1}, E''_{dA2}, M_{qA}, N_{qA}, V_{cqA}

Figure 5-13 shows η factor for interaction modes between subsystems Grid B and MMC B subsystems. There is almost equal participation of the two subsystems in $\lambda_{85,86}$, $\lambda_{92,93}$ and λ_{94}. MMC B subsystem dominates in λ_{76}, while Grid B subsystem dominates in λ_{102}.

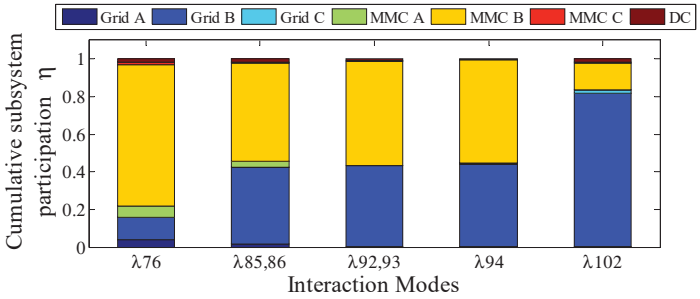

Figure 5-13 : Interaction modes between Grid B and MMC B subsystems

Table 5-17 lists the interaction modes between Grid B and MMC B subsystems, and 5 state variables with the largest participation in the modes. Similar to the case above, the modes are well damped and located on the far left side of the s-plane. The q-axis control of the MMC and the sub transient voltage state variables of the generators have the highest participations in the interaction modes.

Table 5-17 : Dominant state variables interaction modes between Grid B and MMC B

Mode #	Eigenvalue	ζ [%]	Dominant state variables
λ_{76}	-30.6	100	N_{qB}, M_{dB}, I_{gqB}, ξ_B, x_{PLLB}
$\lambda_{85,86}$	-26.3 ± j0.3	99.99	M_{dB}, E''_{qB1}, ξ_B, M_{qB}, E''_{qB2}
$\lambda_{92,93}$	-22 ± j1.06	99.88	M_{qB}, E''_{qB3}, E''_{qB2}, $E''qB1$, N_{qB}
λ_{94}	-22.91	100	M_{qB}, M_{dB}, E''_{qB1}, E''_{qB3}, E''_{qB2}
λ_{102}	-17.26	100	E''_{dB3}, E''_{dB2}, E''_{dB1}, E''_{qB1}, x_{PLLB}

No interaction modes were found with participation from Grid C and MMC C subsystems.

5.5.2. Converter interaction modes

Converter interaction modes are defined here as modes with at least 10% cumulative participation from all three MMC converter systems. Figure 5-14 shows converter interaction modes for the study system. In modes $\lambda_{5,6}$ and $\lambda_{26,27}$, the dc subsystem has a significant participation in addition to the MMC subsystems, while λ_{182} and λ_{183} have participation only from the converter subsystems.

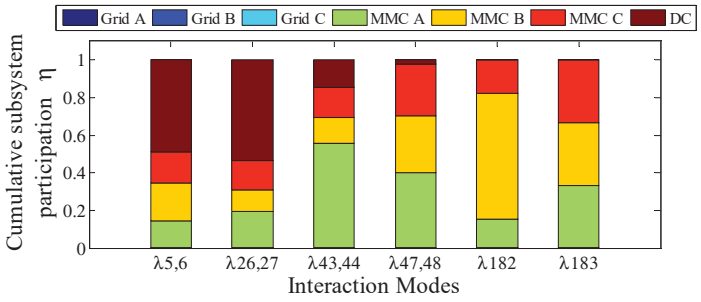

Figure 5-14 : Interaction modes with participation from all converters

Table 5-18 : Converter interaction modes with dominant state variables

Mode #	Eigenvalue	ζ [%]	Dominant state variables
$\lambda_{5,6}$	-305.23 ± *j*2733.16	11.1	v_{dcB}, v_{dcC}, v_{dcA}, i_{czB}, i_{dc12_AB}
$\lambda_{26,27}$	-103.98 ± *j*1080.52	9.58	i_{czA}, i_{czC}, i_{czB}, v_{dc2_AC}, v_{dc3_AC}
$\lambda_{43,44}$	-89.56 ± *j*164.02	47.92	$w_{\Sigma zA}$, N_{dA}, $w_{\Sigma zC}$, v_{sdA}, i_{gdA}
$\lambda_{47,48}$	-11.029 ± *j*90.77	12.06	$w_{\Sigma zA}$, N_{dA}, N_{dB}, N_{dC}, $w_{\Sigma zB}$
λ_{182}	-1	100	κ_B, κ_C, κ_A, $w_{\Sigma zB}$, $w_{\Sigma zC}$
λ_{183}	-1	100	κ_C, κ_A, κ_B, ξ_C, ξ_A

From the dominant state variables in the converter interaction modes shown in Table 5-18, it can be observed that dc voltage, circulating current and zero-sequence-energy dynamics are the state variables that have the highest participation in the interaction modes along with states associated with zero-sequence circulating current and energy controllers. In $\lambda_{5,6}$ and $\lambda_{26,27}$, the cable subsystem has almost 50% cumulative participation. However, from the dominant state variables listed in Table 5-18, it can be seen that the dc voltage and circulating current state variables of the converter have the highest participation in the mode followed by cable state variables. This is one of the

shortcomings of this method as discussed in the beginning of this section. In the other interaction modes, the converter subsystems dominate, and it is supported by the dominant state variables listed in the table.

In the ac-to-converter interaction modes, the outer loop and mostly the q-axis controller had high participations. On the other hand, in the converter interaction modes, zero-sequence circulating current and energy controller state variables participate the most. Furthermore, there is no converter interaction mode with participation from the ac state, while the reverse was observed for the ac-converter interaction modes, where there were no interaction modes with participation from the dc (cable) subsystem.

5.5.3. AC-AC interaction modes

When MTDC terminals are operating in dc voltage droop control only, there are no modes with η > 10% from any two ac grid subsystems. However, when frequency droop is included to the outer control loop for frequency reserve sharing, the interaction modes shown in Figure 5-15 are found. The interaction modes are between Grid A and Grid B subsystems except for the oscillatory modes ($\lambda_{159,160}$ and $\lambda_{167,168}$) that have participation from Grid A and Grid C subsystems. In addition, mode λ_{83} has large participation from MMC B subsystem.

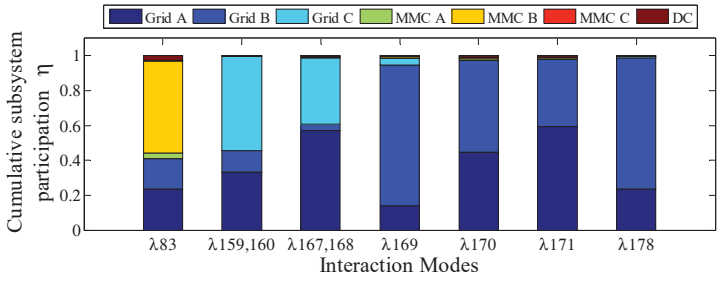

Figure 5-15 : Minimum two ac subsystems with at least 10% cumulative participation

Table 5-19 lists the damping ratio and most dominant states for each ac-to-ac interaction mode. Most of the modes are real modes except two ($\lambda_{159,160}$ and $\lambda_{167,168}$) that are oscillatory. However, some of the real modes are located very close to the imaginary axis. Therefore, depending on their sensitivities, a parameter variation can cause them to move to the right and lead to system instability. Most of the dominating state variables are

associated with governors and generator speed. This is due to the frequency droop controller through which system frequency reserve sharing is realized.

Table 5-19 : Interaction modes between any two ac subsystems

Mode #	Eigenvalue	ζ [%]	Dominant states
λ_{83}	-27.04	100	M_{dB}, E''_{d2}, ξ_B, N_{qB}, M_{qB}
$\lambda_{159,160}$	-0.20 ± *j* 0.24	64.47	x_{gov2C}, x_{gov2A}, $\Delta\omega_{C4}$, $\Delta\omega_{C1}$, $\Delta\omega_{C2}$
$\lambda_{167,168}$	-0.34 ± *j* 0.22	83.59	x_{gov2A}, x_{gov2C}, $\Delta\omega_{A1}$, $\Delta\omega_{A2}$, $\Delta\omega_{C4}$
λ_{169}	-0.41	100	x_{gov2B}, x_{gov2A}, $\Delta\omega_{B3}$, $\Delta\omega_{B2}$, $\Delta\omega_{B1}$
λ_{170}	-0.85	100	$\Delta\omega_{B3}$, $\Delta\omega_{B2}$, $\Delta\omega_{A1}$, $\Delta\omega_{B1}$, x_{AVR2A}
λ_{171}	-0.93	100	x_{AVR2A}, $\Delta\omega_{A1}$, x_{AVR1A}, $\Delta\omega_{A2}$, $\Delta\omega_{B3}$
λ_{178}	-1.14	100	x_{AVR2B}, x_{AVR3B}, x_{AVR1B}, x_{AVR2A}, E'_{qB2}

5.5.4. Poorly damped modes

As seen from the ac-to-dc and converter interaction modes, this method does not discriminate based on damping ratio. So, the identified interaction modes were well damped with small likelihood of going unstable. Here, poorly damped interaction modes are defined as modes with at least 10% cumulative participation from two subsystems and with damping ratio less than 15%.

Figure 5-16 shows interaction modes with at least two subsystems participation in modes and with damping ratio less than 15%. The interacting subsystems are converters and cables in all identified modes. None of the poorly damped interaction modes has participation from any of the ac subsystems. Moreover, the result shows that most of the interaction modes have the largest participation from dc/cable subsystem. In modes $\lambda_{5,6}$ and $\lambda_{26,27}$, even though the cable subsystem has the highest participation, the three converter subsystems participate as well. In mode $\lambda_{37,38}$, MMC C subsystem dominates while in $\lambda_{47,48}$ all the converter subsystems participate proportionally.

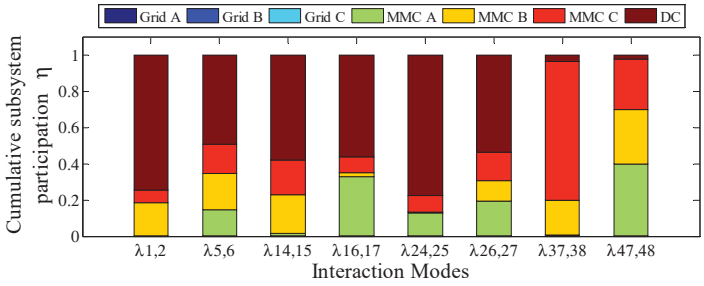

Figure 5-16 : Interaction modes with at least 2 subsystem participation and damping ratio less than 15%

From the dominant state variables in the interaction modes in Table 5-20, it can be seen that the most participating state variable from the converters is the dc capacitor state variable followed by the circulating current state variable. In addition, the interaction modes that have participation from a converter and dc subsystems, have dominating state variables from the cable sections closest to the converters.

Table 5-20 : Poorly damped interaction modes damping ratio and dominant states

Mode #	Eigenvalue	ζ [%]	Dominant state variables
$\lambda_{1,2}$	-420.72 ± j 3148.51	13.2	v_{dcB}, v_{dc2_BC}, v_{dc3_BC}, i_{dc22_BC}, i_{dc12_BC}
$\lambda_{5,6}$	-305.23 ± j 2733.16	11.1	v_{dcB}, v_{dcC}, v_{dcA}, i_{czB}, i_{dc12_AB}
$\lambda_{14,15}$	-252.25 ± j 2237.88	11.2	v_{dcB}, v_{dcC}, i_{dc22_BC}, i_{czB}, i_{czC}
$\lambda_{16,17}$	-245.34 ± j 2122.69	11.5	v_{dcA}, i_{czA}, v_{dc3_AB}, v_{dc3_AC}, i_{dc22_AC}
$\lambda_{24,25}$	-202.65 ± j 1366.7	14.7	v_{dc3_BC}, v_{dc2_BC}, i_{dc12_BC}, v_{dc2_AB}, i_{czA}
$\lambda_{26,27}$	-103.98 ± j 1080.52	9.6	i_{cz}, i_{czC}, i_{czB}, v_{dc2_AC}, v_{dc3_AC}
$\lambda_{37,38}$	-29.71 ± j 223.06	13.2	v_{cdC}, v_{cqC}, I_{gdC}, $\omega\Sigma zC$, I_{gqC}
$\lambda_{47,48}$	-11.03 ± j 90.77	12.1	$\omega_{\Sigma zA}$, N_{dA}, N_{dB}, N_{dC}, $\omega_{\Sigma zB}$

To summarize, it was found that q-axis converter controller and generators' sub-transient voltage state variables participate most in interaction modes between an ac grid and a converter, while d-axis, circulating current and zero-sequence energy converter controller state variables participate most in interaction modes between all three converters. In addition, generator speed and governor/turbine state variables participate most in interaction modes between asynchronous ac grids, which were are only found when frequency reserve sharing using the dc grid was activated. Most of the interaction modes identified were stable and well damped, and poorly damped interaction modes have participation from the cable and dc link capacitor states.

5.6. State matrix

In this subsection, a qualitative analysis of state matrix of a single 2-level converter with and without connection to an ac grid is used to supplement and extend the quantitative analysis presented in the previous sections. The single 2-level converter shown in Figure 5-17 is used in the analysis. The converter is connected to a constant dc voltage source on the dc side and to a stiff bus on the ac side through a phase reactor.

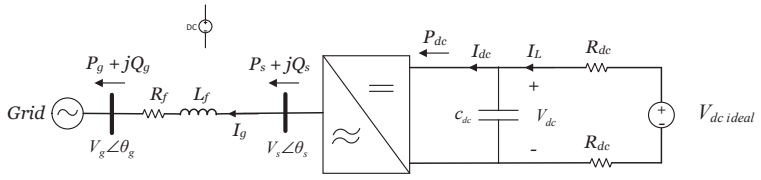

Figure 5-17 : A simple system with single 2-level converter connected to stiff voltage sources

The linearized state space representation of the system was computed for three converter control strategies: constant ac power control, constant dc voltage control and dc voltage droop control. The linearized state space representation of the system has the form:

$$\Delta\dot{\mathbf{x}} = \mathbf{A}\Delta\mathbf{x} + \mathbf{B}\Delta\mathbf{u} \tag{5.5}$$

where the state vector $\Delta\mathbf{x}$ is the same for all three control modes, while the input vector $\Delta\mathbf{u}$ is different for the three control modes:

$$\Delta\mathbf{x} = \begin{bmatrix} i_{gd} & i_{gq} & N_d & N_q & M_d & M_q & v_{sd} & v_{sq} & v_{dc} \end{bmatrix}^T \tag{5.6}$$

$$\begin{aligned} \Delta\mathbf{u}_{(P\ control)} &= \begin{bmatrix} P_{ref} & Q_{ref} & v_{gd} & v_{gq} & v_{dc\ ideal} & \omega_{pll} \end{bmatrix}^T \\ \Delta\mathbf{u}_{(Vdc\ control)} &= \begin{bmatrix} V_{dcref} & Q_{ref} & v_{gd} & v_{gq} & v_{dc\ ideal} & \omega_{pll} \end{bmatrix}^T \\ \Delta\mathbf{u}_{(Vdc\ droop\ control)} &= \begin{bmatrix} P_{ref} & V_{dcref} & Q_{ref} & v_{gd} & v_{gq} & v_{dc\ ideal} & \omega_{pll} \end{bmatrix}^T \end{aligned} \tag{5.7}$$

where:

i_{g_dq}	current flowing from the converter into the grid in dq- reference frame
M_d	state variable associated with the PI in the d-axis outer controller
M_q	state variable associated with the PI in the q-axis outer controller
N_d	state variable associated with the PI in the d-axis inner current controller
N_q	state variable associated with the PI in the q-axis inner current controller
P_{ref}	active power reference
Q_{ref}	reactive power reference
$V_{dc\,ref}$	dc voltage reference
$v_{dc\,ideal}$	dc voltage source
v_{dc}	dc voltage
v_{g_dq}	PCC voltage in dq reference frame
v_{s_dq}	internal VSC voltage in dq reference frame
ω_{pll}	grid frequency measured by a PLL

If the state variables of the system are categorized into ac states $\Delta\mathbf{x}_{ac}$ and dc states $\Delta\mathbf{x}_{dc}$, then the state matrix $\mathbf{A}$ can be divided into four submatrices, where each submatrix indicates one way coupling of ac state dynamics ($\Delta\dot{\mathbf{x}}_{ac}$) and dc state dynamics ($\Delta\dot{\mathbf{x}}_{dc}$) to ac and dc state variables, respectively.

$$\begin{bmatrix}\Delta\dot{\mathbf{x}}_{ac}\\ \Delta\dot{\mathbf{x}}_{dc}\end{bmatrix}=\begin{bmatrix}\mathbf{A}_{ac\text{-}to\text{-}ac} & \mathbf{A}_{dc\text{-}to\text{-}ac}\\ \mathbf{A}_{ac\text{-}to\text{-}dc} & \mathbf{A}_{dc\text{-}to\text{-}dc}\end{bmatrix}\begin{bmatrix}\Delta\mathbf{x}_{ac}\\ \Delta\mathbf{x}_{dc}\end{bmatrix} \tag{5.8}$$

or,

$$\begin{aligned}\Delta\dot{\mathbf{x}}_{ac}&=\mathbf{A}_{ac\text{-}to\text{-}ac}\Delta\mathbf{x}_{ac}+\mathbf{A}_{dc\text{-}to\text{-}ac}\Delta\mathbf{x}_{dc}\\ \Delta\dot{\mathbf{x}}_{dc}&=\mathbf{A}_{ac\text{-}to\text{-}dc}\Delta\mathbf{x}_{ac}+\mathbf{A}_{dc\text{-}to\text{-}dc}\Delta\mathbf{x}_{dc}\end{aligned} \tag{5.9}$$

where $\mathbf{A}_{ac\text{-}to\text{-}ac}$ connects ac state variables to ac dynamics, $\mathbf{A}_{dc\text{-}to\text{-}ac}$ connects dc state variables to ac dynamics, $\mathbf{A}_{ac\text{-}to\text{-}dc}$ connects ac state variables to dc dynamics, and $\mathbf{A}_{dc\text{-}to\text{-}dc}$ connects dc state variables to dc dynamics. If any of the off-diagonal submatrices is a zero matrix, then there would be no connection between the corresponding state variables and the state dynamics. If the state variables of the single converter system in (5.6) are categorized into dc states and ac states, then state variable v_{dc} would be the only dc state, while the rest of the state variables would belong to ac states.

$$\begin{aligned}\mathbf{x}_{ac}&=\begin{bmatrix}i_{gd} & i_{gq} & N_d & N_q & M_d & M_q & v_{sd} & v_{sq}\end{bmatrix}^T\\ \mathbf{x}_{dc}&=\begin{bmatrix}v_{dc}\end{bmatrix}\end{aligned} \tag{5.10}$$

Figure 5-18 shows the sparsity matrix of the state matrix $\mathbf{A}$ for the three converter control strategies. The symbolic state matrix $\mathbf{A}$ and input matrix $\mathbf{B}$ for all three control strategies considered are presented in Appendix A1.

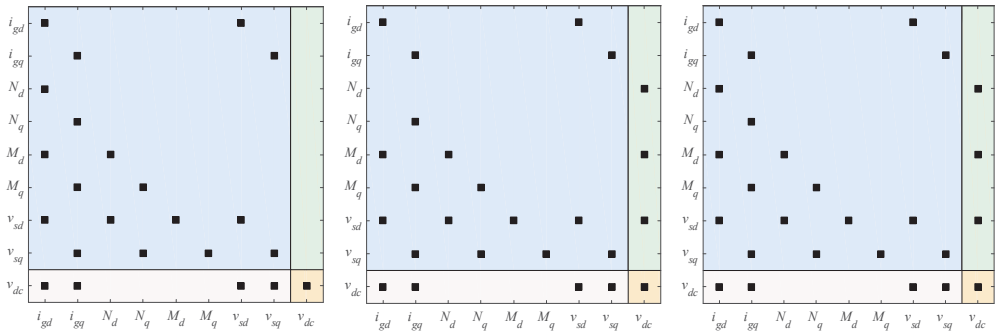

(a) (b) (c)

Figure 5-18 : Sparsity matrix of the state matrix $\mathbf{A}$ for a single 2-level converter for (a) constant power, (b) constant dc voltage, and (c) active power with dc voltage droop control strategies

The color shadings in Figure 5-18 show couplings between state dynamics and state variables. The blue shading indicates coupling of ac state dynamics to ac state variables, while the beige/ecru shading shows coupling of dc state dynamics to dc state variable. The green shading indicates coupling of ac state dynamics to the dc state variable, while the off-white shading indicates coupling of dc state variable dynamics to ac state variables. For all three converter control modes, the dc state variable dynamics ($\dot{v}_{dc}$) is coupled with the ac state variables i_{gd}, i_{gq}, v_{sd} and v_{sq}. This is because of active power balance on the ac and dc side of the converter (Equation (3.14)). On the other hand, the coupling of the ac state variable dynamics to the dc state variable is different under the different control modes. In constant power control mode, none of the ac state variable dynamics is linked to the dc state variable v_{dc}. In constant, under dc voltage and dc voltage droop control modes, the dynamics of $\dot{N}_d$, $\dot{M}_d$ and $\dot{v}_{sd}$ are linked to the dc state variable v_{dc}. This is because d-axis is used for dc voltage control. Note that $\dot{N}_d$ is linked to only v_{dc} in constant dc voltage control, while it is linked to i_{gd} and v_{dc} in active power control with dc voltage droop control.

From the qualitative analysis of the relationship between state dynamics to state variables under the different converter control strategies, it can be observed that ac dynamics is

coupled with dc dynamics under the three control strategies, while dc dynamics is coupled with ac dynamics when the converter operates under constant dc voltage or dc voltage droop control mode. However, dc dynamics is not coupled with ac dynamics when the converter operates in constant power control mode. Note that that dc grid dynamics will be coupled with ac grid dynamics under constant power control mode if the active power measurement comes from the dc side of the converter instead of the PCC on the ac side.

The following numerical example is used to further illustrate the findings from the qualitative analysis. For an initial steady state power flow depicted in Figure 5-19, linear analysis of the single terminal converter gives the eigenvalues listed in Table 5-21.

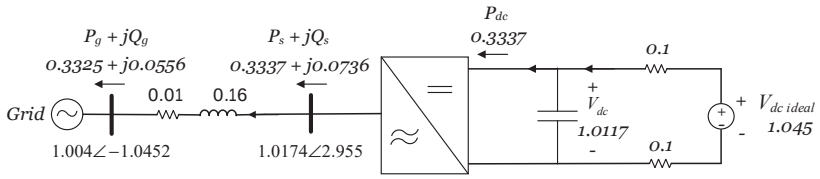

Figure 5-19 : Example

Table 5-21 : Eigenvalues of a single converter for different converter control strategies

Mode	**Eigenvalues**		
	Constant active power	***Constant dc voltage***	***DC voltage droop***
λ_1	-156.03	-625.01 + *j* 705.95	-626.07 + *j* 724.97
λ_2	-630.1 + *j*731.27	-625.01 - *j* 705.95	-626.07 - *j* 724.97
λ_3	-630.1 - *j* 731.27	-302. + *j* 402	-324.45 + *j* 407.85
λ_4	-335.67 + *j* 418.56	-302. - *j* 402	-324.45 - *j* 407.85
λ_5	-335.67 - *j* 418.56	-261.61	-110.32 + *j* 91.28
λ_6	-34.26 + *j* 1.77	-6.14	-110.32 - *j* 91.28
λ_7	-34.26 - *j* 1.77	-34.25	-34.35
λ_8	-19.61 + *j* 0.32	-19.37	-19.63 + *j* 0.12
λ_9	-19.61 - *j* 0.32	-19.93	-19.63 - *j* 0.12

The right eigenvector matrix ($\mathbf{\Phi}$) for the converter under constant active power control is presented in Table 5-22. It can be seen that λ_1 is only observable in dc voltage state variable (v_{dc}) state variable, while the other modes, λ_2 to λ_9, are observable in all state variables including the dc voltage state variable (v_{dc}). This indicates that λ_1 is solely a dc mode. The

zero values of observability/mode shape of λ_1 in the ac state variables show that the dc dynamics does not enter the ac grid, and is only confined to the dc grid. Thus, the dc dynamics, which is represented by λ_1, is decoupled from the ac dynamics. On the other hand, modes λ_2 to λ_9 are ac modes, with high observability in the ac state variables. However, these modes are also observable in the dc state variables, indicating that the ac modes/dynamics enter the dc grid and can be observed in the dc system.

Table 5-22 : Normalized right eigenvector matrix for constant active power control

	λ_1	λ_2	λ_3	λ_4	λ_5	λ_6	λ_7	λ_8	λ_9
I_{gd}	0	1	1	1	1	0.97	0.97	0.55	0.55
I_{gq}	0	1	1	1	1	0.97	0.97	0.55	0.55
N_d	0	0.04	0.04	0.07	0.07	1	1	1	1
N_q	0	0.04	0.04	0.07	0.07	1	1	1	1
M_d	0	0.01	0.01	0.01	0.01	0.01	0.01	0.1	0.1
M_q	0	0.01	0.01	0.01	0.01	0.01	0.01	0.1	0.1
v_{sd}	0	0.38	0.38	0.41	0.41	0.15	0.15	0.09	0.09
v_{sq}	0	0.38	0.38	0.41	0.41	0.15	0.15	0.09	0.09
v_{dc}	1	0.02	0.02	0.03	0.03	0.13	0.13	0.07	0.07

Table 5-23 and

Table 5-24 present right eigenvector matrix for the example system with the converter under constant dc voltage control and dc voltage droop control. For both converter control modes, the eigenvalues in the system are observable in all state variables in the system.

Table 5-23 : Normalized right eigenvector matrix for constant dc voltage control

	λ_1	λ_2	λ_3	λ_4	λ_5	λ_6	λ_7	λ_8	λ_9
I_{gd}	0.91	0.91	1	1	1	0.66	0.04	0.48	0.47
I_{gq}	1	1	0.79	0.79	0.31	0	0.97	0.55	0.56
N_d	0.001	0.001	0.01	0.01	0.05	1	0.01	0.25	0.24
N_q	0.04	0.04	0.06	0.06	0.04	0.001	1	1	1
M_d	0.01	0.01	0.01	0.01	0.01	0.01	0.01	0.13	0.13
M_q	0.01	0.01	0.01	0.01	0.01	0.001	0.01	0.10	0.10
v_{sd}	0.33	0.33	0.36	0.36	0.17	0.001	0.15	0.09	0.09
v_{sq}	0.37	0.37	0.34	0.34	0.12	0.11	0.01	0.08	0.08
v_{dc}	0.02	0.02	0.04	0.04	0.15	0.07	0.01	0.06	0.06

Table 5-24 : Normalized right eigenvector matrix for active power with dc voltage droop control

	λ_1	λ_2	λ_3	λ_4	λ_5	λ_6	λ_7	λ_8	λ_9
I_{gd}	0.97	0.97	1	1	0.92	0.92	0.02	0.14	0.14
I_{gq}	1	1	0.91	0.91	0.13	0.13	0.97	0.39	0.39
N_d	0.03	0.03	0.07	0.07	1	1	0.07	1.00	1
N_q	0.04	0.04	0.06	0.06	0.03	0.03	1	0.71	0.71
M_d	0.01	0.01	0.01	0.01	0.01	0.01	0.01	0.21	0.21
M_q	0.01	0.01	0.01	0.01	0.00	0.00	0.01	0.07	0.07
v_{sd}	0.36	0.36	0.39	0.39	0.08	0.08	0.16	0.06	0.06
v_{sq}	0.38	0.38	0.37	0.37	0.15	0.15	0.01	0.02	0.02
v_{dc}	0.02	0.02	0.03	0.03	0.14	0.14	0.001	0.02	0.02

Now, consider the system shown in Figure 5-20. The single converter is now connected to a small grid with two generators and two loads on the ac side. A constant dc voltage source is still used on the dc side.

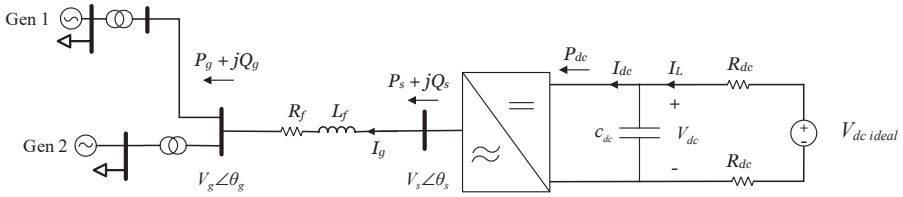

Figure 5-20 : Multi-machine ac grid connected to a single converter

The generators in the ac grid are modelled as a third order model, i.e. only the first three equations in (3.1) are used. The generators are represented by d and q-axes transient voltages E'_d and E'_q behind transient reactances X'_d and X'_q with the assumption that E'_d is constant. Therefore, each generator has rotor angle, speed deviation and transient voltage, δ, $\Delta\omega$, E'_q, as state variables. In addition, a PLL is used to estimate PCC voltage angle and converter control dq-frame rotational speed. The state variable vector $\Delta\mathbf{x}$ and input vectors $\Delta\mathbf{u}$ in (5.5) for the updated system under different converter control strategies become:

$$\Delta\mathbf{x} = \begin{bmatrix} \delta_1 & \Delta\omega_1 & E'_{q1} & \delta_2 & \Delta\omega_2 & E'_{q2} & x_{pll} & \theta_{pll} & i_{gd} & i_{gq} & N_d & N_q & M_d & M_q & v_{sd} & v_{sq} & v_{dc} \end{bmatrix}^T$$

(5.11)

$$\Delta\mathbf{u}_{(P\ control)} = \begin{bmatrix} P_{ref} & Q_{ref} & V_{dc\ ideal} & \omega_{pll} & E_{fd1} & E_{fd2} & E'_{d1} & E'_{d2} \end{bmatrix}^T$$
$$\Delta\mathbf{u}_{(V_{dc}\ control)} = \begin{bmatrix} V_{dcref} & Q_{ref} & V_{dc\ ideal} & \omega_{pll} & E_{fd1} & E_{fd2} & E'_{d1} & E'_{d2} \end{bmatrix}^T \quad (5.12)$$
$$\Delta\mathbf{u}_{(V_{dc}\ droop\ control)} = \begin{bmatrix} P_{ref} & V_{dcref} & Q_{ref} & V_{dc\ ideal} & \omega_{pll} & E_{fd1} & E_{fd2} & E'_{d1} & E'_{d2} \end{bmatrix}^T$$

where the subscripts 1 and 2 indicate that the state variables belong to Gen1 and Gen2, respectively and the variables indicate:

E'_q	q- axis transient voltage
E_{fd}	field excitation voltages
δ	rotor angle
i_{g_dq}	current flowing from the converter into the grid in dq- reference frame
M_d	state variable associated with the PI in the d-axis outer controller
M_q	state variable associated with the PI in the q-axis outer controller
N_d	state variable associated with the PI in the d-axis inner current controller
N_q	state variable associated with the PI in the q-axis inner current controller
P_{ref}	active power reference
Q_{ref}	reactive power reference
$V_{dc\ ref}$	dc voltage reference
$v_{dc\ ideal}$	dc voltage source
v_{dc}	dc voltage
v_{g_dq}	PCC voltage in dq reference frame
v_{s_dq}	internal VSC voltage in dq reference frame
ω_{pll}	grid frequency measured by a PLL

The system in Figure 5-20 is used to explain coupling between state variables under different converter control strategies. For simplicity, the state variables are grouped as dc (v_{dc}), generator ($\delta, \Delta\omega, E'_q$), converter state variables (the remaining elements of $\Delta\mathbf{x}$). The generator and converter state variables together form ac state variable group. Gen 1 is used as a reference machine. Thus, δ_1 is always zero and disappears from the state matrix.

$$\mathbf{x}_{ac} = \begin{bmatrix} \Delta\omega_1 & E'_{q1} & \delta_2 & \Delta\omega_2 & E'_{q2} & x_{pll} & \theta_{pll} & i_{gd} & i_{gq} & N_d & N_q & M_d & M_q & v_{sd} & v_{sq} \end{bmatrix}^T$$
$$\mathbf{x}_{dc} = \begin{bmatrix} v_{dc} \end{bmatrix}$$

(5.13)

Figure 5-21 shows the sparsity matrix for the state matrix $\mathbf{A}$ under constant power and constant dc voltage control modes on the same plot. The interpretations of the color shadings are the same as above, where blue shading indicates coupling of ac state dynamics to ac state variables, while beige/ecru shading shows coupling of dc state dynamics to dc state variable. The green shading indicates coupling of ac state dynamics to the dc state variable, while the off-white shading indicates coupling of dc state variable dynamics to ac state variables. The ac state variable dynamics are not coupled with dc state variable in constant power control mode, while there is a coupling between ac state dynamics and dc state variable in constant dc voltage control mode. The difference between the two control modes is associated with the d-axis PI controller related state variable dynamics ($\dot{N}_d$ and $\dot{M}_d$). When constant power control is used, $\dot{N}_d$ and $\dot{M}_d$ are coupled with the generator state variables, δ_2, E'_{q1} and E'_{q2}, in addition to PLL and converter associated state variables θ_{pll}, i_{gd}, v_{sd} and v_{sq}. However, $\dot{N}_d$ and $\dot{M}_d$ have no coupling with v_{dc}. On the other hand, under constant dc voltage control mode, $\dot{N}_d$ and $\dot{M}_d$ are coupled with v_{dc} but not with the generator state variables. Thus, the converter controllers state dynamics have more coupling with the generator state variable under constant power control than constant dc voltage control mode.

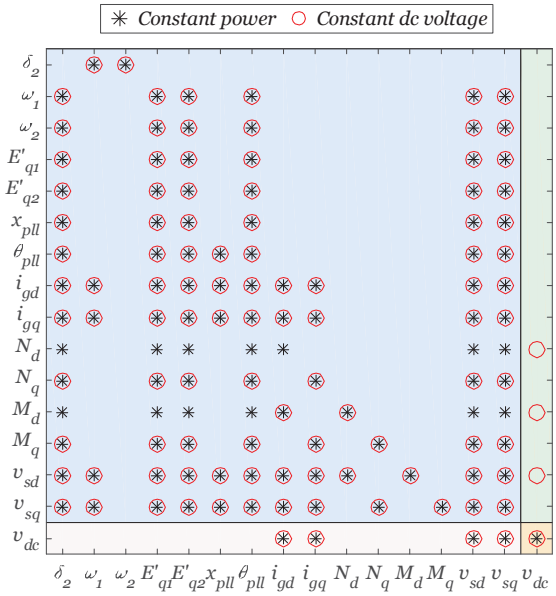

Figure 5-21 : Sparsity matrix of state matrix $\mathbf{A}$ for constant power and constant dc voltage converter control

The sparsity matrix for the state matrix $\mathbf{A}$ for the ac grid and single converter system under constant power and dc voltage droop control modes are plotted together in Figure 5-22. The difference between the two control modes is that no coupling exists between ac state dynamics and dc state in constant power control mode, while ac state dynamics is coupled to the dc state in dc voltage droop control through $\dot{N}_d$, $\dot{M}_d$ and $\dot{v}_{sd}$.

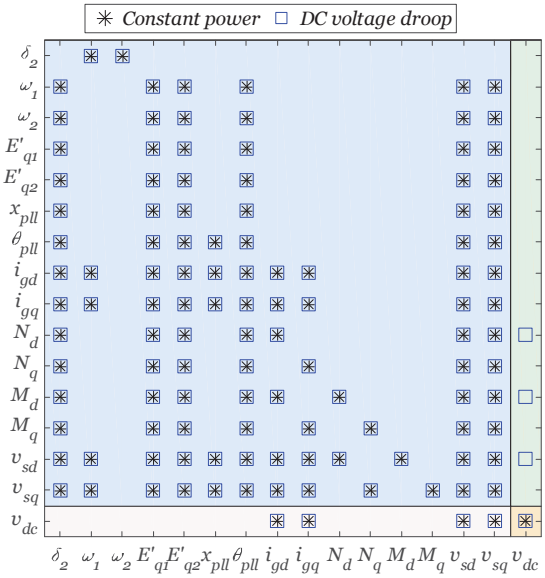

Figure 5-22 : Sparsity matrix of state matrix A for constant power and dc voltage droop converter control

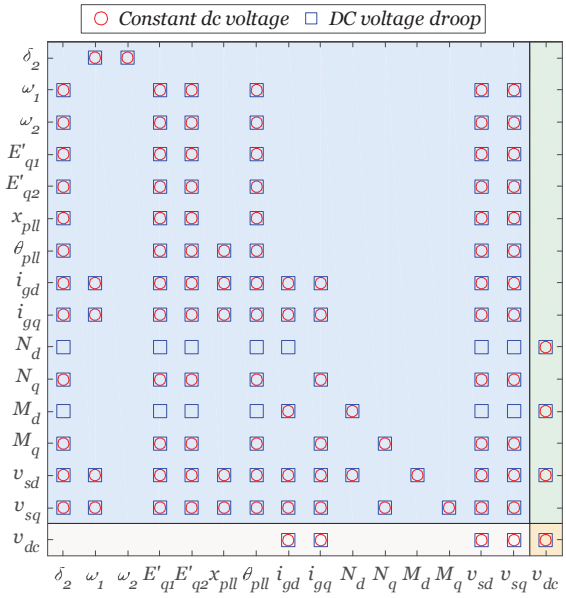

Figure 5-23 : Sparsity matrix of state matrix A for constant dc voltage and dc voltage droop converter control

Figure 5-23 shows the sparsity matrix for the state matrix $\mathbf{A}$ under constant dc voltage and dc voltage droop control modes on the same plot. The ac-to-dc ($\mathbf{A}_{\text{ac-to-dc}}$), dc-to-ac ($\mathbf{A}_{\text{dc-to-ac}}$) and dc-to-dc ($\mathbf{A}_{\text{dc-to-dc}}$) coupling for the two control modes are the same, but the ac-to-ac ($\mathbf{A}_{\text{ac-to-ac}}$) coupling is different. Under dc voltage droop control mode, $\dot{N}_d$ and $\dot{M}_d$ are coupled with the generator state variables, δ_2, E'_{q1} and E'_{q2}, in addition to PLL and converter associated state variables θ_{pll}, i_{gd}, v_{sd} and v_{sq}, while it is not so under constant dc voltage control mode.

In general, regarding coupling between ac and dc dynamics, the conclusions from the single converter stiff bus analysis still holds. There is a two way coupling between ac and dc dynamics when the converter operates in constant dc voltage and dc voltage droop control modes as depicted by the two arrows pointing in opposite directions in Figure 5-24(b) and Figure 5-24(c). Meaning, ac grid dynamics is coupled with dc grid dynamics and, at the same time, dc grid dynamics is coupled with ac grid dynamics. However, when the converter operates in constant power control mode, there is only a one way coupling between ac and dc dynamics. The ac dynamics is coupled with dc dynamics, while dc dynamics is not coupled with ac dynamics when the converter operates in constant power control mode, as depicted in Figure 5-24 (a).

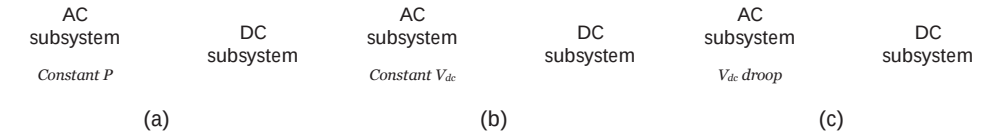

Figure 5-24 : Coupling between ac and dc subsystems under (a) constant power, (b) constant dc voltage and (c) dc voltage droop operation of the converter

5.7. Chapter summary

In this chapter, eigenvalue analysis, in particular, mode shapes and participation factors, were used to identify and analyze interactions (dynamic coupling) between different subsystems in a hybrid ac/dc power system. First, mode shape magnitudes were used to identify electromechanical interactions between generators located in asynchronous grids. Time domain analysis was used to support and give an intuitive understanding of the results from mode shape analysis. The inter-grid electromechanical couplings are generally weak but are influenced by dc grid control strategy and controller tuning. In addition, the interaction is also influenced by the frequency of the dominant modes in

each grid. More specifically, it was found that the interaction increases when the dominant modes in each ac grid have a similar damped frequency.

Then, a participation factor based interaction mode identification method was used to identify interaction modes in which more than one subsystems participate to a certain extent. The method was used to identify interaction modes between ac grids and converters, in between several converters and ac grids. It was found that state variables associated with generators and outer controller of converters participate most in interaction modes between an ac grid and a converter, while state variables associated with circulating current and zero-sequence energy converter controller state variables participate most in interaction modes between converters. In addition, generator speed and governor/turbine state variables participate most in interaction modes between asynchronous ac grids, which were only found when frequency reserve sharing using the dc grid is activated. Most of the interaction modes identified were stable and well damped. DC cable and dc-link capacitor state variables participate most in poorly damped interaction modes.

Finally, a qualitative analysis of state matrix of a single 2-level converter with and without connection to a detailed ac grid model was used to supplement the findings of quantitative eigenvalue analysis. It was shown that there is a two way coupling between ac and dc grids when the converter is operated in constant dc voltage or dc voltage droop control modes, i.e. ac grid dynamics is coupled with dc grid dynamics and dc grid dynamics is coupled with ac grid dynamics. However, there is only a one-way coupling between an ac grid and a dc grid if the converter is operated in constant power control mode. In such cases, the ac grid dynamics is coupled with the dc grid dynamics, but the dc grid dynamics is not coupled with the ac grid dynamics.

6. Decentralized Power Oscillation Damping Controller Interaction

Recently, the number of power electronics interfaced renewable energy sources (RES) such as wind and solar has increased. These types of sources are increasingly covering the growing electricity demand, and their share in the total power generation portfolio is becoming significant. On the other hand, high voltage direct current (HVDC) transmission systems are being used to connect the RES to the grid, and to exchange balancing power that is needed to mitigate the power fluctuations resulting from RES. This large penetration of RES and HVDC interconnections has changed the way the electricity grid is being operated, and, consequently, these systems are expected to deliver power system services that used to be provided by conventional generators. To this end, the grid codes are being updated to include ancillary service requirements from RES and HVDC systems to ensure continuous, secure and stable operation of the power system. One such requirement is power oscillation damping capability. The ENTSO-E Network Code on High Voltage Direct Current Connections (NC HVDC) [69] specifies that HVDC systems, both HVDC links and multi-terminal direct current (MTDC) grids, shall be capable of contributing to the damping of power oscillations in connected ac networks.

Traditionally, large synchronous generators provided damping torque through power system stabilizers (PSS) to damp low frequency power oscillations in power systems. In addition, flexible ac transmission system (FACTS) devices such as static var compensator (SVC) and thyristor controlled series capacitor (TCSC) have been used for power oscillation damping. SVCs dynamically vary system voltage during power oscillations, thereby act to accelerate or decelerate rotating machines in the system, while TCSC on tie lines regulate their capacitive reactance so that the line impedance changes in opposition to the power oscillation on the line.

Research works focusing on providing additional damping torque to ac grids through power oscillation damping (POD) controllers installed on HVDC or MTDC grids are found in the literature [62-64, 98]. The additional power can come either from ac grids or from offshore wind farms connected to the HVDC systems. If offshore wind farms are connected to the onshore grid via an HVDC link, then the POD controller can be installed either on the offshore wind turbines, on the onshore HVDC converter station, or a

combination of the two [62-64]. The first option requires communication to transfer onshore signals to offshore wind turbines. In addition to communication delays, challenges such as mechanical resonances with wind turbine generators, dc voltage variation and over-loading of the wind turbines may arise when POD controllers are installed on offshore wind turbines [62, 64]. On the other hand, need for communication can be avoided if the POD controllers are installed on the onshore converter stations and if local measurement signals are used. In such cases, the POD controller output modulates converter reference signals and its input/output signal selection is done in a systematic way to increase the effectiveness of the controllers. In the context of decentralized POD controllers installed at more than one terminal of an MTDC grid, their settings can be adjusted in such a way that their effectiveness is maximized. It was shown in [54] and [55] that using similar gain values with opposite signs and dc voltage closed-loop shaping, respectively, improves power oscillation damping in ac grids with embedded MTDC.

Previous works have focused on the capability of providing power oscillation damping from offshore wind farms via HVDC links and embedded MTDC grids and the effectiveness of the POD controllers. However, they did not address issues related to interaction between different POD controllers installed at different terminals of an MTDC grid and the effect it has on the performance of the PODs; thus, the stability of the connected ac grids.

This chapter analyses interaction between POD controllers installed at different terminals of an MTDC grid interconnecting asynchronous ac grids. The interaction analysis uses decentralized controllers design techniques to design the POD controllers. Relative gain array (RGA) and performance relative gain array (PRGA), introduced in Section 4.2, are used to gain insights on the nature of interactions between POD controllers. The rest of this Chapter is organized as follows. Section 6.1 describes aspects of decentralized controllers in the context of Multiple-Input-Multiple-Output (MIMO) power systems. In Section 6.2, POD controller on MTDCs and their design steps are presented. In Section 6.3, case studies and sensitivity analysis are carried out to study the level of POD interactions and their responsiveness to changes in controller parameter. Results and discussion are also presented in this section. Finally, the conclusions are outlined in 6.4.

6.1. Decentralized feedback control

When multiple POD controllers are used at different terminals of an MTDC grid to contribute to power oscillation damping in their respective connected ac grids, then the

system becomes a MIMO system with decentralized controllers as shown in Figure 6-1. The plant model is a combination of both the ac and dc grid or hybrid ac/dc grid, and the POD controllers inserted into MTDC converter controllers are the feedback controllers.

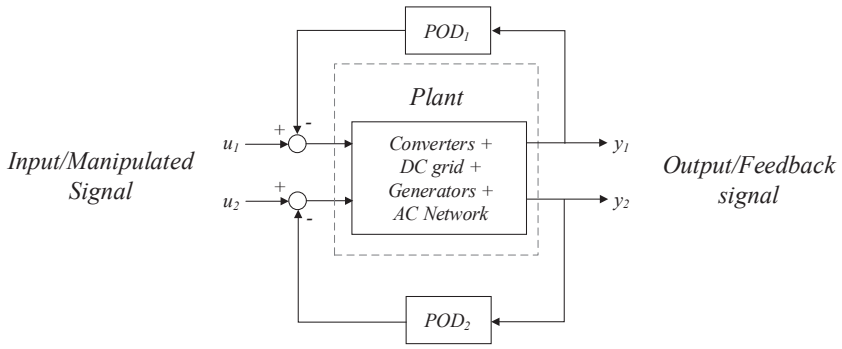

Figure 6-1: Block diagram for 2-input-2-output hybrid ac/dc power system plant with feedback PODs

As explained in Chapter 4, the transfer function for the plant model (MIMO system) has a general form given by:

$$\mathbf{G}(s)=\begin{bmatrix} g_{11}(s) & g_{12}(s) & \dots & g_{1m}(s) \\ g_{21}(s) & g_{22}(s) & \dots & g_{2m}(s) \\ \vdots & \vdots & \ddots & \vdots \\ g_{m1}(s) & g_{m2}(s) & \dots & g_{mm}(s) \end{bmatrix} \tag{6.1}$$

where $g_{ij}(s)$ is the transfer function from input j to output i.

In decentralized control, each controller has local measurements and makes its own decision. Decentralized control design uses diagonal or block diagonal control K(s) as in (6.2). If the MIMO system to be controlled G(s) is close to diagonal, then with decentralized controllers, it essentially becomes a collection of independent sub-systems. Large off-diagonal elements of G(s) result in poor performance of decentralized control due to interactions [93].

$$K(s) = diag\{k_i(s)\} = \begin{bmatrix} k_1(s) & & & \\ & k_2(s) & & \\ & & \ddots & \\ & & & k_m(s) \end{bmatrix} \quad (6.2)$$

Selection of input/output pairings and tuning of controllers are the two major steps in design of decentralized controller systems. Full coordinated, sequential or independent design approaches can be used for designing decentralized controllers.

In fully coordinated design, all diagonal elements $k_i(s)$ are designed simultaneously, which makes the design problem very difficult. In sequential design, the controllers are designed sequentially, one at a time, with the previously designed inner controllers implemented. Thus, each step in the design procedure involves one single-input-single-output (SISO) controller [99]. The faster inner loops are designed before the slower outer loops. However, stability is not guaranteed if an inner loop fails. In independent design, each controller $k_i(s)$ is designed based on the corresponding diagonal element of $G(s)$, such that the individual loop is stable. It is used when the individual parts of the system can operate independently. In general, independent designed is used when the system is decoupled in space ($G(s)$ close to diagonal), whereas sequential design is used when the system outputs can be decoupled in time [99].

Independent design is the appropriate design approach for the decentralized POD controllers on an MTDC interconnecting multiple asynchronous power system. This is because the individual ac grids can operate independently, and the plant model is close to diagonal as there is a weak coupling between an input in one ac grid and an output in another. Furthermore, from the practical point of view, different transmission system operators (TSO) would operate the different ac grids, and each POD at a terminal converter would be tuned according to the needs and requirements of the TSO.

Independent decentralized controller design involves two steps [93]:

- Step 1: selection of input-output pairs bearing in mind the three pairing rules
    - RGA matrix close to identity at frequencies around the closed loop bandwidth
    - Avoid pairings with negative steady state RGA elements
    - Prefer pairing with minimal restrictions on the achievable bandwidth

- Step 2: controllability analysis
    - Compute PRGA
    - Consider disturbance rejection

6.2. Design of power oscillation damping controllers on MTDC

Power oscillation damping (POD) controllers are used to provide additional damping torque to damp low frequency power oscillations. They are typically used on synchronous generators and are part of the excitation system. In such cases, the manipulated/input signal is automatic voltage regulator (AVR) voltage reference while a variety of signals, such as rotor speed, active power, voltage angle, etc., can be selected as measured/feedback signal. The term power system stabilizer (PSS) is used when the controllers are inserted in synchronous generators' control, while the term power oscillation damping controller is usually used when the controllers are used together with FACT devices and converters.

In principle, POD on a voltage source converter (VSC) can modulate either the active power or reactive power reference. However, it was shown in [62, 64, 100] that active power modulation gives better damping and is not sensitive to AVR settings or local voltage variations. Furthermore, active power has usually a priority over reactive power in the VSC control. Therefore, if the POD was to modulate reactive power reference, its performance would depend upon the available reactive power capacity and/or loading of the converter. In this work, it is chosen that the output of the POD controller modulates the active power reference in the outer control of the MTDC converter as shown in Figure 6-2.

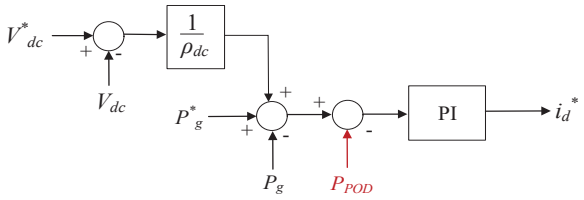

Figure 6-2: VSC dc voltage droop controller with POD

where V_{dc} and P_g are dc voltage and active power flow at the converter, respectively, while P_{POD} is the output of the POD controller. The superscript * indicates reference signals. The

control structure of a POD controller on VSC terminals of an MTDC grids is similar to power system stabilizer in excitation systems of synchronous generators in ac grids. Figure 6-3 shows a block diagram for a POD controller for MTDC converters.

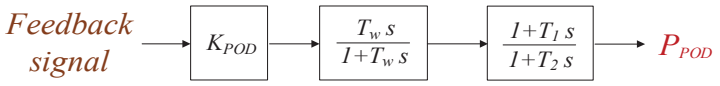

Figure 6-3: Block diagram for a POD on MTDC converters

where K_{POD} is a gain constant, T_w is wash-out filter time constant, while T_1 and T_2 are lead-lag time constants. Depending upon the phase compensation needed, more lead-lag blocks can be added. As mentioned earlier, the two most important steps in design of decentralized controller systems are selection of input/output signals and tuning of the controller. The following subsections discuss these topics in the context of POD controller design.

6.2.1. POD input/output signal selection

An important step in POD design process is selection of an input signal that gives a high controllability and an output signal that gives a high observability of the mode of interest. As explained earlier, power oscillation damping with MTDC converters is realized through the active power modulation. Therefore, active power references of the VSC converters are selected as input or manipulated signals. Frequency, point of common coupling (PCC) voltage, and angle are evaluated as possible output or controlled signals. These signals are measured or estimated locally by the phase locked loop (PLL). It is also possible to consider remote signals through wide area monitoring systems (WAMS), but the topic is out of the scope of this work as the focus here is on interaction between decentralized POD controllers.

Transfer function residues, which are a joint measure of observability and controllability, are typically used for the selection of feedback stabilizing signals and the location of PODs. However, given the fact that residues related to signals of different scales and units, such as frequency and voltage angle, cannot be compared with each other due to scaling issues, geometric measures for controllability and observability were proposed in [101]. Generally, geometric measures indicate controllability of a mode from an input and observability of a mode in an output. They are mathematically defined as the cosine of the angle between subspaces spanned by the eigenvectors of state matrix $\mathbf{A}$, and input/output

vectors in state space representation equation. Assume that $\boldsymbol{\phi}_i$ and $\boldsymbol{\psi}_i$ are right and left eigenvectors of matrix $\mathbf{A}$ associated with mode λ_i, respectively. Then, the geometric measures for observability (m_{oi}) and controllability (m_{ci}) of the mode on the l^{th} row of the output vector (c_l), and from the k^{th} column of the input vector (b_k), respectively, are defined as:

$$m_{ci}(k) = cos\left[\beta\left(\boldsymbol{\psi}_i^T, \mathbf{b}_k\right)\right] = \frac{\left|\boldsymbol{\psi}_i \cdot \mathbf{b}_k\right|}{\left\|\boldsymbol{\psi}_i^T\right\| \cdot \left\|\mathbf{b}_k\right\|} \tag{6.3}$$

$$m_{oi}(l) = cos\left[\beta\left(\mathbf{c}_l^T, \boldsymbol{\phi}_i\right)\right] = \frac{\left|\mathbf{c}_l \cdot \boldsymbol{\phi}_i\right|}{\left\|\mathbf{c}_l^T\right\| \cdot \left\|\boldsymbol{\phi}_i\right\|} \tag{6.4}$$

where β is the angle between the vectors, | | indicates absolute value and || || indicates L2-norm. If the vectors are orthogonal, i.e. β = 90°, then there is low observability of the mode on the output and/or controllability from the input. The product of the controllability and observability measures gives a joint geometric observability and controllability measure (m_{coi}) [102]:

$$m_{coi} = m_{oi}(l) \cdot m_{ci}(k) \tag{6.5}$$

A relative large value m_{coi} indicates the most effective input-output signal combination among the alternatives being considered. As m_{coi} is independent of scaling, input-output signals of different units can be compared.

6.2.2. POD tuning

Once the input and output signals for the controller are selected, then the next step is to tune the controller so as to achieve the best performance. In general, the intention is to increase the damping of the mode of interest. This is equivalent to shifting the mode to the left on the complex plane. There are different methods to tune a POD [103], but here the root locus method is used.

Root locus graphically traces the movement of modes in the complex plane when a gain, typically in a feedback controller, is varied from zero to infinity. The system transfer function is computed from the manipulated signal to the output of the wash out filter in Figure 6-3. Assume that the POD is tuned to increase the damping of a mode indicated by a red * symbol in Figure 6-4. The goal is to increase the damping ratio higher than ζ_2,

where $\zeta_1 < \zeta_2$. The compensation angle (θ) is estimated from the departure angle (δ) of the mode trajectory for an increase in gain constant, K_{POD}. The departure angle can also be calculated from a Nyquist plot. The compensation angle is calculated as shown in (6.6).

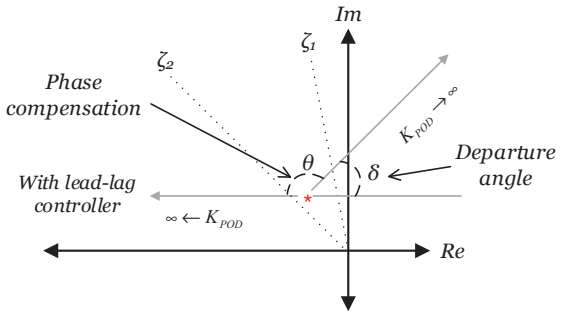

Figure 6-4 : Tuning with root locus method

$$\theta = 180 - \delta \tag{6.6}$$

where θ is the compensation angle and δ is the departure angle. Note that both root locus and the Nyquist plot assume a negative feedback. Therefore, if a positive feedback signal is used, as in the case of PSS on an AVR, then it is necessary to change the feedback to a negative feedback and compensate for the sign change by multiplying the input to the PSS by -1.

Once the phase compensation angle (θ) is found, then parameters α and T, which are used for tuning of the lead-lag controllers, are calculated as:

$$\begin{aligned} sin\left(\frac{\theta}{n}\right) &= \frac{1-\alpha}{1+\alpha} \\ T &= \frac{1}{\omega\sqrt{\alpha}} \end{aligned} \tag{6.7}$$

where ω is the frequency of the mode in rad/s and n is the number of lead-lags. The maximum phase compensation achieved with a single lead-lag controller is less than 90°. Therefore, if the phase compensation needed is greater than or equal to 90°, then multiple lead-lag controllers are used. The time constants for each lead-lag is related to α and T as:

$$\frac{1+T}{1+\alpha T} \tag{6.8}$$

With a proper selection of lead-lag parameters, the root locus for the system from the manipulated signal to an output after the lead-lag block(s) should have a modal trajectory towards the left (180°), as depicted in Figure 6-4. Then, an appropriate POD gain constant, K_{POD}, is chosen based on the root locus. It should be noted that while the mode under study moves to the left and becomes more damped, other modes in the system may become less damped. Therefore, it is important to pay attention to the movement of all modes so that the system remains stable.

6.3. Case study

Interaction between PODs connected to different terminals of an MTDC is explained using a case study. The methods and measures introduced in the previous sections for input/output selection and tuning are used. Furthermore, control loop interaction measures, dynamic relative gain array (DRGA) and performance relative gain array (PRGA), introduced in Chapter 4.2 are used to quantify the interaction between POD controllers.

The test study system is a three terminal two-level VSC based MTDC grid connecting three asynchronous ac grids as shown in Figure 6-5. All three ac grids have multiple generators, and represent large power systems. System topology and data for Grid A, Grid B, and Grid C are based on benchmark systems given in [72], [71], and [104], respectively. MATLAB/Simulink is used for the analyses. The DC grid is a symmetric monopolar system with ±200 kV voltage rating. The dc cables have a 900MW rating and their lengths are depicted in Figure 6-5. The MTDC terminal converters are operating in dc voltage droop control mode with 4% droop constant. Table 6-1 summarizes the initial load flows at the terminal converters of the study system. Positive power flow direction is defined as power flowing from dc grid into ac grid.

Table 6-1 : Initial load flow summary of the Study system

Terminal	P [MW]	Q [MVAr]	V_{dc} [pu]	ρ_{dc} [%]
A	198.9	0	0.98	4
B	-402.6	0	0.98	4
C	198.9	0	0.97	4

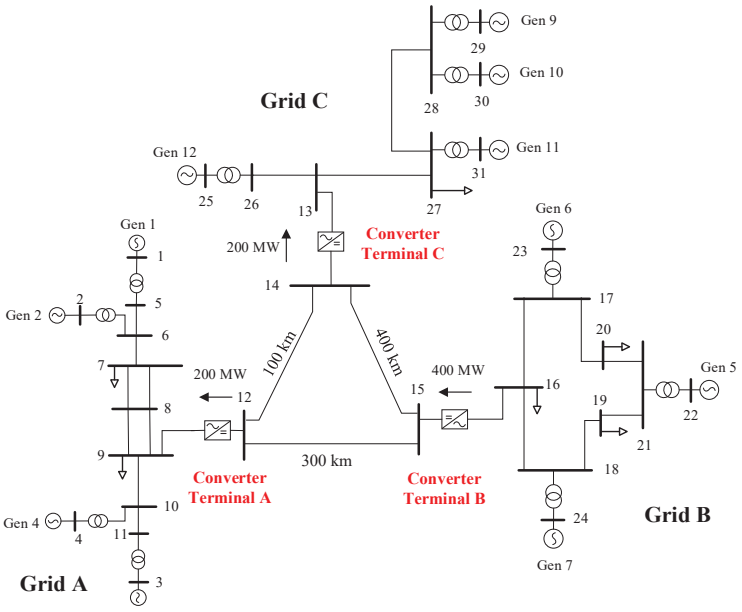

Figure 6-5: Study system

A linear analysis was carried out for the study system. Table 6-2 lists eigenvalues of the study system with damping ratio less than 15%. The participation factors of the modes reveal that most of the poorly damped modes are local and inter-area electromechanical modes in the ac grids.

Table 6-2: Poorly Damped Modes with Damping Ratio Less Than 15%

Mode	Eigenvalue	f [Hz]	ζ [%]	Dominant state variables
$\lambda_{84,85}$	-0.042 ± j3.57	0.57	1.18	δ_{A1}, δ_{A2}, $\Delta\omega_{A3}$, $\Delta\omega_{A4}$, $\Delta\omega_{A1}$
$\lambda_{88,89}$	-0.136 ± j3.11	0.50	4.35	δ_{C3}, $\Delta\omega_{C4}$, $\Delta\omega_{C1}$, $\Delta\omega_{C2}$, $\Delta\omega_{C3}$
$\lambda_{78,79}$	-0.479 ± j6.11	0.97	7.82	δ_{C2}, $\Delta\omega_{C3}$, $\Delta\omega_{C1}$, $\Delta\omega_{C2}$, E''_{dC4}
$\lambda_{68,69}$	-0.559 ± j6.96	1.11	8	δ_{A3}, $\Delta\omega_{A4}$, $\Delta\omega_{A3}$, δ_{A2}, E'_{d4}
$\lambda_{70,71}$	-0.619 ± j7.34	1.17	8.4	$\Delta\omega_{B2}$, δ_{B1}, δ_{B2}, $\Delta\omega_{B3}$, E''_{dB2}
$\lambda_{76,77}$	-0.672 ± j7.21	1.15	9.28	δ_{C1}, $\Delta\omega_{C2}$, $\Delta\omega_{C1}$, E''_{dC2}, E''_{dC1}
$\lambda_{72,73}$	-0.663 ± j6.8	1.08	9.7	δ_{A2}, $\Delta\omega_{A2}$, $\Delta\omega_{A1}$, δ_{A1}, E'_{d2}
$\lambda_{64,65}$	-0.997 ± j8.25	1.31	12	$\Delta\omega_{B1}$, δ_{B2}, δ_{B1}, $\Delta\omega_{B2}$, $\Delta\omega_{B3}$

POD controllers are installed on MTDC grid terminal converters to damp the inter-area modes in Grid A ($\lambda_{84,85}$) and Grid C ($\lambda_{88,89}$) through modulation of active power at terminals A and C, respectively. In the following sections, these inter-area modes in Grid A and Grid C are referred simply as λ_A and λ_C, respectively.

6.3.1. POD input-output signal selection

Geometric measures are used to find the most effective control loop for damping of the inter-area modes. Active power reference (P_{ref}) of the converters is the input signal while signals measured at the point of common coupling (PCC) by the phase locked loop (PLL) are considered as alternatives for output signals. These local signals are frequency (ω_{pll}), PCC voltage (v_{pcc}) and PCC voltage angle (θ_{pll}). The normalized geometric measure values of the possible input- output signal combinations are presented in Table 6-3. The control loop P_{ref}-θ_{pll} has the highest controllability/observability for the inter-area modes in Grid A and Grid C. Therefore, the PODs at both converter A and converter C have PCC voltage angle of the respective grids as stabilizing feedback signal.

Table 6-3: Normalized geometric measures (m_{co}) for inter-area modes in Grid A and C for different control loops

Grid	Eigenvalues	P_{ref} -ω_{pll}	P_{ref} - V_{pcc}	P_{ref} - θ_{pll}
Grid A	λ_A = -0.0417 ± j3.58	0.015	0.082	1
Grid C	λ_C = -0.1358 ± j3.11	0.002	0.564	1

6.3.2. POD interaction analysis

With the selected input-output signal combinations, the MIMO transfer function matrix, $G(s)$, becomes the two-by-two transfer function shown in Figure 6-6. The values of the transfer functions are presented in (6.9). The subscripts A and C refer to signals from Grid A and Grid C.

$$G(s) = \begin{array}{c} \\ \theta_{pll,A} \rightarrow \\ \theta_{pll,C} \rightarrow \end{array} \begin{array}{c} \begin{array}{cc} P_{ref,A} \downarrow & P_{ref,C} \downarrow \end{array} \\ \begin{bmatrix} g_{11}(s) & g_{12}(s) \\ g_{21}(s) & g_{22}(s) \end{bmatrix} \end{array}$$

Figure 6-6: Plant transfer function for the selected input-output signals

$$g_{11}(s)=\frac{\theta_{pll,A}(s)}{P_{ref,A}(s)}, \qquad g_{12}(s)=\frac{\theta_{pll,A}(s)}{P_{ref,C}(s)}$$
$$g_{21}(s)=\frac{\theta_{pll,C}(s)}{P_{ref,A}(s)}, \qquad g_{22}(s)=\frac{\theta_{pll,C}(s)}{P_{ref,C}(s)} \tag{6.9}$$

The diagonal elements $g_{11}(s)$ and $g_{22}(s)$ use local measurement signals and are the control loops that are selected using geometric measures in the previous section. The off-diagonal elements $g_{12}(s)$ and $g_{21}(s)$ entail the use of measurements from remote grids.

Figure 6-7 shows the magnitude of DRGA elements for the frequency range 1 to 10 rad/s. The vertical traces indicate the frequency of the critically damped inter-area modes, which are important frequencies for the performance of the POD. The RGA magnitudes for the diagonal elements of the transfer function matrix ($G(s)$), at the frequencies of interest, are around 1.4. This means that there is some interaction between the two POD input-output loops. An RGA number equal to one indicates no interaction with the other loop, while RGA different from one indicates some interactions. Large RGA elements (5-10 or larger) at frequencies important for control indicate that the plant is difficult to control due to strong interactions [93]. The DRGA magnitudes for off-diagonal pairing (i.e. using measurements from a remote grid) are less than 0.4. This suggests that with this pairing option, the effective closed loop gain would be more than twice the open loop gain. This can lead to instability. Moreover, the option to control a converter using remote measurements from another grid would require consideration of aspects, such as, (i) the time delay associated with remote signal transmission, and (ii) impact of the possible loss of the remote signal. These aspects are outside the scope of this work. Against this backdrop, off-diagonal pairings are not given further consideration.

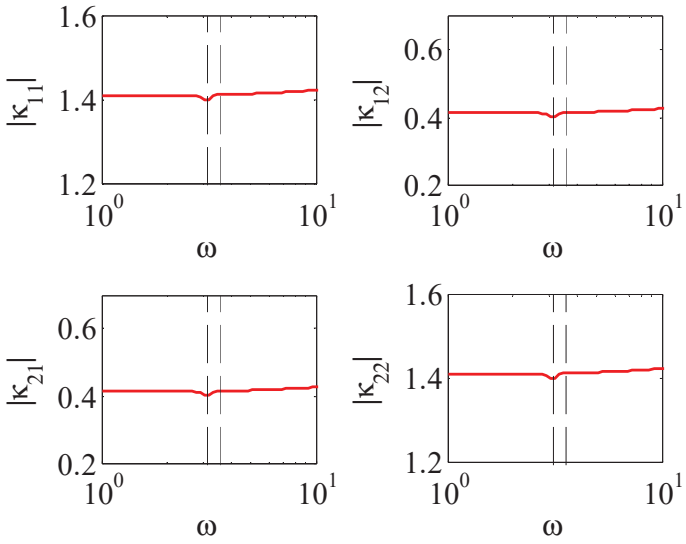

Figure 6-7: RGA numbers for the selected input-output (P_{ref}-θ_{pll}) pairings

As mentioned in Section 4.2, RGA indicates only the existence of interactions, while PRGA is also indicative of the extent of interactions. Figure 6-8 shows that as a result of interaction between the two control loops, the gain of $P_{ref,A}$ - $\theta_{pll,A}$ increases as γ_{12} is less than one while the gain of $P_{ref,C}$ - $\theta_{pll,C}$ decreases as γ_{21} is greater than one, when the two loops are closed. In other words, loop $P_{ref,C}$ - $\theta_{pll,C}$ enhances the effective gain of loop $P_{ref,A}$ - $\theta_{pll,A}$. On the other hand, loop $P_{ref,A}$ - $\theta_{pll,A}$ reduces the effective gain of $P_{ref,C}$ - $\theta_{pll,C}$. The diagonal elements of PRGA, γ_{11} and γ_{22}, are the same as the diagonal elements of the RGA. Since they have identical values, their curves in Figure 6-8 overlap.

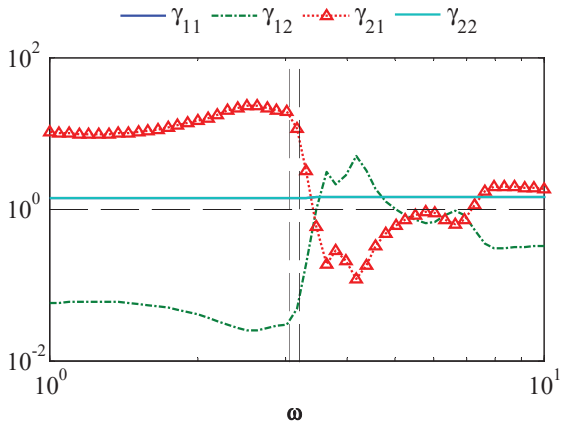

Figure 6-8: PRGA

6.3.3. Modal Analysis and POD insertions

Power oscillation damping controllers were added to Terminals A and C to damp the inter-area modes in their respective grids identified in Table 6-2. The POD tuning was performed according to the root locus method explained in section 6.2.2. Independent design approach is used to design the decentralized controllers. First, the two PODs were tuned individually to damp respective modes of interest, i.e. the POD on converter A was tuned without connecting the POD on Converter C, and vice versa. Then, both PODs were connected at the same time and interaction between the two control loops was analyzed. Table 6-4 shows the damping ratio of the inter-area modes for different cases of POD insertions.

Table 6-4: Insertions of POD and damping ratio of inter-area modes

Case No.	**Description**	λ_A	λ_C
		ζ [%]	ζ [%]
Case 1	No POD	1.18	4.35
Case 2	POD on A	11.16	4.32
Case 3	POD on C	1.17	9.61
Case 4	POD on A and C	14.75	6.01

The inter-area modes in Grid A and Grid C had damping ratios of 1.1% and 4.3%, respectively, without POD on the converters. Adding a POD on converter A with the appropriate phase shift and gain $K_{POD,A}$ =15 increases the damping ratio of the inter-area

mode in Grid A to 11.1%. Adding a POD only on Converter C with the appropriate phase shift and gain $K_{POD,C}$ = 0.1 improves the damping of the inter-area mode in Grid C from 4.3% to 9.6%. When both PODs on Converter A and on Converter C are used at the same time, the damping ratios of the inter-area modes in Grid A and C become 14.7% and 6%, respectively. This shows that due to the interaction between the two control loops, the effective gain of the POD on Converter A has increased, and the effective gain of the POD on Converter C has decreased, at the frequencies of interest, i.e. at the oscillation frequencies of the inter-area modes.

Figure 6-9 shows the movement of the inter-area modes in the complex plane for different cases of POD insertions at the MTDC terminal converters. Diamond markers indicate the position of λ_A, while triangle markers indicate the position of λ_C for Cases 1 to 4. Note that the No POD case or Case 1 markers overlap with some of the other markers as the position of λ_A is the same in Cases 1 and 3, while the position of λ_C is the same in Cases 1 and 2.

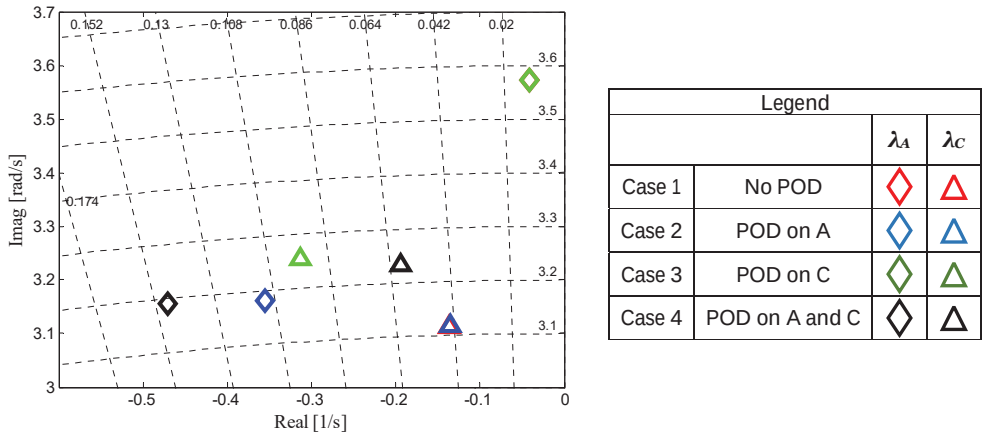

Figure 6-9 : Inter area modes in Grid A (diamond marker) and Grid C (triangle marker) for Cases 1 to 4

The findings from the eigenvalue analysis are corroborated by time domain analysis. A three-phase symmetric short circuit fault was applied at t=1s at Bus 27 in Grid C (see Figure 6-5). The rotor speed deviation for Gen11 in Grid C for three different cases analyzed is shown in Figure 6-10. Without POD installed on Converter C (dashed red curve), the speed of the generator has large oscillation following the fault occurrence. With POD on converter C only (dash-dot green curve), the oscillation has lower amplitude

and is damped out faster. However, when PODs are installed on both Converters A and C, the damping on the inter-area mode in Grid C is visibly reduced (solid black curve).

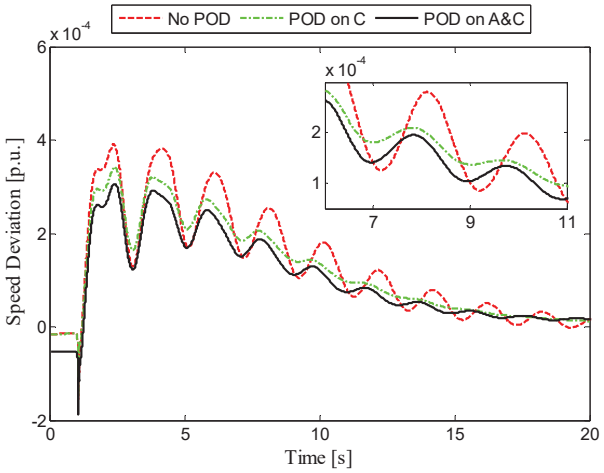

Figure 6-10: Speed deviation for Gen11 in Grid C

6.3.4.Sensitivities to POD tuning

To elaborate the interaction between the two controllers further, different cases of POD tunings presented in Table 6-5 were investigated and compared with the original tuning in Case 4. First, in Case 5, the gain for the POD on Converter A was reduced from 15 to 5, while keeping the gain for the POD on Converter C constant. Then, in Case 6, the gain for POD on Converter C was increased from 0.1 to 0.35, while keeping the gain for the POD on Converter A constant. The damping ratios of the inter-area modes in each grid before and after re-tuning the PODs are shown in Table 6-5.

Table 6-5: POD interactions for different tunings

	POD on A and C	**POD gains**	λ_A	λ_C
			ζ [%]	ζ [%]
Case 4	Original tuning	$K_{POD,A}$ =15, $K_{POD,C}$ = 0.1	14.75	6.01
Case 5	Tuning 1	$K_{POD,A}$ =5, $K_{POD,C}$ = 0.1	5.12	10.8
Case 6	Tuning 2	$K_{POD,A}$ =15, $K_{POD,C}$ = 0.35	8.16	17.63

The results in Table 6-5 are also clearly depicted in Figure 6-11 where the eigenvalues' movement in the complex plane are shown.

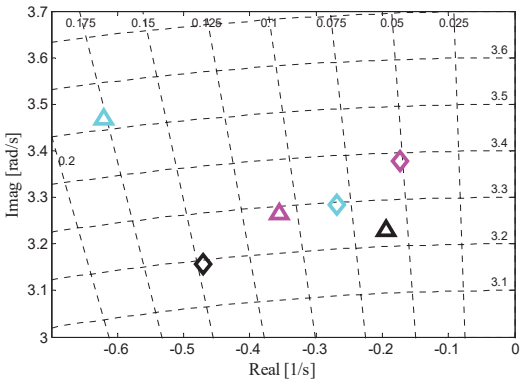

Legend			
		λ_A	λ_C
Case 4	Original tuning	◇	△
Case 5	Tuning 1	◇	△
Case 6	Tuning 2	◇	△

Figure 6-11: Inter area modes in Grid A (diamond marker) and Grid C (triangle marker) for Cases 4 to 6

It can be seen from Table 6-5 and Figure 6-11, that the damping ratio of the inter-area mode in Grid A decreases when the gain of the POD on Converter A is reduced or when the gain of POD on Converter C is increased. Contrarily, the damping ratio of the inter-area mode in Grid C increases when the gain of POD on Converter A is reduced or the gain of POD on Converter C is increased. These results are consistent with what was observed from the PRGA curve in Figure 6-8.

Figure 6-12 shows rotor speed deviation for Gen4 in Grid A. A three-phase symmetric short circuit fault was applied at t=1s at Bus 7. Without POD installed on either Converter A (dashed red curve), the speed of the generator experiences almost sustained oscillations following the fault. With POD on converter A only (dash-dot blue curve), the oscillations are well damped. However, when PODs are installed on both Converters A and C and tuned as in Case 6, the damping on the inter-area mode in Grid A is slightly reduced (cyan curve). Again, the interaction of the two controllers is evident.

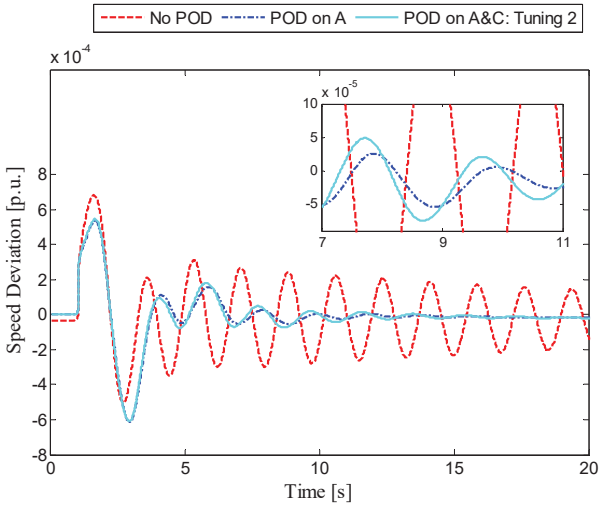

Figure 6-12 : Generator speed deviation for Gen 4 in Grid A

The results presented in this section clearly show undesired interactions between two POD controllers installed on different MTDC terminal converters. If there was a POD on the third terminal that is connected to Grid B, then the control loop interaction analysis would be the same as above, but the plant transfer functions for DRGA and PRGA would each be a 3x3 matrix.

6.4. Chapter summary

This chapter analyzed the interaction between POD controllers on an MTDC that interconnects several asynchronous ac grids. Geometric measures of controllability and observability were used to select the most effective input-output signal combinations for each POD controller. In addition, using RGA and PRGA measures, the interaction between POD controllers at two different terminal converters of an MTDC were assessed. Small-signal and time domain analyses carried out for a study case supported the findings of the frequency domain analysis, as given by the RGA and PRGA. For the analyzed study case, it was found that due to the interactions the performance of one of the controllers was augmented, while the performance of the other controller deteriorated. The analyses clearly show that control loop interaction should be considered while tuning PODs on converters even if they are connected to different grids.

7. Inertia and Frequency stability

Power system frequency is dependent on the balance between active power generation and load demand. Active power imbalance, which is caused by disconnection of large loads or generators, leads to deviation from the nominal frequency. The resulting frequency deviation is regulated by the actions of governors, which vary gate positions of turbines in order to change generated active power. When a power system has two or more generators with governors, the governors are provided with frequency droop characteristics to ensure stable operation. In recent times, the share of power from renewable energy sources (RES) such as wind, solar, small hydro, etc. has increased significantly. As these types of generation systems do not store primary energy resource, a power system with high penetration of RES will have low frequency containment reserve. Frequency Containment Reserve (FCR) is the operational (primary) reserves activated to contain system frequency after the occurrence of an imbalance [105]. In addition, the total inertia of the system becomes lower as most generators in RES are either power electronics interfaced or are small generators with low inertia. This has raised concerns regarding frequency stability of a synchronous system; particularly in periods of high power import through high voltage direct current (HVDC) links and/or high generation from power electronics interfaced power sources such as wind and solar generations.

Frequency stability refers to the ability of a power system to maintain the frequency within a nominal range, following a severe system upset that may or may not result in the system being divided into subsystems [22, 106]. It falls in the category of midterm to long term stability studies, where inter-machine synchronizing power oscillations are damped out, and the focus is on slower and longer duration phenomena that accompany large disturbances and result in large, sustained mismatches between generation and consumption of active and reactive power [72]. Frequency stability has dynamics ranging from tens of seconds to few minutes.

Provision of FCR and inertia through HVDC links and multi-terminal HVDC (MTDC) grids for mitigation of frequency stability problems is explored in [57, 59-61, 107-109]. It is achieved by changing the power flow at the terminal converter based on the change in ac grid frequency. Frequency reserve sharing through HVDC links has been implemented in some installations in Europe. The HVDC interconnector between the Netherlands and Great Britain, *BritNed*, is equipped with a frequency droop controller to support

frequency in Great Britain [110]. The pilot testing started in 2014 [111] and balancing power of ±100MW is transferred for frequency control on top of the market exchange [112]. The technical and economic investigation of trading primary frequency reserves between Western Denmark and Norway via *Skagerrak* HVDC interconnectors is underway [113], while there already exists a five years agreement for delivery of ±100 MW secondary control power with a matching 100 MW capacity reservation on the *Skagerrak 4* link [114].

The following sections in this chapter are organized as follows. An overview on frequency reserve sharing through HVDC links and MTDC grids is given in Section 7.1. Global analysis of frequency stability for two ac grids connected through an HVDC link is presented in Section 7.2. A coordinated control for MTDC converters is proposed in Section 7.3 to improve global frequency stability in hybrid ac/dc power systems. Conclusions from this chapter are given in Section 7.4. The analyses and results presented in this chapter have been published in [115, 116].

7.1. AC grid frequency support through HVDC transmission systems

7.1.1. HVDC systems interconnecting ac grids

In HVDC link interconnecting two ac grids, one terminal controls dc voltage while the other terminal controls active power. If the HVDC participates in ac grid frequency regulation, then the controller of the active power-controlling terminal is modified to include frequency deviation signal, and its outer loop control structure becomes as shown in Figure 7-1.

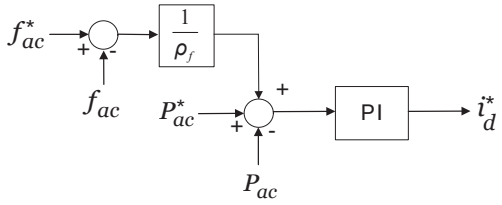

Figure 7-1 : Control structure for frequency droop controller

where ρ_f is frequency droop, P_{ac} is active power flowing into the grid and f_{ac} is ac grid frequency. The superscript * indicates reference signals. ρ_f is the percentage of change ac grid frequency to percentage of change in active power flow in the HVDC. When ac grid

frequency decreases (i.e. the load demand is higher than generated power), the controller increases power flow into the ac grid, and vice versa.

If a derivative controller is used together with a proportional controller, then the controller would act not only the error between measured and reference frequency signals but also on the rate of change of the error. With this controller, frequency support is also provided during the transient period, which is the characteristics of inertia. Here, a phase lead controller is proposed for frequency and inertia support from HVDCs. A phase lead controller is basically a proportional-derivative (PD) controller with a filter and has the form:

$$C(s) = K\left(\frac{1+T_1 s}{1+T_2 s}\right) \tag{7.1}$$

where $T_1 > T_2$. The controller introduces a positive phase to a system between the corner frequencies $\omega_1=1/T_1$ and $\omega_2=1/T_2$. The maximum amount of phase, ϕ_m, is added at the geometric mean of the two corner frequencies, which is called the center frequency (ω_m). ω_m and ϕ_m are calculated as:

$$\begin{aligned} \omega_m &= \frac{1}{T_2\sqrt{(T_1/T_2)}} \\ sin\,\phi_m &= \frac{(T_1/T_2)-1}{(T_1/T_2)+1} \end{aligned} \tag{7.2}$$

Depending on the value of T_1/T_2, up to 90° phase can be added using a single phase-lead controller. The controller improves stability by improving the phase margin of a system. With proper tuning, the controller increases system damping, and decreases rise time and settling time [117].

The block diagram of the modified HVDC frequency controller with the phase lead controller is shown in Figure 7-2. The controller improves the transient behavior and stability of ac grid frequency. Note that the steady state behavior of the ac frequency remains the same as the frequency droop controller if K in (7.1) is equal to $1/\rho_f$.

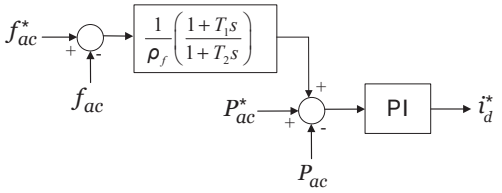

Figure 7-2 : Frequency controller with inertia support

The control structure for an MTDC terminal converter that participates in ac grid frequency regulation is similar to that of an HVDC converter. If the MTDC is being operated in dc voltage droop control mode, then a frequency droop controller is included in addition to the dc voltage droop as shown in Figure 7-3. This leads to sharing of primary frequency reserves among different synchronous grids that are connected through the MTDC grid. All ac grids connected to the MTDC grid respond to frequency deviation in one grid. The final steady state frequency of each grid will have some amount frequency error which can be removed by a secondary frequency controller [61].

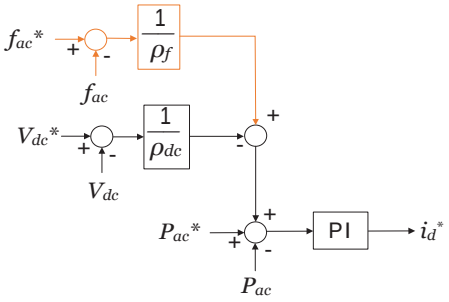

Figure 7-3 : Frequency and dc voltage droop control

7.1.2. Onshore grid frequency support from offshore wind farms

When an offshore wind farm is connected to an onshore ac grid through a dc transmission system, the offshore terminal converter determines wind farm's collection grid voltage and frequency. During normal operation, the wind turbines are controlled in such a way that they are operating at an optimal speed; extracting maximum possible power from the available wind. However, when wind turbines provide onshore frequency and/or inertia support, auxiliary controllers are introduced to the wind turbine converter controllers so

that the turbines change their power output depending upon change in onshore grid frequency. It should be noted that this entails non-optimal or curtailed operation of a wind farm.

As the dc transmission decouples the frequency of onshore grid and offshore wind farm grid, the offshore wind turbines can not sense the change in onshore frequency. Rather, auxiliary converter controllers and/or communication system are used to convey the frequency deviation signal across the dc system. The different methods proposed in the literature to signal onshore frequency deviation to offshore wind turbines can broadly be categorized into three. The first method requires additional controllers on both onshore and offshore terminal converters and uses change in dc voltage as a signaling medium [107, 108, 118]. The second method requires additional controller only on the offshore terminal converter and uses a communication system to transmit onshore frequency change signal to the offshore terminal converter [109]. The third method proposes use of communication system to send onshore frequency measurement directly to offshore wind turbines [118, 119]. The work in this thesis focuses on coordinated control of MTDC converters for improved system frequency support from offshore wind farms. For this reason, a brief review of the first two types of onshore grid frequency deviation signaling methods are presented in the following sub-sections. The two methods produce different results if the dc transmission is an HVDC or an MTDC. To highlight the difference, the methods are explained in the context of offshore wind farm connected to an onshore grid through an HVDC and an MTDC.

7.1.2.1. HVDC connected offshore wind farms

Figure 7-4 shows an HVDC link connecting an offshore wind farm to an onshore grid. A schematic of the converters' control structure is depicted in the figure. The onshore side HVDC converter controls dc link voltage, while the offshore side converter determines the frequency and ac voltage for the offshore wind farm collection grid.

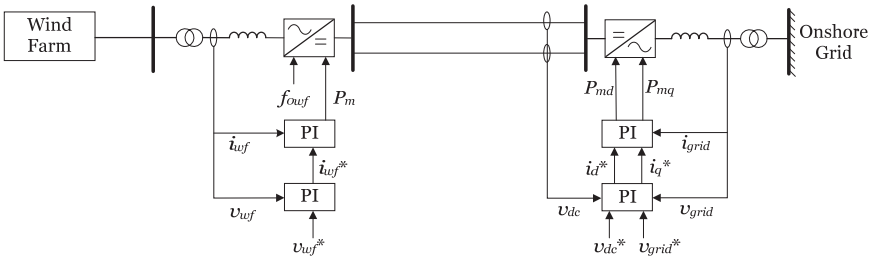

Figure 7-4 : HVDC connected offshore wind farm [109]

If the offshore wind farm is to participate in frequency regulation of the onshore grid, then auxiliary controllers are added to both the onshore and offshore side HVDC converters. These auxiliary controllers are shown in Figure 7-5. f_{ac}, V_{dc} and f_{owf} represent onshore ac grid frequency, dc link voltage and offshore wind farm collection grid frequency, respectively. ρ_f and $\rho_{dc,owf}$ represent frequency droop and dc voltage droop constants, respectively. The superscript * indicates a reference signal. When a frequency deviation occurs in the ac grid, then the onshore side auxiliary controller in Figure 7-5 (a) changes dc link voltage. The offshore side auxiliary HVDC controller in Figure 7-5 (b) will then change offshore grid frequency according to the change in dc link voltage.

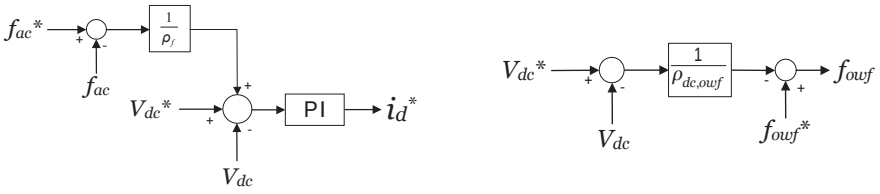

(a) (b)

Figure 7-5 : Auxiliary VSC-HVDC converter controllers on (a) onshore grid side and (b) offshore wind farm side

Alternatively, a communication system can be used to directly transfer onshore frequency signal to the offshore HVDC converter controller as shown in Figure 7-6. $\rho_{f,owf}$ represent frequency droop constant of the offshore converter controller. With this method, the onshore side HVDC converter controls dc link voltage to a constant value, while the offshore side HVDC converter controller changes the offshore frequency (thereby wind

farm's output) based on onshore frequency deviation. The communication system introduces some delay in response time. To compensate for the delayed response, [109] proposes the use of energy stored in dc link capacitors for frequency regulation during communication latency period.

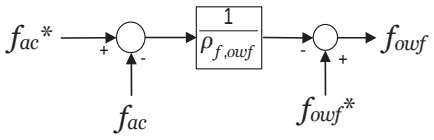

Figure 7-6 : Offshore wind farm side converter controller for frequency sent over a communication system

From the perspective of the ac grid, the control methods described above, i.e. using dc voltage change or communication system as a signaling medium, produce the same result except for the delay. As the wind farm is connected to only one onshore ac grid, all the power produced by the wind farm flows into that grid, and any power flow change at the wind farm terminal is also reflected as a change in power flow into the ac grid. However, the two control methods produce different results if the wind farm is connected to several ac grids through an MTDC.

7.1.2.2. MTDC connected offshore wind farms

When an offshore wind farm is connected at one of MTDC terminals, then the wind farm connected terminal controls the wind farm's collection grid voltage and frequency (similar to the case of HVDC) allowing the wind farm to inject all its power production into the dc grid. If the wind farm is to participate in onshore frequency regulation, then converter control structure of the offshore wind farm terminal and the terminal(s) connected to onshore grids that are receiving the frequency support are modified as shown in Figure 7-7.

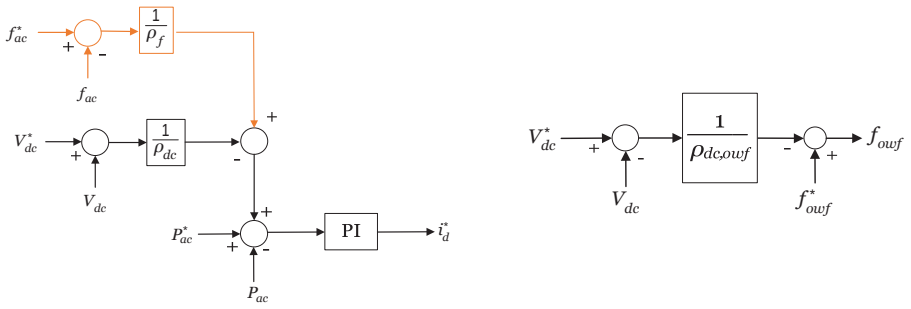

(a) (b)

Figure 7-7 : Auxiliary MTDC converter controllers on (a) onshore grid side and (b) offshore wind farm side

where f_{grid}, V_{dc}, P_{ac} and f_{owf} are onshore ac grid frequency, dc link voltage, active power into ac grid and offshore wind farm collection grid frequency, respectively. The superscript * indicates reference signal. By using both frequency and dc voltage droop control, change in onshore grid frequency is counteracted by a change in power flow at the onshore grid terminal. This power flow change causes active power imbalance in the dc grid and leads to change in dc grid voltage. MTDC terminals operating in dc voltage droop control mode, and the offshore wind farm terminal change their power flow to remove dc grid power imbalance and regulate dc voltage. Hence, the onshore grid receives frequency support through the dc grid. It should be noted that the actual power support comes both from the offshore wind farm and the other ac grids connected to the MTDC whose terminals are operating in dc voltage droop control mode.

If a communication system is used to send ac grid frequency directly to an offshore wind farm's terminal converter, then the change in wind farm's power output would be considered as a dc grid power imbalance, and all terminals operating in dc voltage droop would react to remove the imbalance. This means, the additional power output from the wind farm not only flows into the ac grid experiencing a frequency disturbance but also flows into the other ac grids. This is different from using communication in an HVDC link where the power from wind farm flows only to a single onshore grid.

In section 7.3, a coordinated converter strategy for MTDC converters is proposed that uses both change in dc grid voltage and a communication system as a medium to communicate onshore frequency disturbance to an offshore wind farm.

7.2. Global analysis of frequency stability

In the literature, the technical feasibility of frequency reserve sharing strategies is demonstrated through isolated analysis limited to a single synchronous grid with a focus on the frequency of the grid under study. However, in a global system where several asynchronous grids are connected through an HVDC system, frequency reserve sharing will also affect the frequency of other synchronous zones, which may or may not experience lack of frequency reserve and/or inertia. Therefore, it is important to carry out a global analysis that considers the entire hybrid ac/dc power system, which includes all asynchronous power systems.

In this section, a global analysis of frequency stability is carried out by not only studying the grid that is receiving frequency support, but also the grid providing the support. Furthermore, the analysis focuses on dynamics that are in the range of seconds to several minutes, i.e. both electromechanical and governor (frequency) stability are studied in detail in all ac grids in the hybrid ac/dc power system. Modal and non-linear time domain analyses are used in the study and interactions between the ac grids are identified.

A power system with two asynchronous ac grids interconnected via an 800 MW HVDC link is used for global analysis of frequency stability and inertia. A single line diagram of the study system configuration is presented in Figure 7-8. Grid A is a large power system with four generators and long 230 kV transmission lines. It is based on the two area system presented in [72]. Grid B, which is based on a power system presented in [71], is a nine bus power system with three generators and three loads. All generators in the study system have HYGOV and SEXS types of hydro governor/turbine and excitation system models, respectively. In addition, the exciters in Grid A are equipped with STAB1 type of power system stabilizers (PSS) for damping local and inter-area oscillations. DIgSILENT *PowerFactory* is used for the simulation studies.

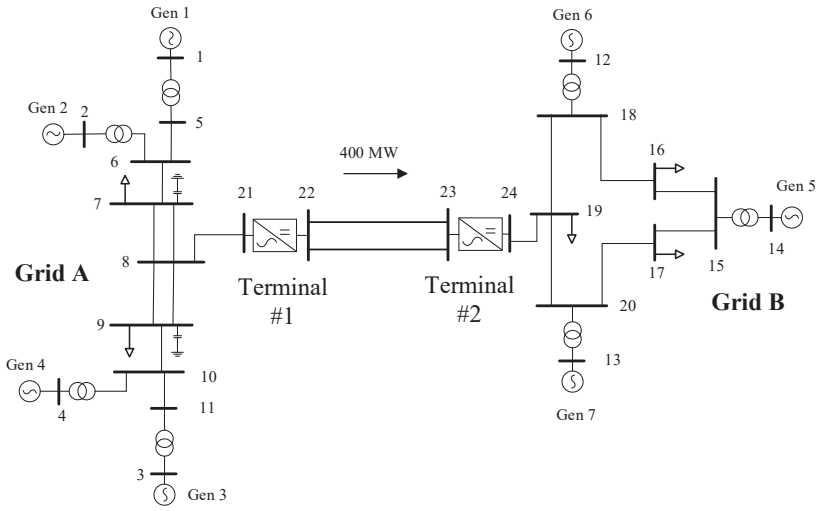

Figure 7-8 : Study system

The converter controllers at Terminal #1 are operating in dc voltage and reactive power control, while three converter control scenarios are considered for converter controllers at Terminal #2. In the first scenario, Case 1, the converter operates in constant active power control mode and does not participate in frequency control. This case is used as a base case to compare the change in frequency stability and system inertia when the HVDC is involved in frequency control. In the other two scenarios, Case 2 and Case 3, Terminal #2 converter controllers provide frequency support to Grid B. In Case 2, frequency control with droop (Figure 7-1) is used, and in Case 3 both inertia support and frequency support are provided by the converter controller (Figure 7-2). Table 7-1 summarizes the different converter control strategies used in the outer loop d-axis control for the different cases. In all case scenarios, the outer q-axis controller of Terminal #1 and #2 are set to constant (zero) reactive power control.

Table 7-1 : Terminal converter d-axis control for different studied cases

Cases	**Terminal #1**	**Terminal #2**
Case 1	Constant V_{dc} control	Constant P control and
Case 2	Constant V_{dc} control	P control with frequency droop (ρ_f = 20%)
Case 3	Constant V_{dc} control	P control with frequency droop (ρ_f = 20%) and inertia

The different cases are studied using linear and time domain analyses. The study evaluates and compares the performance of the controllers, and assesses the electromechanical and frequency stability of both Grid A and B. The initial steady state power flow is 400 MW flowing from Grid A to Grid B. An HVDC frequency droop constant of ρ_f = 20% was used both in Case 2 and 3. ρ_f has a Hz/MW unit and is based on the rating of the converter.

7.2.1. Linear analysis

A linear analysis for the study system was carried out for the three different converter control cases at Terminal #2. The aim of this linear analysis is to investigate how the dynamics of the ac systems are affected when an HVDC participates in ac frequency control. The focus is on low frequency electromechanical and governor (frequency) oscillation modes. Electromechanical oscillations are due to oscillations of rotating masses of generators that occur following a disturbance, while frequency oscillations are due to the slow actions of governors following an active power imbalance. The electromechanical and governor modes for the studied system were identified from the participation factors of the modes and are listed in Table 7-2.

Table 7-2 : Electromechanical and governor (frequency) modes for the three case studies

Case study	Eigenvalues	f [Hz]	ζ [%]	
Case 1 No HVDC frequency support	-0.23 ± j2.80	0.45	8	Electromechanical modes in Grid A
	-0.92 ± j6.37	1.01	14	
	-0.91 ± j6.13	0.98	15	
	-1.02 ± j10.39	1.65	10	Electromechanical modes in Grid B
	-1.32 ± j11.53	1.83	11	
	-0.84 ± j2.78	0.44	29	
	-0.06 ± j0.16	0.03	32	Grid A governor mode
	-0.11 ± j0.40	0.06	27	Grid B governor mode
Case 2 HVDC frequency droop support	-0.23 ± j2.80	0.45	8	Electromechanical modes in Grid A
	-0.92 ± j6.37	1.01	14	
	-0.91 ± j6.13	0.98	15	
	-1.02 ± j10.39	1.65	10	Electromechanical modes in Grid B
	-1.33 ± j11.53	1.83	11	
	-0.75 ± j2.72	0.43	26	
	-0.06 ± j0.16	0.03	32	Grid A governor mode
	-0.14 ± j0.40	0.06	33	Grid B governor mode
Case 3 HVDC frequency and inertia support	-0.23 ± j2.80	0.45	8	Electromechanical modes in Grid A
	-0.91 ± j6.37	1.01	14	
	-0.91 ± j6.13	0.98	15	
	-1.02 ± j10.39	1.65	10	Electromechanical modes in Grid B
	-1.34 ± j11.53	1.84	12	
	-0.33 ± j2.73	0.43	12	
	-0.06 ± j0.16	0.03	32	Grid A governor mode
	-0.16 ± j0.41	0.06	36	Grid B governor mode

The governor mode of Grid B has 0.06 Hz frequency. The phase-lead controller parameters in Case 3 were selected in such a way that the center frequency for the controller is close to the frequency of this mode. Therefore, T_1 and T_2 in Eq. (7.2) were set to 10s and 1s, respectively. This is equivalent to a maximum phase boost of 54.9° at center frequency of 0.32 rad/s (0.05 Hz).

The governor mode in Grid A has damped frequency of 0.03 Hz with 32% damping ratio. Neither electromechanical nor governor modes in Grid A change their position in all three cases of converter controllers implement for the HVDC. They remain unaffected.

The frequency controller is added to controller of Terminal #2, which is the terminal connected to Grid B. Therefore, Grid B receives frequency and inertia support from Grid A through the HVDC, as corroborated by the modal analysis result. The damping ratio of governor (frequency) mode of Grid B changes depending on the type of converter control used. When no frequency support was provided, i.e. Case1, the mode had a damping of 27%, while when a frequency droop control was used in Case 2, its damping increased to 32%. In Case 3, where frequency and inertia support is included, the damping ratio of the mode increased further to 36%. The change is only in the real part of the mode and its imaginary part (frequency) does not change. This means that when HVDC is involved in frequency support for the tuning used, the governor mode shifts to the left on the real-imaginary plane improving its damping; as intended.

Even though the frequency control loop in the HVDC improves damping of the governor (frequency) mode in Grid B, it reduces damping of other modes in the grid. One of the electromechanical modes in Grid B (-0.84 ± j2.78), which is an inter-area mode between Gen6 and Gen7, became less stable in Case 2 and 3 compared to Case 1. In Case 1, the mode had a damping ratio of 29% while in Case 2 and Case 3, the damping ratio reduced to 26% and 12%, respectively.

From the modal analysis study, it can be concluded that the frequency controllers improve the frequency stability of Grid B but reduce the damping of the inter-area mode in the grid (especially the frequency controller with inertia support). The type of frequency controller implemented in the HVDC does not have any effect on the modes in Grid A.

7.2.2. Time domain analysis

Two non-linear time domain simulations were run for the three cases of converter controls studied. A load disturbance was used to study frequency stability, and short circuit fault in Grid B was used to assess the interaction between the frequency controllers and the electromechanical dynamics of the generators identified by the modal analysis.

Loss of load in Grid B

A 10% load loss (70 MW) in Grid B at Bus 17 was simulated at t=1s. Immediately after the load loss, the frequency in Grid B is disturbed due to an imbalance between generated power and consumed load. Grid A and Grid B frequencies under the three converter control scenarios are shown in Figure 7-9.

In Case 1, where no frequency control is used in the HVDC, only governors regulate the grid frequency. Governors' actions are slow because of the large physical time constants of the turbines. It takes 40 seconds until the frequency is stabilized. The maximum frequency in Grid B after the load loss reaches up to 50.5 Hz. When the HVDC is involved in frequency support, then the maximum deviation is reduced and becomes 50.3 Hz and 50.2 Hz in Case 2 and Case 3, respectively. Since the droop constants are the same in both cases, i.e. 20%, the steady state value of the frequency after the disturbance is also the same. It is clear from the low peak and limited rate of change of frequency following the load loss in Case 3 that Grid B receives an inertia support Grid A.

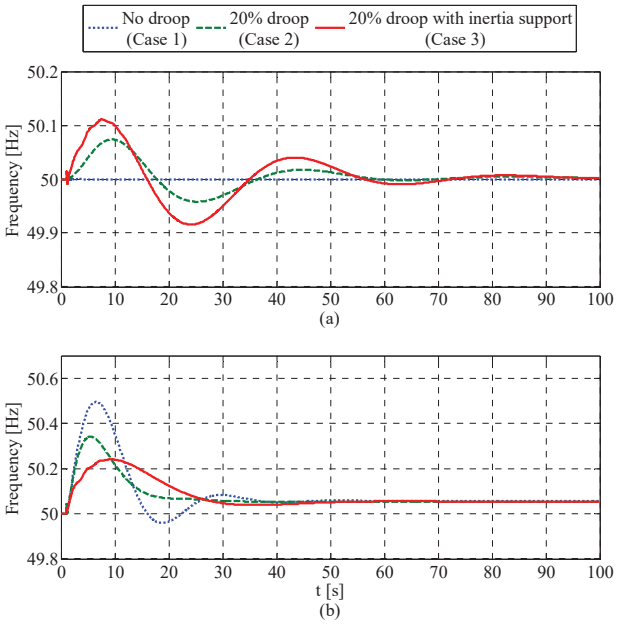

Figure 7-9 : Frequency responses in (a): Grid A and (b): Grid B

Since the power needed to support Grid B frequency is coming from Grid A, the frequency in latter grid gets disturbed as shown in Figure 7-9(a). The disturbance is larger in Case 3 than Case 2 because the power support provided by the grid is larger and faster (see Figure 7-10). Even though the frequency oscillations in Grid A are larger in Case 3 compared to Case 2, the damping of the oscillations is the same for both cases. The type of frequency control applied in Terminal #2 has no adverse effect on the frequency stability of Grid A.

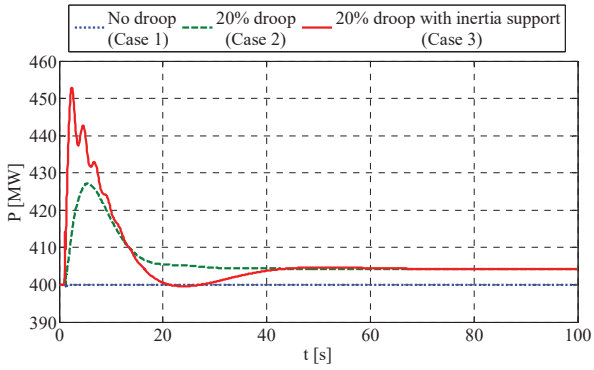

Figure 7-10 : Active power transferred from Grid A to B through the HVDC

Short circuit in Grid B

In order to study specifically the impact the different frequency controllers have on the electromechanical modes, a complete short circuit fault at Bus 18 in Grid B lasting for 100ms was simulated for Case 2 and Case 3. Figure 7-11 shows speed curves of generators in Grid A (Gen 1-4) and Grid B (Gen 5-7). The generators in Grid B accelerate until the fault is cleared. In Case 2, the electromechanical modes in both grids are highly damped. On the other hand, in Case 3, a poorly damped mode is clearly visible in Grid B. The frequency of the oscillation of the speed curves (ca. 0.43Hz) is close to the mode that was identified in the modal analysis (-0.33 ± j2.73) to be less stable in Case 3. The mode was also found to have high observability in Gen1 and Gen2 speed state variables. The oscillation frequency of Grid A generators' speed is 0.45 Hz. Since the poorly damped mode in Grid A (-0.23 ± j2.80) also has a similar damped frequency, i.e. 0.45 Hz, it is not possible to point out the contribution of Grid B inter-area mode (-0.33 ± j2.73) in speed oscillations of Grid A generators in Case 3. It is highly likely that the oscillations observed in Grid A in Case 3 are due to higher excitation inter-area mode of the grid caused by the higher power transfer (which can be considered as a sudden power change disturbance)

between the two grids. In general, the interaction between the two grids is higher in Case 3.

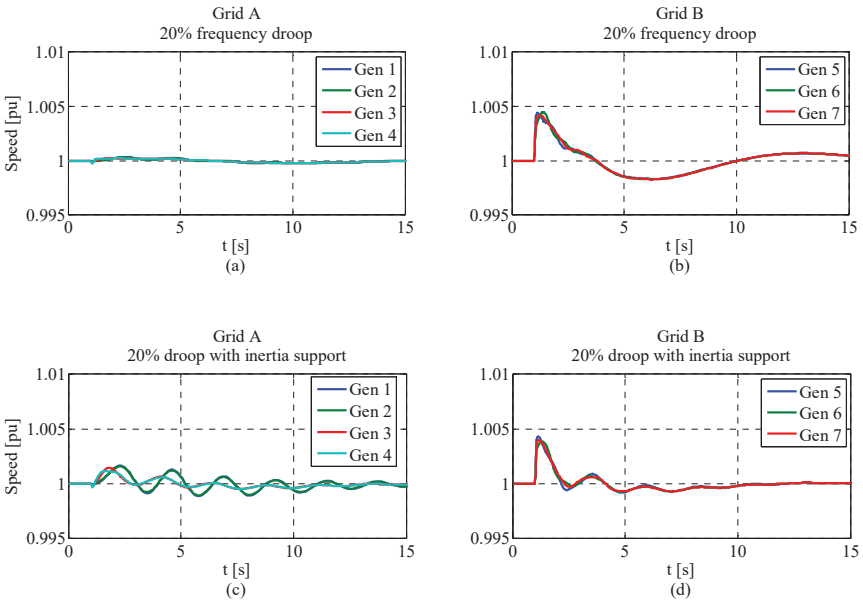

Figure 7-11 : Frequency responses in Grid A and Grid B for Case 2 ((a) and (b)) and Case 3 ((c) and (d))

In conclusion, this section presented a global analysis of frequency stability and inertia in the context of two ac systems connected with an HVDC. Emphasis was given to the dynamic behavior of both ac grids under different types of frequency and inertia support from HVDC converters. For the considered case studies, it was found that the frequency controllers perform as expected and improve the frequency stability of the grid receiving the support, and did not have any adverse effect on the dynamics of the grid providing the support. However, the electromechanical stability of the frequency support-receiving grid was found to be reduced especially when frequency controller with inertia was used.

7.3. Coordinated control of MTDC converters in hybrid AC/DC grids

In this section, a coordinated converter control strategy for MTDC converters is proposed that uses both change in dc grid voltage and a communication system as a medium to communicate onshore frequency disturbance to an offshore wind farm. The control strategy uses frequency and dc voltage droop at an onshore terminal and, at the same time,

sends onshore ac grid's frequency to the offshore wind farm terminal using a communication system. Figure 7-12 shows the control structures for onshore and offshore converters under the proposed coordinated control strategy.

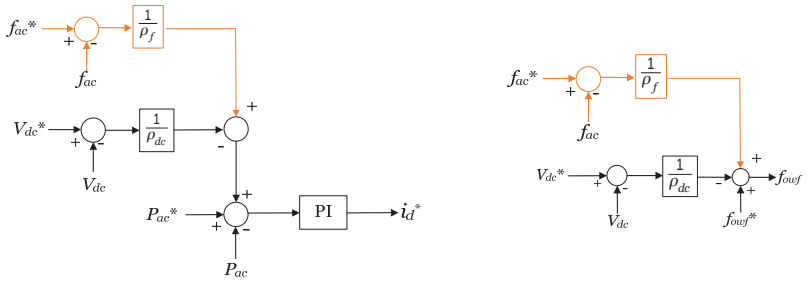

(a) (b)

Figure 7-12 : Auxiliary MTDC converter controllers on (a) onshore grid side and (b) offshore wind farm side

If a frequency disturbance occurs in the onshore grid, the power demanded by the onshore converter changes as the frequency error becomes different from zero. At the same time, the offshore wind farm's collection grid frequency is changed according to the frequency deviation of the onshore ac grid: signal sent over communication system. With this control strategy, dc grid power imbalance due to the change in power demand of the onshore converter terminal is counterbalanced by the change in power output of the offshore wind farm. This means dc grid voltage variation is reduced and, therefore, the participation of other MTDC converters (operating in dc voltage droop control) in dc voltage would be limited. This effectively means most of the FCR support provided through the dc grid comes from the offshore wind farm. This is further illustrated below through case studies. The different case studies demonstrate the effectiveness and limitations of the proposed coordinated MTDC converter control strategy.

Consider a three terminal VSC-MTDC grid connected to two asynchronous ac grids and an offshore wind farm as shown in Figure 7-13. Both onshore ac grids have multiple synchronous machines equipped with governors, automatic voltage regulators and power system stabilizers. Wind turbines and internal collection grid of the offshore wind farm are not modelled in detail. Instead, a stiff bus was used behind the offshore converter terminal to represent the wind farm. This is considered sufficient for the study as the focus is on the coordination of MTDC converter controllers. Furthermore, it is assumed that the wind turbines respond immediately and no delay was considered for communicating

onshore frequency signal to wind farm converter terminal. DIgSILENT *PowerFactory* was used for the simulation studies. During the initial steady state conditions, the wind farm was producing 600 MW. Grid #1 imports 400 MW while Grid #2 imports the remaining power (minus dc grid losses).

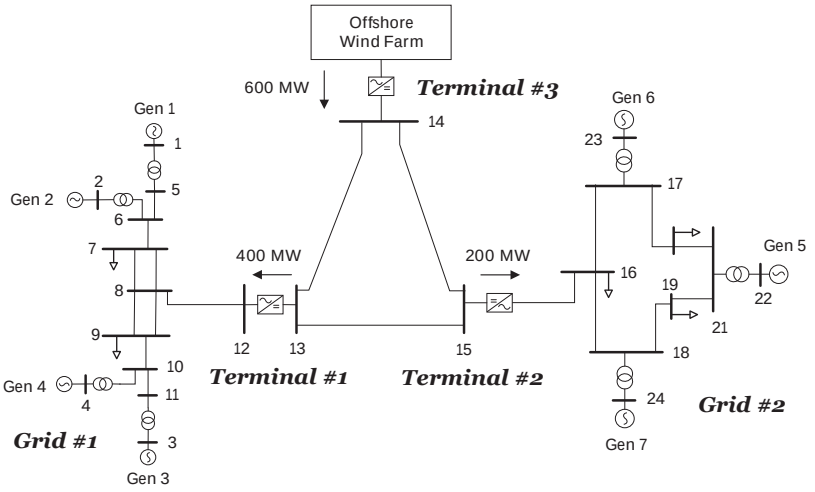

Figure 7-13 : Study system

Four different cases were studied and compared with each other. Table 7-3 lists types of converter controls used in each case at each MTDC terminal of the study system.

Table 7-3. List of study cases

	Terminal #1	Terminal #2	Terminal #3
Case 1	Frequency + Vdc droop	Vdc droop	Vdc as freq. change signal
Case 2	Frequency + Vdc droop	Vdc droop	Vdc droop + Frequency signal via communication
Case 3	Frequency + Vdc droop	Frequency + Vdc droop	Vdc as freq. change signal
Case 4	Frequency + Vdc droop	Frequency + Vdc droop	Vdc droop + Frequency signal via communication

In Case 1 and Case 2, only Grid #1 receives frequency support from the offshore wind farm through the dc grid, while in Case 3 and Case 4 both Grid #1 and Grid #2 receive frequency support from the offshore wind farm through the dc grid. In Case 1 and Case 3, the offshore wind farm changes its output to give frequency support to an onshore grid based on change in the dc grid voltage (Figure 7-7 (b)). In Case 2 and Case 4, the controller in Figure

7-12 (b) is used at the offshore wind farm terminal. Thus, the wind farm changes its output based on both change in dc grid voltage and change in Grid #1 frequency (that is sent via communication channel).

Loss of load in Grid #1 and Grid #2 were simulated to cause a frequency disturbance in the grids and study the performance of the proposed coordinated control strategy.

7.3.1. Single grid receiving frequency support: Case 1 and Case 2

Loss of load in Grid #1

Loss of load in Grid #1 causes power imbalance in the grid leading to increase in frequency. In order to control the frequency, the governors act to make the synchronous generators reduce their power output. At the same time, Terminal #1 converter controller reduces the power flowing from the dc grid into Grid #1. This leads to power imbalance in the dc grid and increase in dc voltage level, which is picked up by converters at both Terminal #2 and #3. Both terminals will try to regulate the dc voltage by changing converter power flows. Terminal #2 takes in more power from the dc grid, while Terminals #3 injects less power into the dc grid. Figure 7-14 shows Grid #1 and Grid #2 frequencies after the load disturbance for Case 1 and Case 2.

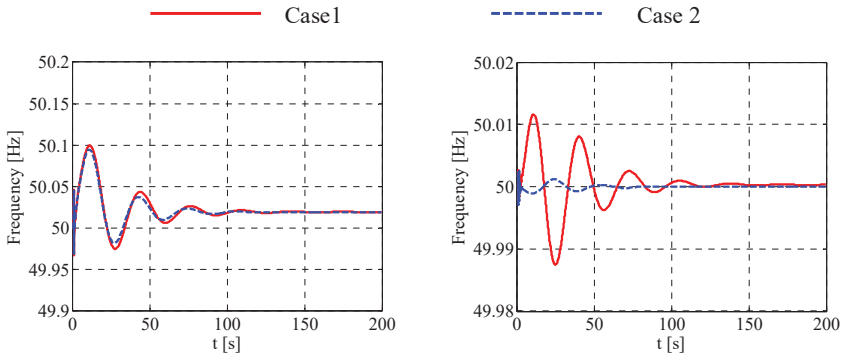

(a) Grid 1 Frequency (b) Grid 2 Frequency

Figure 7-14 : Frequency in Grid #1 and #2 for Case 1 and Case 2 for loss of load in Grid #1

The frequency disturbance in Grid #1, where the load loss has occurred, is similar for both cases. However, the frequency disturbance in Grid #2 is significantly reduced in Case 2 than in Case 1. This is because in Case 1 the frequency support to Grid #1 comes not only from the wind farm but also from Grid#2; which participates in dc grid voltage regulation and indirectly shares the frequency support duty according to its dc voltage droop setting.

Therefore, the control actions of Terminal #2 converter causes a frequency disturbance in Grid#2, which is eventually regulated by the governors in the grid. On the other hand, in Case 2, by communicating Grid #1 frequency directly to Terminal #3, the reduction in wind farm's power output is higher compared to Case 1. Thus, the wind farm contributes most of the power needed to regulate the frequency in Grid #1 and the power flow at Terminal #2 remains almost unchanged. The change in power output from the wind farm is higher for Case 2 than Case 1 as shown in Figure 7-15 (a). This is reflected in Grid #2 frequency for Case 2 in Figure 7-14 (b). In addition, the disturbance in dc grid is voltage is reduced in Case 2 compared to Case 1, see Figure 7-15 (b).

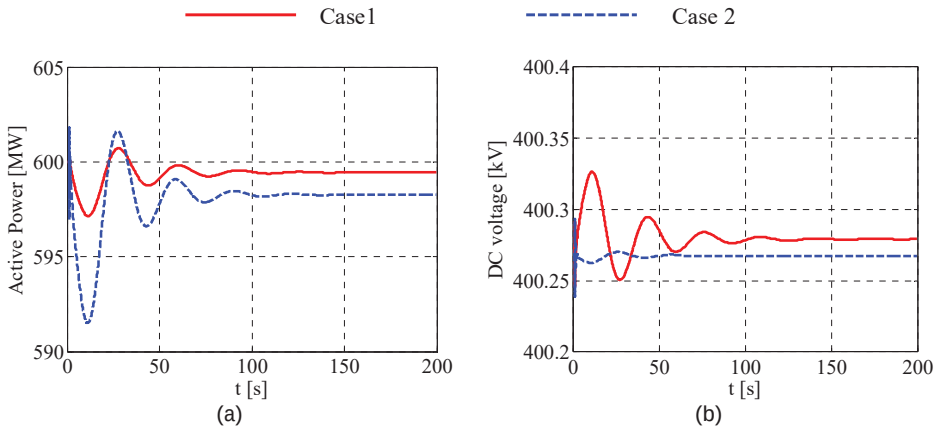

Figure 7-15 : Wind farm power output in Case 1 and Case 2 for loss of load in Grid #1

Loss of load in Grid #2

Since MTDC converter at Terminal #2 is operating only in dc voltage droop control mode in Case 1 and Case 2, neither the wind farm nor Grid #1 participate in frequency regulation of Grid #2. Only governors of the synchronous generators regulate any frequency disturbance in the grid. Figure 7-16 presents frequency in Grid #1 and Grid #2 for a loss of load in Grid #2. For both Case 1 and Case 2, the governors in the grid regulate the frequency of Grid #2, and the frequency in Grid #1 remains undisturbed.

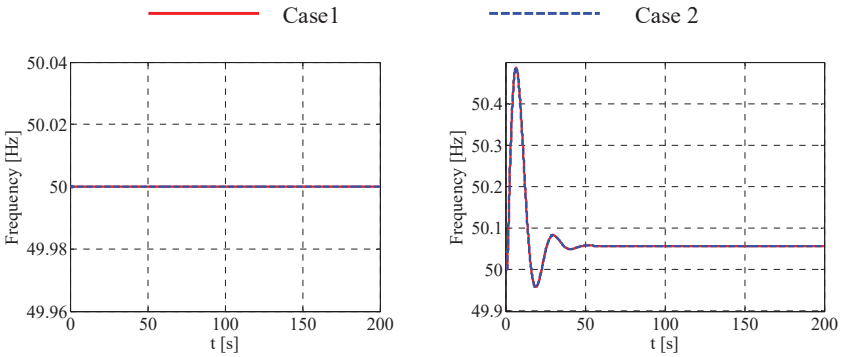

(a) Grid #1 Frequency (b) Grid #2 Frequency

Figure 7-16 : Frequency in Grid #1 and #2 for Case 1 and Case 2 for loss of load in Grid #2

From the results above, it can be concluded that the proposed coordination between converter controllers improves frequency support from an offshore wind farm when a single ac grid in the MTDC receives frequency support. The frequency support from the offshore wind farm is maximized and the extent of frequency disturbance in other ac grids connected to the MTDC is reduced significantly.

7.3.2. Multiple grids receiving frequency support: Case 3 and Case 4

In Case 3 and Case 4, both Grid #1 and Grid #2 receive frequency support from the offshore wind farm. Therefore, the converter controllers at Terminals #1 and #2 operate both in frequency droop and dc voltage droop control mode. In Case 3, the converter controller at Terminal #3 changes offshore grid frequency in proportion to change in dc voltage, while in Case 4, Terminal #3 receives Grid #1 frequency directly via a communication system. Again, loss of load in Grid #1 and Grid #2 are simulated for these two cases.

Loss of load in Grid #1

Frequency plots, after a loss of load in Grid #1, for the two ac grids is presented in Figure 7-17. The results show that when the MTDC converter controllers are coordinated (Case 4), the frequency support from the offshore wind farm is higher than Case 3 and unintended frequency disturbance in Grid #2 is avoided. This is similar to the results from Case 1 and Case 2 for load disturbance in Grid #1.

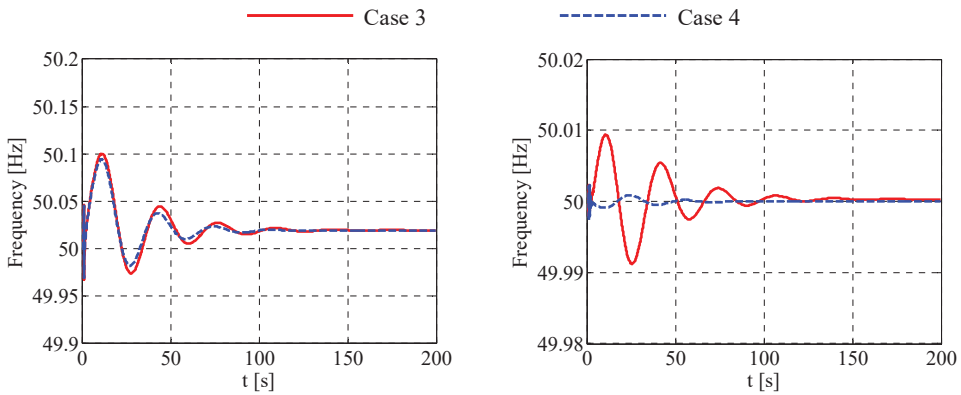

(a) Grid 1 Frequency (b) Grid 2 Frequency

Figure 7-17 : Frequency in Grid #1 and #2 for Case 3 and Case 4 for loss of load in Grid #1

Loss of load in Grid #2

If there is a frequency disturbance in Grid #2, both Terminal #1 (Grid #1) and Terminal #3 (wind farm) change their power flow and participate in the frequency regulation of Grid #2 alongside the governors in the grid. The additional frequency support Grid #2 receives through the dc grid can be observed by comparing Figure 7-16(b) and Figure 7-18(b). Due to the power flow change at Terminal #1, the frequency in Grid #1 is disturbed. In Case 3, only the governors regulate the frequency in Grid #1. However, in Case 4, the offshore wind farm also tries to regulate Grid #1 frequency and undesired interactions between the converter controllers in Terminal #1 and #3 occurs. This can be seen from Figure 7-18(a), where the frequency disturbance in Grid #1 is higher in Case 4 than Case 3.

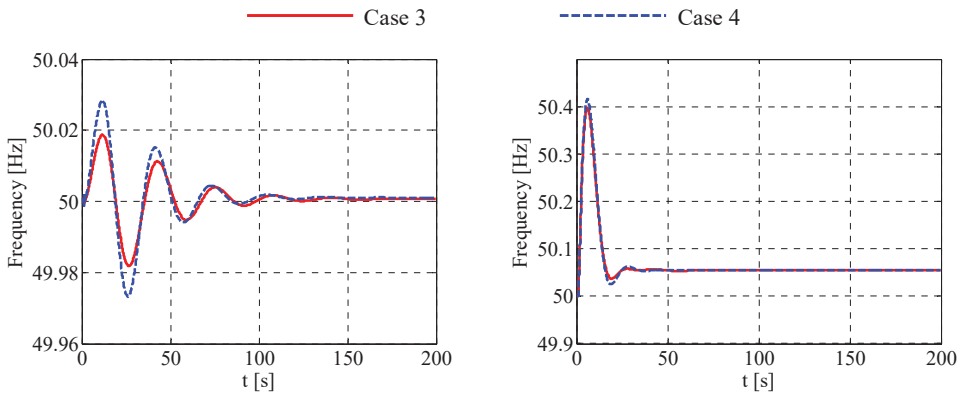

(a) Grid 1 Frequency (b) Grid 2 Frequency

Figure 7-18 : Frequency in Grid #1 and #2 for Case 3 and Case 4 for loss of load in Grid #2

Furthermore, the power production from the wind farm oscillates between increasing and decreasing its output. This is because the wind farm is trying to regulate Grid #1 frequency, while Terminal #1 is trying to contribute to the dc grid voltage regulation.

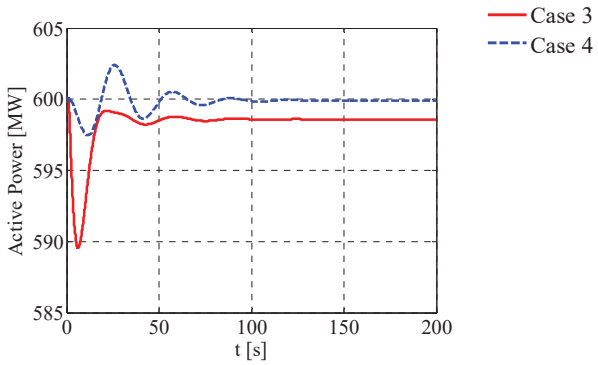

Figure 7-19 : Offshore Wind farm output for Case 3 and Case 4 for loss of load in Grid #2

The above results showed that when more than one ac grid receives frequency support from a dc grid, the proposed coordination between converter controllers leads to undesired interactions and causes more disturbance.

7.4. Chapter summary

This chapter showed the importance of global analysis in hybrid ac/dc power systems through two study cases. In the first case, global analysis of frequency stability and inertia

for two ac systems connected with an HVDC link was presented. Modal analysis and non-linear time domain analyses were used in the study. The analyses focused on the dynamic behavior of the ac grids for different types of frequency and inertia supports using HVDC converter controllers. It was shown that the frequency controllers perform as expected and improve the frequency stability of the grid receiving the support, and did not have any adverse effect on the grid providing the support. However, the electromechanical stability of the frequency support receiving grid was found to be reduced especially when frequency controller with inertia was used. In the second case study analysis, it was proposed that by coordinating converter controllers at an offshore wind farm and one ac grid, it is possible to maximize frequency support contribution of the offshore wind farm and avoid disturbance in other ac grids connected to the MTDC. However, the proposed method works when only one ac grid is getting frequency support and the remaining ac grid connected MTDC terminals are operating in dc droop or constant power control mode. If more than one ac grids are to receive frequency support through MTDC grid, then negative interactions occur when the proposed controller is used. Therefore, in such cases, distributed dc voltage and frequency droop control is the best control option. However, it should be noted that with distributed dc voltage and frequency droop control method, the frequency support comes not only from the wind farm but also from other ac grids behind an MTDC terminal operating in dc voltage droop control mode.

8. Conclusions and Future work

8.1. Conclusions

This thesis investigated stability and control of a hybrid ac/dc power system, where more than one asynchronous ac grids are connected to the same dc transmission system. The work used both small-signal and large signal analysis methods to study interactions between subsystems and/or controllers. In this thesis, the term interaction is used to refer to the existence of a dynamic coupling between subsystems. The interaction can be significant or insignificant, and may or may not affect the stability of the entire or part of the hybrid ac/dc power system. The main findings and conclusions are categorized into three main topics/areas as presented below.

i. Small-signal interaction between ac and dc grids

Modal analysis was used to study interaction between asynchronous ac grids interconnected through a dc grid. In addition, interactions between ac grids, converters and dc grid were studied.

To analyze the effect of the introduction of a dc grid on ac grid dynamics, a linear analysis was carried out for individual ac grids first, and then the results were compared with a linear analysis that was carried out for a hybrid system with the different ac grids interconnected through a dc grid. In general, the modes in the hybrid ac/dc system are a mere combination of the modes in the individual ac grids, and the additional modes that are related to the dc grid, converters and their controllers. For the study case considered, most of the ac grid modes of the hybrid ac/dc system stayed in the vicinity of the modes of the individual ac grids. The change in their positions was not significant enough to affect the stability of the overall system. However, it was shown in Chapter 7 that as a result of interaction between converter controllers and generator controllers, the electromechanical stability of an ac grid was found to be reduced. Therefore, depending upon controller settings and grid topology, undesired interactions, which may affect system stability, can occur between converter and generator the controllers in hybrid ac/dc power system.

Right eigenvectors or mode shapes of poorly damped modes were used to identify electro-mechanical interactions among generators located in synchronous areas in a hybrid ac/dc power system. In general, the magnitudes of the interactions are very low but are

influenced by dc grid control strategy and converter controller tuning. The observed interactions were between all ac grids if the dc grid is operated in dc voltage droop control mode. However, if the dc grid is operated in a master-slave type of control mode, then the interactions are observed only between ac grids behind constant power controlled terminal and an ac grid behind the master terminal that is controlling dc grid voltage. No interaction was observed between ac grids connected to a constant power controlling terminal. Furthermore, it was found that ac grid frequency reserve sharing through the dc grid and slower tuning of converter outer controllers results in higher dynamic coupling between ac grids. Contrarily, faster tuning of converter outer controllers results in lower interactions between asynchronous ac grids. In addition, the extent of the interactions increases when two poorly damped modes of different ac grids have a similar damped frequency. The source of the interactions is dynamic coupling between ac and dc grids. When several terminals share the duty of dc voltage regulation, as in the case of dc voltage droop control operation mode, the dynamics of the ac grids behind those terminals are coupled to a common dc grid (voltage) dynamics. This leads to an indirect coupling of dynamics of different ac grids through the dc grid dynamics.

A qualitative analysis of state matrix of a linearized representation of a simple system showed that the ac and dc dynamic coupling can be *one-way* or *two-way* depending up on the control mode of a converter. Figure 8-1 illustrates this phenomenon in the context of a hybrid ac/dc power system. The dc grid in Figure 8-1(a) is operating in dc voltage droop control mode, while the dc grid in Figure 8-1(b) is operating in master-slave control mode with the terminal connected to ac grid #2 operating as a slack bus. The solid lines indicate a dynamic coupling between ac and dc grids, while dashed lines indicate a coupling between asynchronous ac grids. The direction of the arrows indicates the direction of coupling. The two arrows between ac and dc grids pointing in opposite directions Figure 8-1(a) illustrate the *two-way* coupling between ac and dc grids when a converter is operating in dc voltage droop control mode. Similarly, the two arrows pointing in opposite directions in Figure 8-1(b) between ac grid #2 and the dc grid illustrate the *two-way* coupling between the grids under constant dc voltage control operation of the terminal converter. However, only a *one-way* coupling between an ac grid and a dc grid exists when the converter is operated in constant power control mode, as indicated by the single arrow between ac grid #1 and the dc grid in Figure 8-1(b). In such cases, the ac grid dynamics is coupled with the dc grid dynamics, but the dc grid dynamics is not coupled with the ac grid dynamics.

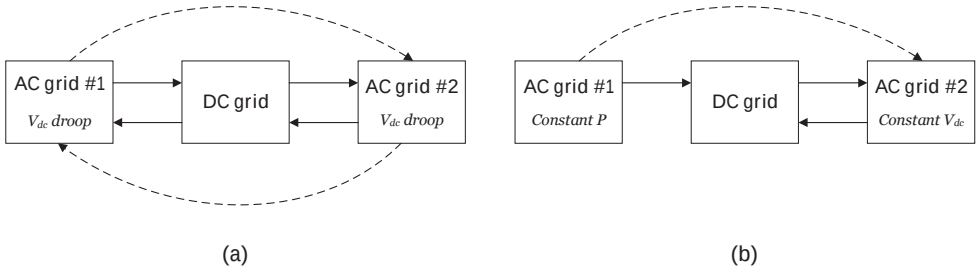

Figure 8-1 : ac/dc and ac/ac interaction for dc grid control mode (a) dc voltage droop and (b) master-slave

Therefore, the ac-to-ac interactions between all grids observed under dc voltage droop operation mode of the dc grid are due to ac grid dynamics is being coupled with dc grid dynamics, which in turn is coupled with other ac grid dynamics. This results in an indirect coupling of dynamics of two ac grids through the dynamics of the dc grid, as indicated by the two dashed-line arrows in Figure 8-1(a). On the other hand, when the dc grid is operated in master-slave control mode, only one terminal operates in dc voltage control mode while the other terminals operate in constant power control mode. Thus, even though there is a two-way coupling between ac and dc grid dynamics at the constant voltage controlling, the one-way coupling at the power controlling terminals prevents the dc grid dynamics from entering into the ac grids connected to them. Hence, the coupling is limited to ac grids behind constant power controlled terminal and an ac grid behind the master terminal that is controlling dc grid voltage, as shown by the single dashed-line arrow in Figure 8-1(b).

Cumulative participation factor of ac, converter and dc subsystems was used to identify interaction modes that have a certain degree of participation from two or more subsystems. It was found that in ac-to-converter interaction modes, generators and converter outer loop controllers participate most, while in converter-to-converter interaction modes, energy and circulating current controllers participate in most. In addition, generator speed and governor/turbine state variables participate most in interaction modes between asynchronous ac grids, which were are only found when frequency reserve sharing through the dc grid was activated. Most of the interaction modes identified were stable and well damped, while poorly damped interaction modes had strong participation from cable and dc-link capacitor state variables.

ii. Interaction between decentralized controllers

One of the ancillary services that can be provided by dc grids to connected ac grids is power oscillation damping (POD). Interaction between POD controllers on multiple terminals of an MTDC that interconnects several asynchronous ac grids was studied using decentralized control techniques. Methods for design of decentralized POD controllers and techniques for identification of interactions between POD control loops were presented. Geometric measures of controllability and observability were used to select the most effective input-output signal combinations for each POD controller and root locus method was used to tune the controllers. A case study was used to illustrate the interaction between PODs inserted at two terminals of an MTDC. Interaction between the selected control loops was assessed using dynamic relative gain array (DRGA) and performance relative gain array (PRGA) techniques in the frequency domain. In addition, modal and time domain analyses carried out for the study case supported the findings of the frequency domain analysis. For the analyzed study case, it was found that due to the interactions the performance of one of the controllers was augmented, while the performance of the other controller deteriorated. The analyses clearly showed that control loop interaction should be considered while tuning PODs on converters even if they are connected to different grids.

iii. Global frequency stability analysis

Frequency support can be provided to connected ac grids though HVDC systems. As the HVDC systems do not have their own active power source, the additional active power used in the frequency support service comes from wind farms and other ac grids connected to the HVDC systems. This affects the frequency of the other grids, which may or may not be experiencing a lack of frequency reserve and/or inertia. Therefore, it is important to carry out a global analysis that considers all connected ac grids, i.e. both frequency support receiving and providing ac grids. Through a case study of two ac grids connected with an HVDC link, it was shown that the frequency controllers perform as expected and improve the frequency stability of the grid receiving the support. No adverse effect on the stability of the grid that provided the frequency support was observed other than a frequency disturbance during the support period. However, the electromechanical stability of the frequency support-receiving grid was found to be reduced especially when frequency controller with inertia was used.

A coordinated control strategy for terminal converters of a dc grid was proposed to address the issue of frequency disturbance in other ac grids when one grid receives frequency support from an offshore wind farm. It was shown that by coordinating converter controllers at the offshore wind farm and the frequency support receiving ac grid, it is possible to maximize frequency support contribution of the offshore wind farm and avoid disturbance in other ac grids connected to the MTDC. However, the proposed method works when only one ac grid is getting frequency support and the remaining ac grid connected MTDC terminals are operating in dc droop or constant power control mode. If more than one ac grids are to receive frequency support through MTDC grid, then negative interactions occur when the proposed controller is used. Therefore, in such cases, distributed dc voltage and frequency droop control is the best control option. However, it should be noted that with distributed dc voltage and frequency droop control method, the frequency support comes not only from the wind farm but also from other ac grids behind an MTDC terminal operating in dc voltage droop control mode.

8.2. Future work

This thesis used modal analysis to identify interactions between ac and dc grids. Other methods can be used to analyze interactions and extend the results found in this work. The ac-to-ac interactions identified were low, but sensitive to converter controller mode and settings. More work can be done to determine scenarios where these interactions can be significant. In addition, research can be done on how to limit or even avoid the identified interactions.

Interaction between POD control loops was studied in this work. The findings can be extended by studying analytically how power flow, cable length, dc grid topology, etc influence the extent of control loop interactions. In addition, decentralized control techniques can be used to study interactions between dc grid converter controllers and controllers in the ac grid.

Ancillary services requiring active power, such as frequency/inertia and POD, cause an imbalance in the dc grid and lead to dc voltage disturbance. This disturbance is sensed by all terminal of a dc grid and is passed on to ac grids, which are connected to terminals participating in dc voltage regulation. Therefore, by limiting the dc grid voltage disturbance, it would be possible to prevent propagation of large signal disturbances in a hybrid ac/dc power system. An MMC converter has an extra degree of control freedom compared to two-level converters as both circulating and grid currents can be controlled

independently. Thus, studies can be carried out to investigate how MMC control can be used to decouple the ac and dc grid dynamics. In addition, it can be studied if the energy stored in the submodule capacitors can be used during the transient period so that dc grid voltage disturbance is reduced.

References

[1] (22.03.2017). *The 2020 Climate and Energy Package* European Union. Available: https://ec.europa.eu/clima/policies/strategies/2020_en

[2] (22.03.2017). *The 2030 Climate and Energy Framework* European Union. Available: https://ec.europa.eu/clima/policies/strategies/2030_en

[3] (2015, 22.03.2017). *The Paris Agreement* United Nations [Online]. Available: http://unfccc.int/paris_agreement/items/9485.php

[4] "The European Offshore Wind Industry - Key Trends and Statistics 2016," European Wind Energy Association (EWEA) Januray 2017.

[5] "Wind Energy Scenarios for 2020," European Wind Energy Association (EWEA) July 2014.

[6] (22.03.2017). *Borwin1* ABB [Online]. Available: http://new.abb.com/systems/hvdc/references/borwin1

[7] (22.03.2017). *Dolwin1* ABB. Available: http://new.abb.com/systems/hvdc/references/dolwin1

[8] (22.03.2017). *Dolwin2* ABB. Available: http://new.abb.com/systems/hvdc/references/dolwin1

[9] (22.03.2017). *Borwin2* Siemens [Online]. Available: http://www.energy.siemens.com/mx/en/power-transmission/grid-access-solutions/borwin-2.htm

[10] (22.03.2017). *Helwin1* Siemens [Online]. Available: http://www.energy.siemens.com/mx/en/power-transmission/grid-access-solutions/helwin-1.htm

[11] (22.03.2017). *Sylwin1* TenneT [Online]. Available: http://www.tennet.eu/our-grid/offshore-projects-germany/sylwin1/

[12] J. Beerten, S. Cole, and R. Belmans, "Modeling of Multi-Terminal VSC HVDC Systems with Distributed DC Voltage Control," *Power Systems, IEEE Transactions on,* vol. 29, pp. 34-42, 2014.

[13] N. R. Chaudhuri, B. Chaudhuri, R. Majumder, and A. Yazdani, *Multi-Terminal Direct-Current Grids: Modeling, Analysis, and Control*: Wiley, 2014.

[14] J. Freytes, L. Papangelis, H. Saad, P. Rault, T. V. Cutsem, and X. Guillaud, "On the Modeling of MMC for Use in Large Scale Dynamic Simulations," in *2016 Power Systems Computation Conference (PSCC)*, 2016, pp. 1-7.

[15] J. Beerten, S. Cole, and R. Belmans, "Generalized Steady-State VSC MTDC Model for Sequential AC/DC Power Flow Algorithms," *IEEE Transactions on Power Systems,* vol. 27, pp. 821-829, 2012.

[16] T. M. Haileselassie and K. Uhlen, "Precise Control of Power Flow in Multiterminal VSC-Hvdcs Using DC Voltage Droop Control," in *Power and Energy Society General Meeting, 2012 IEEE*, 2012, pp. 1-9.

[17] W. Wenyuan and M. Barnes, "Power Flow Algorithms for Multi-Terminal VSC-HVDC with Droop Control," *Power Systems, IEEE Transactions on,* vol. 29, pp. 1721-1730, 2014.

[18] T. K. Vrana, J. Beerten, R. Belmans, and O. B. Fosso, "A Classification of DC Node Voltage Control Methods for HVDC Grids," *Electric Power Systems Research,* vol. 103, pp. 137-144, 2013.

[19] Y. Phulpin and D. Ernst, "Ancillary Services and Operation of Multi-Terminal HVDC Grids," in *International Workshop on Transmission Networks for Offshore Wind Power Plants as well as on Transmission Networks for Offshore Wind Power Farms*, Aarhus, Denmark, 2011.

[20] M. Aragüés-Peñalba, A. Egea-Àlvarez, S. G. Arellano, and O. Gomis-Bellmunt, "Droop Control for Loss Minimization in HVDC Multi-Terminal Transmission Systems for Large Offshore Wind Farms," *Electric Power Systems Research,* vol. 112, pp. 48-55, 2014.

[21] M. A. Abdelwahed and E. F. El-Saadany, "Power Sharing Control Strategy of Multiterminal VSC-HVDC Transmission Systems Utilizing Adaptive Voltage Droop," *IEEE Transactions on Sustainable Energy,* vol. 8, pp. 605-615, 2017.

[22] P. Kundur, J. Paserba, V. Ajjarapu, G. Andersson, A. Bose, C. Canizares*, et al.*, "Definition and Classification of Power System Stability IEEE/CIGRE Joint Task Force on Stability Terms and Definitions," *IEEE Transactions on Power Systems,* vol. 19, pp. 1387-1401, 2004.

[23] G. Tang, "High Power Conversion Technology for High Voltage DC Transmission Application," in *ECCE*, Presentation, 2016.

[24] H. Rao, "Architecture of Nan'ao Multi-Terminal VSC-HVDC System and Its Multi-Functional Control," *CSEE Journal of Power and Energy Systems,* vol. 1, pp. 9-18, 2015.

[25] Z. Xu and C. Zhang, "Case Study: Dynamic Performance of a MTDC Network in Zhoushan City," *Energy Procedia,* vol. 88, pp. 341-348, 2016/06/01 2016.

[26] X. Lei. (2016, 21.03.2017). *21st Century Grids: Global Energy Interconnection* [Online]. Available: http://irena.org/innovationweek2016/outcomes/Planary4/IRENA%20Innovation%20Week%202016-Day%202_Technological%20Innovation%20Plenary_State%20Grid%20Corporation%20of%20China.pdf

[27] "SGRI Participates in Construction of Zhang-Bei DC Grid Pilot Project," ed: State Grid China, 2015.

[28] "Atlantic Wind Connection: Grid Resiliency, Its Economic and Security Impacts, and the Implications of AWC," T. C. Group, 2012.

[29] ABB. (2017, 21.03.2017). *North-East Agra*. Available: http://new.abb.com/systems/hvdc/references/north-east-agra

[30] R. Meere, J. Ruddy, P. McNamara, and T. O'Donnell, "Variable AC Transmission Frequencies for Offshore Wind Farm Interconnection," *Renewable Energy,* vol. 103, pp. 321-332, 2017.

[31] J. Ruddy, R. Meere, and T. O'Donnell, "Low Frequency AC Transmission for Offshore Wind Power: A Review," *Renewable and Sustainable Energy Reviews,* vol. 56, pp. 75-86, 2016.

[32] T. K. Vrana and O. Mo, "Optimal Operation Voltage for Maximal Power Transfer Capability on Very Long HVAC Cables," *Energy Procedia,* vol. 94, pp. 399-408, 2016.

[33] N. G. v. Luijk, "Delivering Energy through the World's Longest Submarine HV AC Cable," in *PES General Meeting, Presentation*, Denver, 2015.

[34] (03.03.2017). *Martin Linge: Innovating to Protect the Environment* [Online]. Available: http://www.total.no/en/powering-martin-linge-field-shore

[35] Yongtao Yang, M. Jafar, P. Vaessen, A. Yanushekvich, Y. Fu, R. Marshall, *et al.*, "Hybrid Grid: Towards a Hybrid AC/DC Transmission Grid," D. GL, 2015.

[36] "HVDC Grid Feasibility Study," C. W. G. B4.52, CIGRÈ April 2013.

[37] Magnus Callavik, Peter Lundberg, and O. Hansson, "Nordlink Pioneering VSC-HVDC Interconnector between Norway and Germany," in *White Paper*, 2015.

[38] "ABB Wins $900 Million Order to Connect Norwegian and German Power Grids," ed, 2015.

[39] D. Van Hertem and M. Ghandhari, "Multi-Terminal VSC HVDC for the European Supergrid: Obstacles," *Renewable and Sustainable Energy Reviews,* vol. 14, pp. 3156-3163, 2010.

[40] DESERTEC, "Clean Power from Deserts: The DESERTEC Concept for Energy, Water and Climate Security," 2009.

[41] S. Mano, B. Ovgor, Z. Samadov, M. Pudlik, V. Jülch, D. Sokolov, *et al.*, "Gobitec and Asian Super Grid for Renewable Energies in Northeast Asia," 2014.

[42] (14.03.2017). *Power from Shore* ABB [Online]. Available: http://new.abb.com/systems/hvdc/power-from-shore

[43] M. Barnes and A. Beddard, "Voltage Source Converter HVDC Links – the State of the Art and Issues Going Forward," *Energy Procedia,* vol. 24, pp. 108-122, 2012/01/01 2012.

[44] C. W. G. B4.56, "Guidelines for the Preparation of "Connection Agreements" or "Grid Codes" for Multi-Terminal DC Schemes and DC Grids," CIGRÈ 2016.

[45] R. E. Torres-Olguin, A. R. Årdal, H. Støylen, A. G. Endegnanew, K. Ljøkelsøy, and J. O. Tande, "Experimental Verification of a Voltage Droop Control for Grid Integration of Offshore Wind Farms Using Multi-Terminal HVDC," *Energy Procedia,* vol. 53, pp. 104-113, 2014.

[46] D. V. Hertem, O. Gomis-Bellmunt, and J. Liang, *HVDC Grids: For Offshore and Supergrid of the Future*: Wiley-IEEE Press 2016.

[47] N. R. Chaudhuri and B. Chaudhuri, "Adaptive Droop Control for Effective Power Sharing in Multi-Terminal DC (MTDC) Grids," *Power Systems, IEEE Transactions on,* vol. 28, pp. 21-29, 2013.

[48] A. Egea-Alvarez, J. Beerten, D. Van Hertem, and O. Gomis-Bellmunt, "Primary and Secondary Power Control of Multiterminal HVDC Grids," in *AC and DC Power Transmission (ACDC 2012), 10th IET International Conference on*, 2012, pp. 1-6.

[49] K. Rouzbehi, J. I. Candela, G. B. Gharehpetian, L. Harnefors, A. Luna, and P. Rodriguez, "Multiterminal DC Grids: Operating Analogies to AC Power Systems," *Renewable and Sustainable Energy Reviews,* vol. 70, pp. 886-895, 2017.

[50] T. M. Haileselassie, A. G. Endegnanew, and K. Uhlen, "Secondary Control in Multi-Terminal VSC-HVDC Transmission System," in *2015 IEEE Power & Energy Society General Meeting*, 2015, pp. 1-5.

[51] J. Beerten and D. V. Hertem, "Analysis of Power Redispatch Schemes for HVDC Grid Secondary Voltage Control," in *2015 IEEE Power & Energy Society General Meeting*, 2015, pp. 1-5.

[52] Y. Li, C. Rehtanz, S. Ruberg, L. Luo, and Y. Cao, "Assessment and Choice of Input Signals for Multiple HVDC and Facts Wide-Area Damping Controllers," *IEEE Transactions on Power Systems,* vol. 27, pp. 1969-1977, 2012.

[53] J. He, C. Lu, X. Wu, P. Li, and J. Wu, "Design and Experiment of Wide Area HVDC Supplementary Damping Controller Considering Time Delay in China Southern Power Grid," *IET Generation, Transmission & Distribution,* vol. 3, pp. 17-25, 2009.

[54] L. Harnefors, N. Johansson, L. Zhang, and B. Berggren, "Interarea Oscillation Damping Using Active-Power Modulation of Multiterminal HVDC Transmissions," *IEEE Transactions on Power Systems,* vol. 29, pp. 2529-2538, 2014.

[55] R. Eriksson, "A New Control Structure for Multiterminal DC Grids to Damp Interarea Oscillations," *IEEE Transactions on Power Delivery,* vol. 31, pp. 990-998, 2016.

[56] T. Smed and G. Andersson, "Utilizing HVDC to Damp Power Oscillations," *IEEE Transactions on Power Delivery,* vol. 8, pp. 620-627, 1993.

[57] Z. Jiebei, C. D. Booth, G. P. Adam, A. J. Roscoe, and C. G. Bright, "Inertia Emulation Control Strategy for VSC-HVDC Transmission Systems," *Power Systems, IEEE Transactions on,* vol. 28, pp. 1277-1287, 2013.

[58] T. Joseph, C. E. Ugalde-Loo, and J. Liang, "Subsynchronous Oscillatory Stability Analysis of an AC/DC Transmission System," in *2015 IEEE Eindhoven PowerTech*, 2015, pp. 1-6.

[59] T. M. Haileselassie and K. Uhlen, "Primary Frequency Control of Remote Grids Connected by Multi-Terminal HVDC," in *Power and Energy Society General Meeting, 2010 IEEE*, 2010, pp. 1-6.

[60] N. R. Chaudhuri, R. Majumder, and B. Chaudhuri, "System Frequency Support through Multi-Terminal DC (MTDC) Grids," *Power Systems, IEEE Transactions on,* vol. 28, pp. 347-356, 2013.

[61] D. Jing, Y. Phulpin, A. Sarlette, and D. Ernst, "Voltage Control in an HVDC System to Share Primary Frequency Reserves between Non-Synchronous Areas," presented at the 17th Power Systems Computation Conference (PSCC-11), Stockholm, 2011.

[62] Y. Pipelzadeh, N. R. Chaudhuri, B. Chaudhuri, and T. C. Green, "Coordinated Control of Offshore Wind Farm and Onshore HVDC Converter for Effective Power Oscillation Damping," *IEEE Transactions on Power Systems,* vol. PP, pp. 1-1, 2016.

[63] M. Ndreko, A. A. van der Meer, B. G. Rawn, M. Gibescu, and M. A. M. M. van der Meijden, "Damping Power System Oscilations by VSC-Based HVDC Networks: A North Sea Grid Case Study," in *12th Int. Workshop Large-Scale Integration of Wind Power Into Power Systems as Well as on Transmission Networks for Offshore Wind Power Plants*, 2013.

[64] L. Zeni, R. Eriksson, S. Goumalatsos, M. Altin, P. Sørensen, A. Hansen*, et al.*, "Power Oscillation Damping from VSC-HVDC Connected Offshore Wind Power Plants," *IEEE Transactions on Power Delivery,* vol. 31, pp. 829-838, 2016.

[65] l. y, Z. Xu, J. Ostergaard, and D. J. Hill, "Coordinated Control Strategies for Offshore Wind Farm Integration Via VSC-HVDC for System Frequency Support," *IEEE Transactions on Energy Conversion,* vol. PP, pp. 1-1, 2017.

[66] Y. Phulpin, "Communication-Free Inertia and Frequency Control for Wind Generators Connected by an HVDC-Link," *IEEE Transactions on Power Systems,* vol. 27, pp. 1136-1137, 2012.

[67] B. Silva, C. L. Moreira, L. Seca, Y. Phulpin, and J. A. P. Lopes, "Provision of Inertial and Primary Frequency Control Services Using Offshore Multiterminal HVDC Networks," *IEEE Transactions on Sustainable Energy,* vol. 3, pp. 800-808, 2012.

[68] Y. Pipelzadeh, B. Chaudhuri, and T. C. Green, "Inertial Response from Remote Offshore Wind Farms Connected through VSC-HVDC Links: A Communication-Less Scheme," in *2012 IEEE Power and Energy Society General Meeting*, 2012, pp. 1-6.

[69] ENTSO-E, "Network Code on High Voltage Direct Current Connections," ed: ENTSO-E, 2016.

[70] J. Machowski, J. Bialek, and J. Bumby, *Power System Dynamics: Stability and Control*: WILEY, 2008.

[71] P. M. Anderson and A. A. Fouad, *Power System Control and Stability*: IEEE Press, 1993.

[72] P. Kundur, *Power System Stability and Control*: McGraw-Hill Inc., 1994.

[73] P. W. Sauer and M. A. Pai, *Power System Dynamics and Stability*: Prentice-Hall, Inc., 1998.

[74] "Dynamic Models for Turbine-Governors in Power System Studies," IEEE 2013.

[75] NEPLAN, "Turbine-Governor Models: Standard Dynamic Turbine-Governor in Neplan Power System Analysis Tool," ed.

[76] C. W. G. B4.57, "Guide for the Development of Models for HVDC Converters in a HVDC Grid," CIGRÈ, 2014.

[77] A. Yazdani and R. Iravani, *Voltage-Sourced Converters in Power Systems : Modeling, Control, and Applications*: John Wiley & Sons, 2010.

[78] S. Cole, J. Beerten, and R. Belmans, "Generalized Dynamic VSC MTDC Model for Power System Stability Studies," *IEEE Transactions on Power Systems,* vol. 25, pp. 1655-1662, 2010.

[79] G. Bergna-Diaz, J. A. Suul, and S. D. Arco, "Small-Signal State-Space Modeling of Modular Multilevel Converters for System Stability Analysis," in *2015 IEEE Energy Conversion Congress and Exposition (ECCE)*, 2015, pp. 5822-5829.

[80] A. Jamshidifar and D. Jovcic, "Small-Signal Dynamic DQ Model of Modular Multilevel Converter for System Studies," *IEEE Transactions on Power Delivery,* vol. 31, pp. 191-199, 2016.

[81] A. Antonopoulos, L. Angquist, and H. P. Nee, "On Dynamics and Voltage Control of the Modular Multilevel Converter," in *Power Electronics and Applications, 2009. EPE '09. 13th European Conference on*, 2009, pp. 1-10.

[82] L. Harnefors, A. Antonopoulos, S. Norrga, L. Angquist, and H. P. Nee, "Dynamic Analysis of Modular Multilevel Converters," *IEEE Transactions on Industrial Electronics,* vol. 60, pp. 2526-2537, 2013.

[83] J. Beerten, S. D' Arco, and J. A. Suul, "Frequency-Dependent Cable Modelling for Small-Signal Stability Analysis of VSC-HVDC Systems," *IET Generation, Transmission & Distribution,* vol. 10, pp. 1370-1381, 2016.

[84] MATACDC. Available: https://www.esat.kuleuven.be/electa/teaching/matacdc

[85] J. Beerten and R. Belmans, "Matacdc - an Open Source Software Tool for Steady-State Analysis and Operation of HVDC Grids," in *11th IET International Conference on AC and DC Power Transmission*, 2015, pp. 1-9.

[86] J. Beerten and R. Belmans, "Development of an Open Source Power Flow Software for High Voltage Direct Current Grids and Hybrid AC/DC Systems: MATACDC," *IET Generation, Transmission & Distribution,* vol. 9, pp. 966-974, 2015.

[87] DIgSINTET. *Powerfactory*. Available: http://www.digsilent.de/index.php/products-powerfactory.html

[88] M. J. Gibbard, P. Pourveik, and D. J. Vowles, *Small-Signal Stability, Control and Dynamic Performance of Power Systems*. Adelaide: University of Adelaide Press, 2015.

[89] W. Birk and A. Medvedev, "A Note on Gramian-Based Interaction Measures," in *2003 European Control Conference (ECC)*, 2003, pp. 2625-2630.

[90] B. Wittenmark and M. E. Salgado, "Hankel-Norm Based Interaction Measure for Input-Output Pairing," *IFAC Proceedings Volumes,* vol. 35, pp. 429-434, 2002.

[91] A. Conley and M. E. Salgado, "Gramian Based Interaction Measure," in *Proceedings of the 39th IEEE Conference on Decision and Control (Cat. No.00CH37187)*, 2000, pp. 5020-5022 vol.5.

[92] E. Bristol, "On a New Measure of Interaction for Multivariable Process Control," *IEEE Transactions on Automatic Control,* vol. 11, pp. 133-134, 1966.

[93] S. Skogestad and I. Postlethwaite, *Multivariable Feedback Control*: John Wiley & Sons, Ltd, 2005.

[94] A. G. Endegnanew, J. Beerten, and K. Uhlen, "Dynamic Interactions between Asynchronous Grids Interconnected through an MTDC System," presented at the CIGRE Symposium, Lund, 2015.

[95] A. G. Endegnanew and K. Uhlen, "Investigation of Dynamic Behaviour of AC/DC Power Systems," in *14th Wind Integration Workshop 14th Workshop on Large-Scale Integration of Wind Power into Power Systems as well as on Transmission Networks for Offshore Wind Power Plants*, Brussels, 2015.

[96] J. Beerten, S. D. Arco, and J. A. Suul, "Identification and Small-Signal Analysis of Interaction Modes in VSC MTDC Systems," *IEEE Transactions on Power Delivery,* vol. 31, pp. 888-897, 2016.

[97] C. Canizares, T. Fernandes, E. G. Junior, G. L. Luc, M. Gibbard, I. Hiskens*, et al.*, "Benchmark Models for the Analysis and Control of Small-Signal Oscillatory Dynamics in Power Systems," *IEEE Transactions on Power Systems,* vol. PP, pp. 1-1, 2016.

[98] J. L. Domínguez-García, C. E. Ugalde-Loo, F. Bianchi, and O. Gomis-Bellmunt, "Input–Output Signal Selection for Damping of Power System Oscillations Using Wind Power Plants," *International Journal of Electrical Power & Energy Systems,* vol. 58, pp. 75-84, 6// 2014.

[99] M. Hovd and S. Skogestad, "Sequential Design of Decentralized Controllers," *Automatica,* vol. 30, pp. 1601-1607, 1994/10/01 1994.

[100] S. G. Johansson, G. Asplund, E. Jansson, and R. Rudervall, "Power System Stability Benefits with VSC DC-Transmission Systems," in *Cigre Session*, 2004, pp. B4-204.

[101] A. M. A. Hamdan and A. M. Elabdalla, "Geometric Measures of Modal Controllability and Observability of Power System Models," *Electric Power Systems Research,* vol. 15, pp. 147-155, 1988/10/01 1988.

[102] A. Heniche and I. Kamwa, "Control Loops Selection to Damp Inter-Area Oscillations of Electrical Networks," in *Power Engineering Society Summer Meeting, 2002 IEEE*, 2002, p. 240 vol.1.

[103] J. H. Chow, G. E. Boukarim, and A. Murdoch, "Power System Stabilizers as Undergraduate Control Design Projects," *IEEE Transactions on Power Systems,* vol. 19, pp. 144-151, 2004.

[104] P. S. D. P. Committee, "Benchmark Systems for Small-Signal Stability Analysis and Control," I. P. E. Society, Power System Dynamic Performace Committee, IEEE Power & Energy Society 2015.

[105] (24.01.2017). ENTSO-E [Online]. Available: https://emr.entsoe.eu/glossary/bin/view/ENTSO-E+Common+Glossary/

[106] C. W. G. C4.601, "Review of on-Line Dynamic Security Assessment Tools and Techniques," CIGRE Technical Brochure No. 325 2007.

[107] T. M. Haileselassie, R. E. Torres-Olguin, T. K. Vrana, K. Uhlen, and T. Undeland, "Main Grid Frequency Support Strategy for VSC-HVDC Connected Wind Farms with Variable Speed Wind Turbines," in *PowerTech, 2011 IEEE Trondheim*, 2011, pp. 1-6.

[108] C. L. Moreira, J. R. Gouveia, and B. Silva, "Participation of Multi-Terminal HVDC Grids in Frequency Regulation Services," in *Compatibility and Power Electronics (CPE), 2015 9th International Conference on*, 2015, pp. 202-209.

[109] L. Hongzhi and C. Zhe, "Contribution of VSC-HVDC to Frequency Regulation of Power Systems with Offshore Wind Generation," *Energy Conversion, IEEE Transactions on,* vol. 30, pp. 918-926, 2015.

[110] S. P. Teeuwsen and R. Rossel, "Dynamic Performance of the 1000 MW BritNed HVDC Interconnector Project," in *Power and Energy Society General Meeting, 2010 IEEE*, 2010, pp. 1-8.

[111] (17.03.2017). *BritNed* [Online]. Available: http://www.britned.com/

[112] J. E. S. de Haan, C. Escudero Concha, M. Gibescu, J. van Putten, G. L. Doorman, and W. L. Kling, "Stabilising System Frequency Using HVDC between the Continental European, Nordic, and Great Britain Systems," *Sustainable Energy, Grids and Networks,* vol. 5, pp. 125-134, 2016.

[113] Energynet.dk, "Energinet.Dk's Ancillary Services Strategy 2015-2017," 2015.

[114] Energynet.dk, "Energinet.Dk's Ancillary Services Strategy," 2011.

[115] A. G. Endegnanew and K. Uhlen, "Coordinated Converter Control Strategy in Hybrid AC/DC Power Systems for System Frequency Support," *Energy Procedia,* vol. 94, pp. 173-181, 2016.

[116] A. G. Endegnanew and K. Uhlen, "Global Analysis of Frequency Stability and Inertia in AC Systems Interconnected through an HVDC," in *2016 IEEE International Energy Conference (ENERGYCON)*, 2016, pp. 1-6.

[117] F. Golnaraghi and B. C. Kuo, *Automatic Control Systems*, 9th ed.: Wiley, 2009.

[118] L. Zeni, "Power System Integration of VSC-HVDC Connected Wind Power Plants," PhD, Technical University of Denmark, 2015.

[119] A. Korompili, Q. Wu, and H. Zhao, "Review of VSC HVDC Connection for Offshore Wind Power Integration," *Renewable and Sustainable Energy Reviews,* vol. 59, pp. 1405-1414, 2016.

Appendix

A1. State space matrix

The symbolic state and input matrix for a single converter connected with a stiff bus and an ideal dc voltage source is presented for three control modes of the converter.

A1.1 Constant dc voltage control

$$\mathbf{A}=\begin{bmatrix}
-\frac{r_f\omega_0}{l_f} & \omega_g\omega_0 & 0 & 0 & 0 & 0 & \frac{\omega_0}{l_f} & 0 & 0 \\
-\omega_g\omega_0 & -\frac{r_f\omega_o}{l_f} & 0 & 0 & 0 & 0 & 0 & \frac{\omega_0}{l_f} & 0 \\
-k_{Pi}V_{gd0} & 0 & 0 & 0 & 0 & 0 & 0 & 0 & 0 \\
0 & -k_{Pi}v_{gd} & 0 & 0 & 0 & 0 & 0 & 0 & 0 \\
k_{ii}(-k_{Pp})v_{gd}-k_{ii} & 0 & k_{ii} & 0 & 0 & 0 & 0 & 0 & 0 \\
0 & k_{ii}(-k_{Pp})v_{gd}-k_{ii} & 0 & k_{ii} & 0 & 0 & 0 & 0 & 0 \\
-\frac{k_{ip}k_{Pp}v_{gd}+k_{ip}}{T_{rconv}} & -\frac{l_f\omega_o}{T_{rconv}} & \frac{k_{ip}}{T_{rconv}} & 0 & \frac{1}{T_{rconv}} & 0 & -\frac{1}{T_{rconv}} & 0 & 0 \\
\frac{l_f\omega_g}{T_{rconv}} & -\frac{k_{ip}k_{Pp}v_{gd}+k_{ip}}{T_{rconv}} & 0 & \frac{k_{ip}}{T_{rconv}} & 0 & \frac{1}{T_{rconv}} & 0 & -\frac{1}{T_{rconv}} & 0 \\
-\frac{v_{sd}}{c_{dc}v_{dc}} & -\frac{v_{sq}}{c_{dc}v_{dc}} & 0 & 0 & 0 & 0 & -\frac{i_{gd}}{c_{dc}v_{dc}} & -\frac{i_{gq}}{c_{dc}v_{dc}} & -\frac{-i_{gd}r_{dc}v_{sd}-i_{gq}r_{dc}v_{sq}+v_{dc}^2}{c_{dc}r_{dc}v_{dc}^2}
\end{bmatrix}$$

$$\mathbf{B}=\begin{bmatrix} 0 & 0 & -\frac{\omega_0}{l_f} & 0 & 0 & i_{gq}\omega_0 \\ 0 & 0 & 0 & -\frac{\omega_0}{l_f} & 0 & -i_{gd}\omega_0 \\ k_{Pi} & 0 & -i_{gd}k_{Pi} & 0 & 0 & 0 \\ 0 & -k_{Pi} & -i_{gq}k_{Pi} & 0 & 0 & 0 \\ k_{ii}k_{Pp} & 0 & -i_{gd}k_{ii}k_{Pp} & 0 & 0 & 0 \\ 0 & -k_{ii}k_{Pp} & -i_{gq}k_{ii}k_{Pp} & 0 & 0 & 0 \\ \frac{k_{ip}k_{Pp}}{T_{rconv}} & 0 & -\frac{i_{gd}k_{ip}k_{Pp}-1}{T_{rconv}} & 0 & 0 & -\frac{i_{gq}l_f}{T_{rconv}} \\ 0 & -\frac{k_{ip}k_{Pp}}{T_{rconv}} & -\frac{i_{gq}k_{ip}k_{Pp}}{T_{rconv}} & \frac{1}{T_{rconv}} & 0 & \frac{i_{gd}l_f}{T_{rconv}} \\ 0 & 0 & 0 & 0 & \frac{1}{c_{dc}r_{dc}} & 0 \end{bmatrix}$$

$$\mathbf{x}=\begin{bmatrix} i_{gd} \\ i_{gq} \\ N_d \\ N_q \\ M_d \\ M_q \\ v_{sd} \\ v_{sq} \\ v_{dc} \end{bmatrix} \qquad \mathbf{u}=\begin{bmatrix} P_{ref} \\ Q_{ref} \\ v_{gd} \\ v_{gq} \\ v_{dcideal} \\ \omega_{PLL} \end{bmatrix}$$

A1.2 Constant active power control

$$\mathbf{A}=\begin{bmatrix}
-\frac{r_f\omega_0}{l_f} & \omega_{pll}\omega_0 & 0 & 0 & 0 & 0 & \frac{\omega_0}{l_f} & 0 & 0\\
-\omega_{pll}\omega_0 & -\frac{r_f\omega_0}{l_f} & 0 & 0 & 0 & 0 & 0 & \frac{\omega_0}{l_f} & 0\\
0 & 0 & 0 & 0 & 0 & 0 & 0 & 0 & -k_{pi}\\
0 & -k_{pi}v_{gd} & 0 & 0 & 0 & 0 & 0 & 0 & 0\\
-k_{ii} & 0 & k_{ii} & 0 & 0 & 0 & 0 & 0 & -k_{ii}k_{pp}\\
0 & -k_{pp}v_{gd}k_{ii}-k_{ii} & 0 & k_{ii} & 0 & 0 & 0 & 0 & 0\\
-\frac{k_{ip}}{T_{rconv}} & -\frac{l_f\omega_{pll}}{T_{rconv}} & \frac{k_{ip}}{T_{rconv}} & 0 & \frac{1}{T_{rconv}} & 0 & -\frac{1}{T_{rconv}} & 0 & -\frac{k_{ip}k_{pp}}{T_{rconv}}\\
\frac{l_f\omega_{pll}}{T_{rconv}} & -\frac{k_{pp}v_{gd}k_{ip}+k_{ip}}{T_{rconv}} & 0 & \frac{k_{ip}}{T_{rconv}} & 0 & \frac{1}{T_{rconv}} & 0 & -\frac{1}{T_{rconv}} & 0\\
-\frac{v_{sd}}{c_{dc}v_{dc}} & -\frac{v_{sq}}{c_{dc}v_{dc}} & 0 & 0 & 0 & 0 & -\frac{i_{gd}}{c_{dc}v_{dc}} & -\frac{i_{gq}}{c_{dc}v_{dc}} & -\frac{v_{dc}^2-i_{gd}r_{dc}v_{sd}-i_{gq}r_{dc}v_{sq}}{c_{dc}r_{dc}v_{dc0}^2}
\end{bmatrix}$$

$$\mathbf{B}=\begin{bmatrix}
0 & 0 & -\frac{\omega_0}{l_f} & 0 & 0 & i_{gq}\omega_0\\
0 & 0 & 0 & -\frac{\omega_0}{l_f} & 0 & -i_{gd}\omega_0\\
k_{pi} & 0 & 0 & 0 & 0 & 0\\
0 & -k_{pi} & -i_{gq}k_{pi} & 0 & 0 & 0\\
k_{ii}k_{pp} & 0 & 0 & 0 & 0 & 0\\
0 & -k_{ii}k_{pp} & -i_{gq}k_{ii}k_{pp} & 0 & 0 & 0\\
\frac{k_{ip}k_{pp}}{T_{rconv}} & 0 & \frac{1}{T_{rconv}} & 0 & 0 & -\frac{i_{gq}l_f}{T_{rconv}}\\
0 & -\frac{k_{ip}k_{pp}}{T_{rconv}} & -\frac{i_{gq}k_{ip}k_{pp}}{T_{rconv}} & \frac{1}{T_{rconv}} & 0 & \frac{i_{gd}l_f}{T_{rconv}}\\
0 & 0 & 0 & 0 & \frac{1}{c_{dc}r_{dc}} & 0
\end{bmatrix}$$

$$\mathbf{u} = \begin{bmatrix} v_{dcref} \\ Q_{ref} \\ v_{gd} \\ v_{gq} \\ v_{dcideal} \\ \omega_{pll} \end{bmatrix} \quad \mathbf{x} = \begin{bmatrix} i_{gd} \\ i_{gq} \\ N_d \\ N_q \\ M_d \\ M_q \\ v_{sd} \\ v_{sq} \\ v_{dc} \end{bmatrix}$$

A1.3 DC voltage droop control

$$\mathbf{A}=\begin{pmatrix}
-\frac{r_f\omega_o}{l_f} & \omega_{pll}\omega_o & 0 & 0 & 0 & 0 & \frac{\omega_o}{l_f} & 0 & 0\\
-\omega_{pll}\omega_o & -\frac{r_f\omega_o}{l_f} & 0 & 0 & 0 & 0 & 0 & \frac{\omega_o}{l_f} & 0\\
-k_{pi}v_{gd} & 0 & 0 & 0 & 0 & 0 & 0 & 0 & -\frac{k_{pi}}{\rho_{dc}}\\
0 & -k_{pi}v_{gd} & 0 & 0 & 0 & 0 & 0 & 0 & 0\\
-k_{pp}v_{gd}k_{ii}-k_{ii} & 0 & k_{ii} & 0 & 0 & 0 & 0 & 0 & -\frac{k_{ii}k_{pp}}{\rho_{dc}}\\
0 & -k_{pp}v_{gd}k_{ii}-k_{ii} & 0 & k_{ii} & 0 & 0 & 0 & 0 & 0\\
-\frac{\rho_{dc}k_{ip}+\rho_{dc}k_{pp}v_{gd}k_{ip}}{\rho_{dc}T_{rconv}} & -\frac{l_f\omega_{pll}}{T_{rconv}} & \frac{k_{ip}}{T_{rconv}} & 0 & \frac{1}{T_{rconv}} & 0 & -\frac{1}{T_{rconv}} & 0 & -\frac{k_{ip}k_{pp}}{\rho_{dc}T_{rconv}}\\
\frac{l_f\omega_{pll}}{T_{rconv}} & -\frac{k_{pp}v_{gd}k_{ip}+k_{ip}}{T_{rconv}} & 0 & \frac{k_{ip}}{T_{rconv}} & 0 & \frac{1}{T_{rconv}} & 0 & -\frac{1}{T_{rconv}} & 0\\
-\frac{v_{sd}}{c_{dc}v_{dc}} & -\frac{v_{sq}}{c_{dc}v_{dc}} & 0 & 0 & 0 & 0 & -\frac{i_{gd}}{c_{dc}v_{dc}} & -\frac{i_{gq}}{c_{dc}v_{dc}} & -\frac{v_{dc}^2-i_{gd}r_{dc}v_{sd}-i_{gq}r_{dc}v_{sq}}{c_{dc}r_{dc}v_{dc}^2}
\end{pmatrix}$$

$$\mathbf{B}=\begin{pmatrix} 0 & 0 & 0 & -\frac{\omega_o}{l_f} & 0 & 0 & i_{gq}\omega_o \\ 0 & 0 & 0 & 0 & -\frac{\omega_o}{l_f} & 0 & -i_{gd}\omega_o \\ k_{pi} & \frac{k_{pi}}{\rho_{dc}} & 0 & -i_{gd}k_{pi} & 0 & 0 & 0 \\ 0 & 0 & -k_{pi} & -i_{gq}k_{pi} & 0 & 0 & 0 \\ k_{ii}k_{pp} & \frac{k_{ii}k_{pp}}{\rho_{dc}} & 0 & -i_{gd}k_{ii}k_{pp} & 0 & 0 & 0 \\ 0 & 0 & -k_{ii}k_{pp} & -i_{gq}k_{ii}k_{pp} & 0 & 0 & 0 \\ \frac{k_{ip}k_{pp}}{T_{rconv}} & \frac{k_{ip}k_{pp}}{\rho_{dc}T_{rconv}} & 0 & -\frac{\rho_{dc}i_{gd}k_{ip}k_{pp}-\rho_{dc}}{\rho_{dc}T_{rconv}} & 0 & 0 & -\frac{i_{gq}l_f}{T_{rconv}} \\ 0 & 0 & -\frac{k_{ip}k_{pp}}{T_{rconv}} & -\frac{i_{gq}k_{ip}k_{pp}}{T_{rconv}} & \frac{1}{T_{rconv}} & 0 & \frac{i_{gd}l_f}{T_{rconv}} \\ 0 & 0 & 0 & 0 & 0 & \frac{1}{c_{dc}r_{dc}} & 0 \end{pmatrix}$$

$$\mathbf{x}=\begin{bmatrix} i_{gd} \\ i_{gq} \\ N_d \\ N_q \\ M_d \\ M_q \\ v_{sd} \\ v_{sq} \\ v_{dc} \end{bmatrix} \quad \mathbf{u}=\begin{bmatrix} P_{ref} \\ v_{dcref} \\ Q_{ref} \\ v_{gd} \\ v_{gq} \\ v_{dcideal} \\ \omega_{Pll} \end{bmatrix}$$